POLITECNICO DI TORINO

Master's Degree in Aerospace Engineering

Politecnico di Torino

Master's Thesis

Development of Biodegradable Helium Balloons for Atmospheric Mini Radio-Probes and Measurement of Physical Fluctuations within the Atmospheric Boundary Layer

Supervisor: Prof. Daniela Tordella (DISAT)

Co-supervisor: Ing. Pasquale Russo Spena (DIGEP)

Candidate: Riccardo Villa

Academic Year 2024/2025

Abstract

Understanding turbulent processes in clouds is one of the most important challenges in atmospheric physics and one of the main sources of uncertainty in climate models. Clouds regulate the hydrological cycle and the Earth's energy balance, but the mechanisms that control their dynamics are still only partly understood. The classical turbulence theory by Kolmogorov (K41), while fundamental, is based on three assumptions — stationarity, homogeneity, and isotropy — which are rarely satisfied in real atmospheric flows. Numerical simulations try to address these limits, but at the current state of the art they can only cover small portions of reality: DNS are restricted to domains of a few meters, while global models work with grids of several kilometers, which cannot describe local microphysical processes.

Besides numerical models, experimental observations are also limited. Radars, aircraft, and large balloons provide useful data, but they cannot follow the evolution of flows at small scales. To really understand the dynamics of the Atmospheric Boundary Layer (ABL) and of clouds, a different approach is needed: one that looks at the atmosphere from the point of view of the air particles, in a Lagrangian way, able to capture the evolution and fluctuations of physical quantities down to the smallest scales.

This is the challenge of the European COMPLETE project (Horizon 2020), which introduces ultralight and environmentally sustainable radiosondes, designed to follow the atmospheric flow like tracked particles. These sondes collect thermodynamic and kinematic data *in situ* and send them in real time to ground receiving stations, and when launched in clusters they make it possible to build multipoint Lagrangian datasets.

This thesis first describes the radiosondes developed in the COMPLETE project and the environment where they operate, with focus on atmospheric turbulence and cloud processes. Then, it presents two main personal contributions. The first is the design, construction, and testing of a double-wheel thermal sealer, developed to improve the reliability and efficiency of the production of aerostatic balloons, essential for the flotation of the sondes on isopycnic surfaces. The second is the analysis of data from two experimental launches, with a single sonde and with a cluster respectively, used to test a new communication system based on a public network of ground stations worldwide, opening new perspectives for the future of the project.

Acknowledgements

Desidero innanzitutto ringraziare la Prof.ssa Daniela Tordella per avermi dato l'opportunità di far parte di questo gruppo di ricerca, coinvolgendomi con costanza e dimostrandosi sempre disponibile. Ringrazio inoltre il dott. Shahbozbek Abdunabiev e la dott.ssa Mina Golshan per la gentilezza e i preziosi consigli che mi hanno aiutato notevolmente in questo percorso. Un ringraziamento al Prof. Pasquale Russo Spena per la disponibilità e per l'accesso al centro J-Tech, dove ho sviluppato parte della tesi.

Grazie alle colleghe tesiste Eleonora e Maria, con cui ho condiviso, seppur in poco tempo, numerose esperienze dentro e fuori da questa tesi.

Ringrazio la mia famiglia per il supporto costante in questi anni universitari: mi sono sentito davvero fortunato e credo siano stati loro, più dell'università, la mia rampa di lancio verso il futuro. Un pensiero va a mamma e papà, a Lara, a tutti i nonni, a Edo e a chi, pur non menzionato, è per me altrettanto importante.

C'è poi una seconda famiglia, formata dagli amici più cari, che sono stati pilastri fondamentali nel diventare la persona che sono: Stefano, Noemi, i miei colleghi Gaia, Gio, Vitto, Luca, Etta e Laura, tutti gli amici della Grigliata dei Nonni e quelli di Pievetta (il cui nome del gruppo è forse meglio non riportare in una tesi universitaria).

In chiusura, ma non per importanza, desidero ringraziare Ino*. Mi ha sempre sostenuto, amato e spronato; con lei ho capito cosa davvero significhi trovare la felicità in un'altra persona, e senza il suo appoggio questo traguardo non avrebbe avuto lo stesso valore.

*All'anagrafe, Federica.

Contents

List of Figures

List of Tables

Introduction

Atmospheric turbulence remains one of the most complex phenomena to describe in fluid dynamics. Within the layer closest to the Earth's surface, the so-called atmospheric boundary layer (ABL), and the warm clouds that develop within it, matter and energy are transported by an extremely complex system of turbulent motions distributed over a wide range of spatial and temporal scales. This multiscale nature makes it difficult to fully represent the behavior of the atmosphere using numerical models alone.

Direct numerical simulations (DNS) would allow for the detailed resolution of the entire turbulent cascade, but are limited to domains on the order of a few meters due to their high computational cost. At the other extreme, global and mesoscale climate models can describe dynamics over expanses of hundreds or thousands of kilometers, but with a typical spatial resolution of a few kilometers, insufficient to represent the more local processes occurring within clouds or in the boundary layer. For this reason, *in situ* experimental observations using radar, lidar, radiosondes, atmospheric profiling systems, and airborne platforms, still play an essential role in overcoming the limitations of numerical models.

It is within this context that the European H2020–COMPLETE project fits in, proposing a new experimental approach based on the development of ultralight and biodegradable radiosondes, designed to follow atmospheric motions in a Lagrangian manner, that is, behaving like fluid particles which, while being passively transported by the flow, record in real time the physical quantities encountered along their trajectory.

The core of the project consists of coupling a miniaturized sensor system, integrated on a printed circuit board (PCB), with a balloon that allows its passive transport. The design of the balloon, although it might appear as a secondary aspect, represents one of the main challenges of the project: it is necessary to combine lightness, mechanical strength, and gas retention with the use of an environmentally sustainable material such as Mater-Bi, capable of guaranteeing adequate performance and, at the same time, a reduced environmental impact.

Part of this work focuses precisely on this aspect, describing the design and construction of a double-wheel thermal welder developed to improve both efficiency and reliability in balloon production, particularly in the welding of its component parts. The system was designed, built, and tested in the laboratory, identifying the optimal parameters of pressure, temperature, and speed, and leading to the production of full-scale balloons subsequently subjected to helium leak tests and a tethered launch of two radiosondes.

In parallel, the thesis addresses a second fundamental aspect for the development of the project, presenting a series of experiments aimed at validating a new LoRaWAN communication system for transmitting the data collected by the sondes. Until now, the project's radiosondes have communicated in peer-to-peer mode via private single-channel receivers, a solution that limited launches both in terms of the number of probes that could be managed simultaneously and in the duration of data reception, as the probes

stopped transmitting once they left the receiver's coverage range. The introduction of a standardized communication protocol on a public network, based on The Things Network (TTN) receiving stations, made it possible to overcome these limitations, enabling cluster launches composed of numerous sondes that can potentially be tracked for the entire battery life (up to about 16 hours) and from any location within network coverage.

After an initial test involving a single sonde launched from the Politecnico di Torino in June 2025, this work presents the cluster launch carried out in Carmagnola (Italy) a month later, which saw the simultaneous flight of twenty probes, the highest number ever achieved in the project's experimental campaigns. This larger number of sondes, together with the extended transmission duration, allowed for a more detailed and robust analysis of numerous environmental parameters and the turbulent characteristics of the atmosphere, including energy spectra, energy dissipation rates, and turbulent dispersion.

The thesis is organized as follows. Chapter 1 introduces the theoretical foundations of turbulence; Chapter 2 applies these principles to the atmospheric boundary layer and clouds, focusing particularly on the microphysical processes governing the formation and development of *warm clouds*. Chapter 3 presents the H2020–COMPLETE project (now evolved into HOUSEFLIES) and the main components of the radiosonde, followed by an overview of the most relevant experiments conducted for the validation of the first prototype. Chapter 4 focuses on the choice of balloon material and its sizing.

The last two chapters concern most of my contribution to the project, developed along two parallel lines. Chapter 5 describes the development of the double-wheel thermal sealer prototype, from the motivations behind its conceptual design to the CAD modeling, the design of the pressure system, and the realization. The results of a helium leak test and a tethered launch with two probes, which were used to validate the welds, are also presented. Finally, Chapter 6 describes the two experimental campaigns previously introduced, analyzing the data and estimating quantitative parameters of atmospheric turbulence, and concludes with a discussion of the future prospects for the project.

Chapter 1

Turbulent flows

In physics, the term turbulence refers to the chaotic behavior of a fluid in space and time, characterized by continuous variations in velocity and pressure that make it intrinsically non-stationary. Unlike laminar flow, where the fluid moves in ordered and parallel layers, turbulent flow generates vortices that enhance mixing and energy transport.

This mechanism of vortical motion was already observed by Leonardo da Vinci in the sixteenth century who, with his remarkable observational skills, recognized a fundamental property of turbulence: its multiscale nature.

Figure 1.1: Turbulent structures at different scales, drawn by Leonardo da Vinci.

Vortical structures are distributed over a wide range of spatial scales, including several orders of magnitude, which coexist and interact inertially with one another, making turbulence a strongly nonlinear phenomenon. Its complexity is emphasized even more when we consider its intrinsic randomness.

Although turbulent flows are governed by the Navier–Stokes equations, which are deterministic and (in principle) capable of describing the velocity field exactly, the resulting solutions still appear random. This apparent paradox exists because turbulent motion is extremely sensitive to small perturbations in the initial and boundary conditions, as well as in the intrinsic properties of the fluid. As a result, turbulence is unpredictable in

detail: it is not possible to define a unique velocity field in space and time, and statistical tools must be employed instead.

A fundamental parameter in the study of turbulence is the Reynolds number, which expresses the ratio between inertial forces and diffusive effects within the fluid. It is defined as:

$$Re = \frac{U\,L}{\nu} \tag{1.1}$$

where U is a characteristic velocity of the flow at the characteristic length scale of the phenomenon, L, and ν is the kinematic viscosity of the fluid.

In general, the larger the Reynolds number, the more unstable the flow becomes and the more it tends to develop turbulence, eventually reaching what is known as fully developed turbulence at high Re. However,it should be remembered that the exact threshold for this transition depends on the specific type of flow considered.

In the following sections, some of the main characteristics of turbulent motion will be analyzed, with particular emphasis on the domain of interest for this work: the atmospheric boundary layer.

1.1 Energy Cascade

As mentioned earlier, a turbulent flow consists of a large number of vortical structures at different spatial scales. To understand the origins of this concept, we must go back to 1922, when Lewis Fry Richardson first introduced the concept of the energy cascade [1]. His well-known poem expressed it as:

> "Big whorls have little whorls, which feed on their velocity,
> And little whorls have lesser whorls, and so on to viscosity."

Richardson intuited that turbulence was not a purely chaotic phenomenon but followed an inertial process according to an organized "cascade" structure.

Richardson's idea was later formalized in 1941 by Andrey Kolmogorov with his K41 theory, where he described the energy cascade in more quantitative terms [2].

It must be clarified from the beginning that Kolmogorov's results, although strongly supported by experiments, relied on two fundamental but somewhat restrictive assumptions. First, the flow must have a very high Reynolds number, corresponding to the so-called fully developed turbulence. Second, the small scales ($\ell \ll L_0$) are assumed to be statistically isotropic (local isotropy) and homogeneous.

Under these assumptions, Kolmogorov demonstrated that energy is

1. introduced into the system through the largest scales (the energy-containing range). Among these, the macroscale is the largest scale of the system, dependent on the outer scale, and is denoted as L_0;

2. transferred, without significant dissipation, to progressively smaller scales through the inertial cascade (the inertial range);

3. dissipated at the smallest scales, when lengths become small enough that diffusive processes act at the same order of magnitude as inertial ones. At this point, viscosity interrupts the cascade and dissipates kinetic energy into heat. The smallest scale of the system is called the Kolmogorov scale (η) [3].

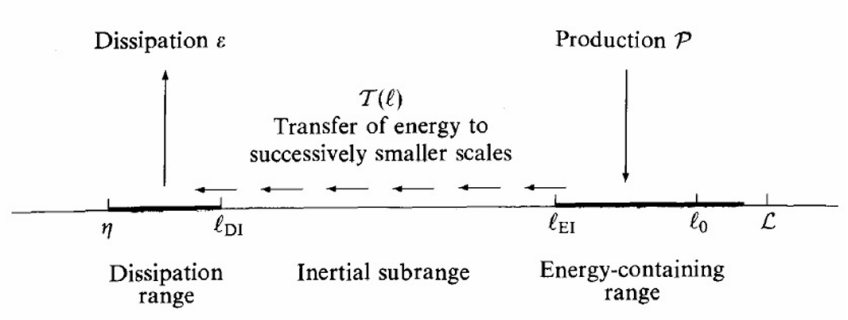

Figure 1.2: Energy cascade process: energy transfer from large scales to smaller scales. Image taken from: Pope, S. B. *Turbulent Flows.* Cambridge University Press, 2000.

The mechanism that enables the continuous transfer of energy from larger to smaller vortices is known as vortex stretching. Velocity gradients within the flow cause the stretching (or compression) of vortices, and when the cross-section of a vortical structure decreases due to stretching, its intensity, or vorticity, increases. This leads to the formation of new, smaller, and more intense vortices, to which turbulent kinetic energy is transferred [4].

Finally, considering how energy is dissipated at the end of this cascade, it can be quantified (as a first approximation) through a simple dimensional analysis. Since the rate of energy input per unit mass at the larger scales is the same as the rate dissipated at the smallest scales, the energy dissipation rate can be expressed as:

$$\varepsilon \sim \frac{U^3}{L} \tag{1.2}$$

where U and L are the characteristic velocity and length of the largest eddies.

1.2 Energy Spectrum and Universal Equilibrium

One of the key results of Kolmogorov's K41 theory is that, in a turbulent flow with a sufficiently high Reynolds number and under conditions of local isotropy, the statistics of small-scale turbulent motion are subject to a law of universal equilibrium. This means that, at these scales, the properties depend solely on the kinematic viscosity ν of the fluid and on the energy dissipation rate ε.

A direct consequence of this is the possibility of defining, through dimensional arguments, the Kolmogorov scales:

$$\eta = \left(\frac{\nu^3}{\varepsilon}\right)^{1/4}, \qquad u_\eta = (\nu\varepsilon)^{1/4}, \qquad \tau_\eta = \left(\frac{\nu}{\varepsilon}\right)^{1/2} \tag{1.3}$$

where:

- η is the Kolmogorov length, the smallest scale of the system,
- u_η is the characteristic velocity relative to the scale η,
- τ_η is the characteristic time of the smallest scale.

The dependence on these parameters implies that the mechanism of energy input at the macroscale and the boundary conditions are no longer relevant in the universal equilibrium range, where instead the turbulent behavior is characterized by similarity.

This peculiar property is also reflected in the distribution of turbulent kinetic energy across different scales, namely in the energy spectrum $E(k)$, which describes how energy is distributed with respect to the wavenumber k (or, equivalently, the frequency f) of a given scale.

Since $E(k)$ has the dimensions of energy per unit wavenumber, that is

$$E(k) = [L^3 T^{-2}],$$

and the only quantities available in the system are ε and k, we can determine the dependence of $E(k)$ on these parameters through dimensional analysis [5].

We construct a general function:

$$E(k) = C\,\varepsilon^{\alpha}\,k^{\beta} \tag{1.4}$$

where:

- ε has dimensions $[L^2 T^{-3}]$,
- k has dimensions $[L^{-1}]$,
- the energy spectrum has physical dimensions of energy per unit mass and per unit wavenumber, therefore $E(k)$ has dimensions $[L^3 T^{-2}]$.

Imposing that both sides have the same dimensions,

$$L^3 T^{-2} = \left(L^2 T^{-3}\right)^{\alpha} \left(L^{-1}\right)^{\beta}$$

Solving for α and β, we obtain:

$$\alpha = \tfrac{2}{3}, \qquad \beta = -\tfrac{5}{3}$$

In conclusion we obtain:

$$E(k) = C\,\varepsilon^{2/3}\,k^{-5/3} \tag{1.5}$$

which is the famous "five-thirds law." C is the universal Kolmogorov constant, experimentally determined to be about 1.5 [6].

This law indicates that energy is distributed among the different scales according to a negative power law $(-5/3)$, which means that the largest structures contain more energy than the smaller ones.

Experiments such as anemometric measurements in atmospheric flows [7, 8], analyses of turbulent flows in wind tunnels and turbulent jets [8], and numerical simulations such as DNS and LES [5, 3] have confirmed with good accuracy the validity of the law for flows with high Reynolds numbers.

To clarify the fundamental results of K41 theory also from a graphical point of view, we refer to the following figure:

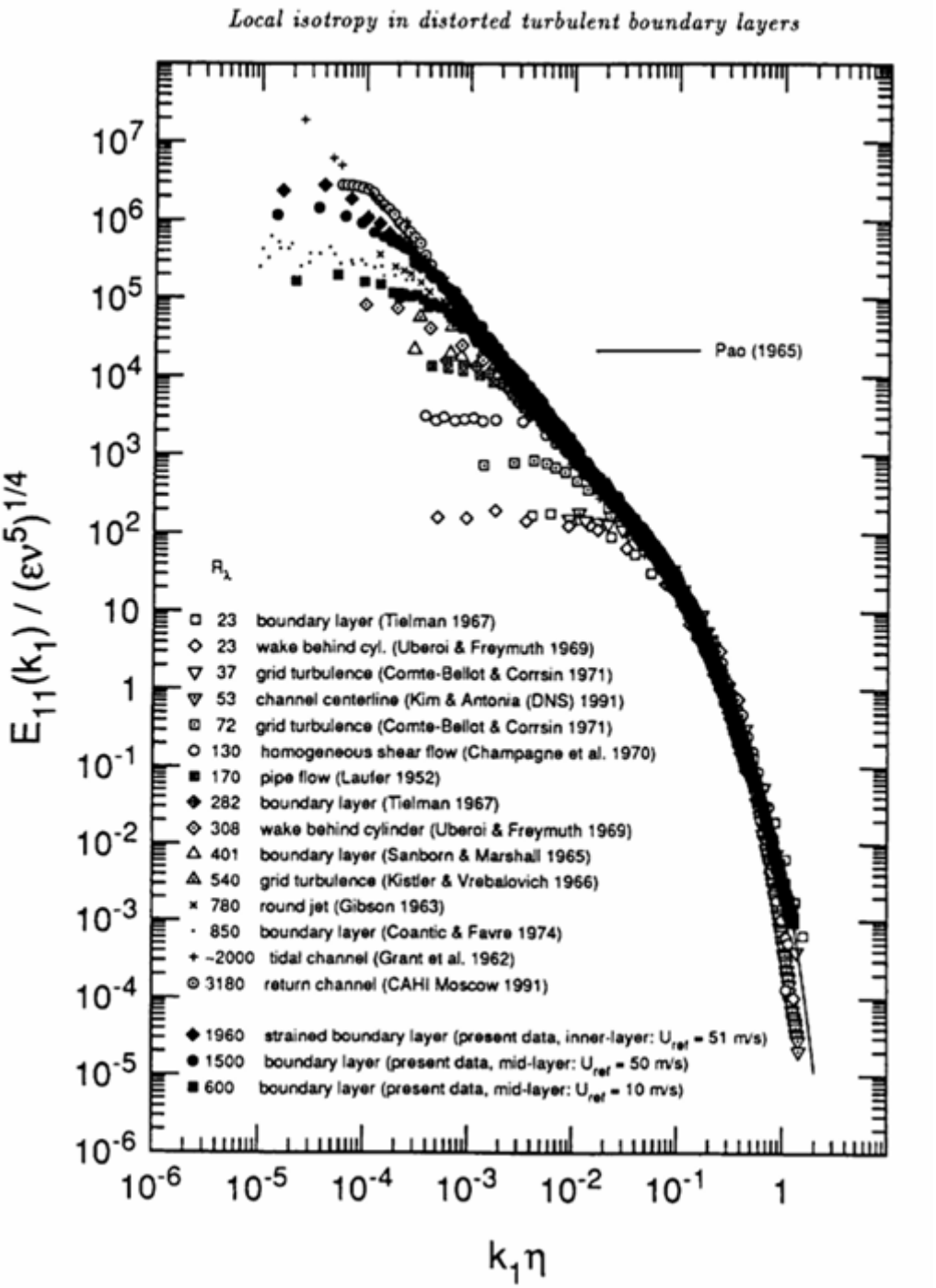

Figure 1.3: Several spectral scales from a large collection of wind-tunnel and geophysical experiments. The values of the Reynolds numbers here are based on the Taylor microscale. Image adapted from: S. G. Saddoughi and S. V. Veeravalli, J. Fluid Mech. 268, 333 (1994).

This figure represents a series of energy spectra, obtained from different experiments, in a normalized bilogarithmic plot. What immediately stands out is the superposition of the graphs as one approaches the smaller scales (larger k). This superposition is due to the universality of energy distributions at the small scales, as described by Kolmogorov.

From left to right, it is possible to observe how energy is distributed:

- The largest scales (smaller k) are those that receive, and therefore contain, most of the energy. The higher the Reynolds number, the greater the energy content.

- The "intermediate" scales are those of the inertial range, where a linear trend with slope equal to $-5/3$ is observed. Graphically, this confirms that the power law described by Kolmogorov is consistent with real cases. It should be noted that the linear trend is well defined only when the Reynolds number is very high, which demonstrates that Kolmogorov's theory requires the assumption of fully developed turbulence.

- At the end of the linear section a collapse occurs, because the system enters the dissipative range, where kinetic energy is rapidly transformed into heat.

1.3 Turbulent diffusion

Turbulent diffusion is another key phenomenon in the study of turbulence, and in our case it concerns in particular the relative dispersion of particles. It is a crucial aspect in many applications, such as the dispersion of pollutants in the atmosphere and in the oceans, mixing in industrial processes, and the dynamics of ocean currents.

Unlike molecular diffusion, which takes place on a microscopic scale due to the agitation of molecules (governed by Fick's law), turbulent diffusion is a large-scale phenomenon, determined by the vortical structures present in the flow.

One of the first scientists to effectively address the problem was, also in this case, Lewis Fry Richardson, in 1926. He observed that, instead of increasing linearly in time (as would happen in classical molecular diffusion), the separation between particles grows much more rapidly as they move apart, following instead a power law.

Consider, as an example, two distinct particles. Even if at the beginning they could disperse exclusively through molecular diffusion (especially if extremely close), sooner or later they will enter two different wind gusts, that is, two vortices, which will separate them further. According to the previously described multiscale theory (which, as I recall, had already been intuited at the time by Richardson himself), their separation will increase at an ever greater speed as they move apart, because it will be influenced by vortical structures of increasingly larger scale [9].

1.3.1 The Distance-Neighbor Graph

To formally describe the relative dispersion of particles, he adopted a statistical approach considering clusters of particles and introducing, for practical purposes, a mathematical tool called the Distance-Neighbor Graph (DNG).

Let us consider a set of N marked molecules, which we can call A, and define an arbitrary reference length h. Taking A as the origin, we can define $A_{n,n+1}$ as the number of particles whose distance ℓ from A falls within the interval $nh \leq \ell \leq (n+1)h$. The average of this quantity, over all the marked particles, will be defined as:

$$Q_{n,n+1} = \frac{1}{N}\big(A_{n,n+1} + B_{n,n+1} + C_{n,n+1} + \dots\big) \tag{1.6}$$

It is thus possible to obtain the values of $Q_{0,1}, Q_{1,2}, Q_{2,3}$ and so on, which represent the number of molecules per unit length classified according to their distance ℓ from the other molecules. Naturally, this concept can be extended to two-dimensional grids or three-dimensional volumes, by adopting cells of characteristic dimension h and counting the number of particles inside them.

It should be noted that, although h is an arbitrary length, it must be chosen with a certain criterion. This ensures that in the average $Q_{n,n+1}$ there is an adequate number of marked molecules so as to make the statistical result consistent.

From a graphical point of view, considering a one-dimensional grid, the (discrete) probability distribution $Q(\ell, t)$ can be plotted using the variable $Q_{n,n+1}$ on the ordinate axis and the length ℓ on the abscissa. Given the strong parallelism between Richardson's cluster of molecules and our cluster of radiosondes, we can directly take as an example a test carried out by our research group on July 5th, 2023 at the Chilbolton Observatory, in the context of the Wessex Convection (WESCON) campaign organized by the British Met Office.

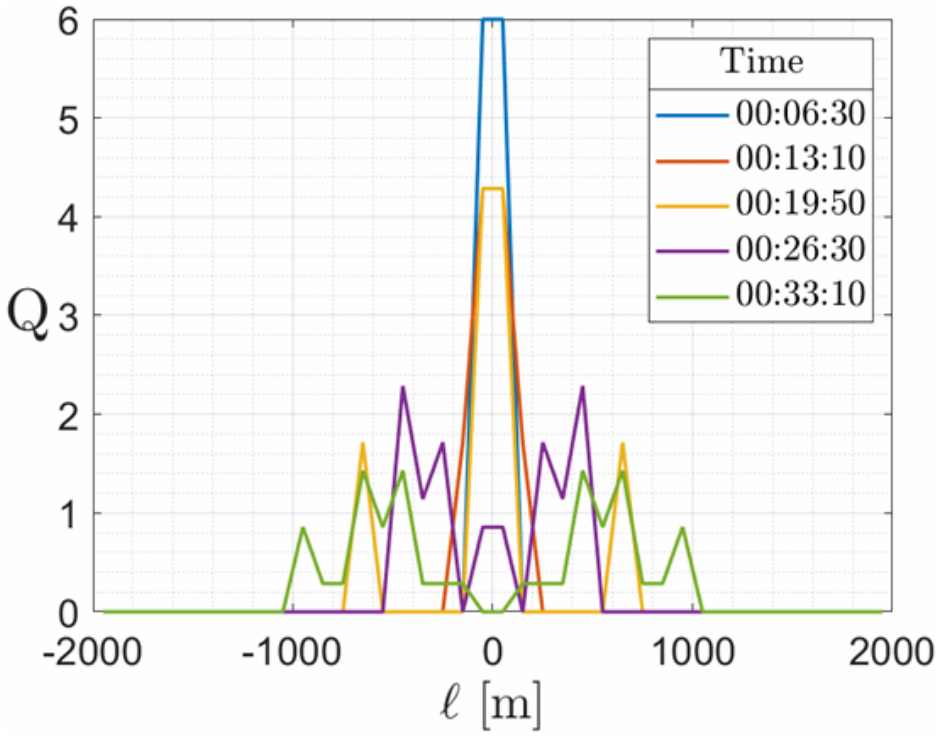

Figure 1.4: Measurements of relative distance during the free-floating experiment performed on July 5th, 2023 at the Chilbolton Observatory. The distributions were computed using the distance-neighbor graph function (Eq. 1.6) between the radiosondes inside a cluster. In this particular case, the parameter was set to $h = 100$ m.

It can be observed that, six minutes after the initial instant, the particles (radiosondes) are still clustered together, but in the subsequent plots they move progressively farther apart: the peaks lower and spread out, and the distribution gradually widens. If the process continued, the peaks would eventually smooth out and the distribution would approach a flatter profile.

We can also observe that, as time passes, the area enclosed between the curve Q and the abscissa axis ℓ remains constant. Hence, Q is expected to fulfill:

$$\frac{dQ}{dt} = \frac{d}{d\ell} \int_{-\infty}^{+\infty} \frac{dQ}{dt}\, d\ell = 0 \tag{1.7}$$

that describes the conservation of the quantity of particles distributed in different cells over time.

1.3.2 Richardson's laws

In his work, Richardson proposed a diffusion equation to define the probability density function $q(\ell, t)$ of the separation distances between particles of the marked cluster. Thus, $q(\ell, t)$ can be considered as the continuous limit of the distribution $Q(\ell, t)$ previously described. Assuming homogeneity and isotropy, such an equation can be written in the form:

$$\frac{\partial q(\ell,t)}{\partial t} = \frac{1}{\ell^2}\frac{\partial}{\partial \ell}\left(\ell^2 D(\ell)\frac{\partial q(\ell,t)}{\partial \ell}\right) \tag{1.8}$$

where $D(\ell)$ is the turbulent diffusivity, dependent on ℓ. Richardson decided to determine empirically the dependence of $D(\ell)$ on the scale ℓ, obtaining as a result the famous scaling law

$$D(\ell) \propto \ell^{4/3} \tag{1.9}$$

(Figure 1.5), which is one of the most emblematic laws of turbulence. This dependence is of crucial importance because it describes how turbulent diffusivity increases with the separation of particles, according to a power law very different from classical Fickian molecular diffusion [10].

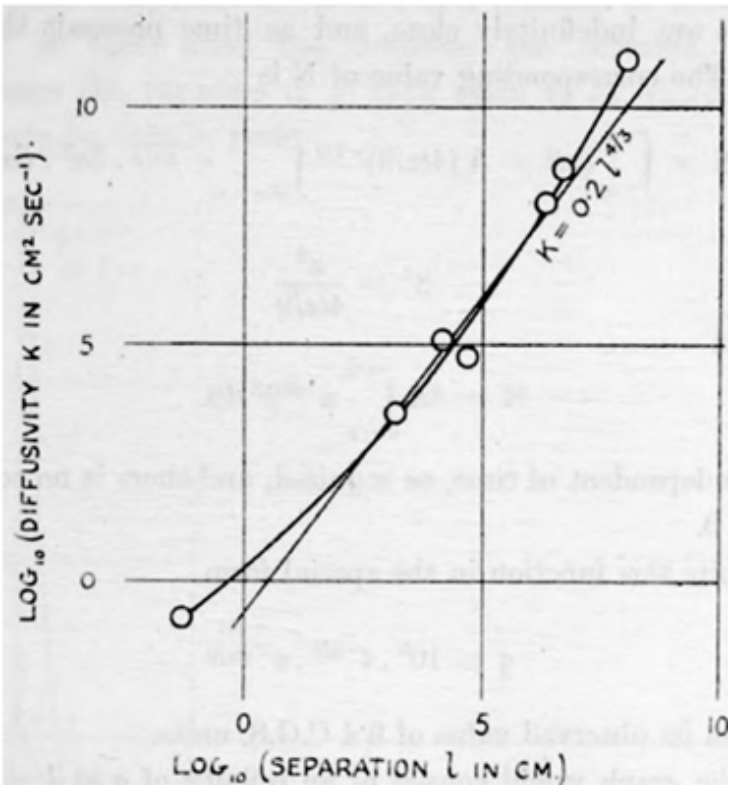

Figure 1.5: Figure from the original Richardson's paper [9] representing the experimental results of the diffusivity D measured as a function of ℓ, i.e., the distance separation between two particles. Starting from these data, Richardson proposed his famous 4/3 law drawn in the figure.

Using this expression of $D(\ell)$ and substituting it into the distribution equation (Eq. 1.8) it could be easily obtained a non-Gaussian distribution for particle separation:

$$q(\ell, t) \propto t^{-9/2} \exp\left(-\frac{C\ell^{2/3}}{t}\right) \tag{1.10}$$

This distribution implies that the mean square separation of particles grows in time as:

$$L^2(t) \equiv \langle \ell^2(t) \rangle = C_2 \, \varepsilon \, t^3 \tag{1.11}$$

Here, C_2 is the so-called Richardson constant and ε is the mean energy dissipation rate encountered earlier. Equation 1.11 represents the celebrated t^3 law of Richardson for pair dispersion and describes how the separation between two particles in a turbulent flow grows in time following a cubic dependence, a distinctive feature of fully developed turbulence.

Despite being formulated long ago, the actual value of the Richardson constant C_2 remains uncertain. Estimates from kinematic simulations place it between $O(10^{-2})$ and $O(10^{-1})$ [11, 12], even if in these models it is difficult to define a meaningful energy flux ε. Closure models, on the other hand, predict significantly larger values, typically of order $O(1)$ or higher [13]. More recent studies, through high-resolution three-dimensional direct numerical simulations (DNS) performed at CINECA by Boffetta and Sokolov [14], provide a more robust estimate of the Richardson constant, $C_2 \approx 0.5$.

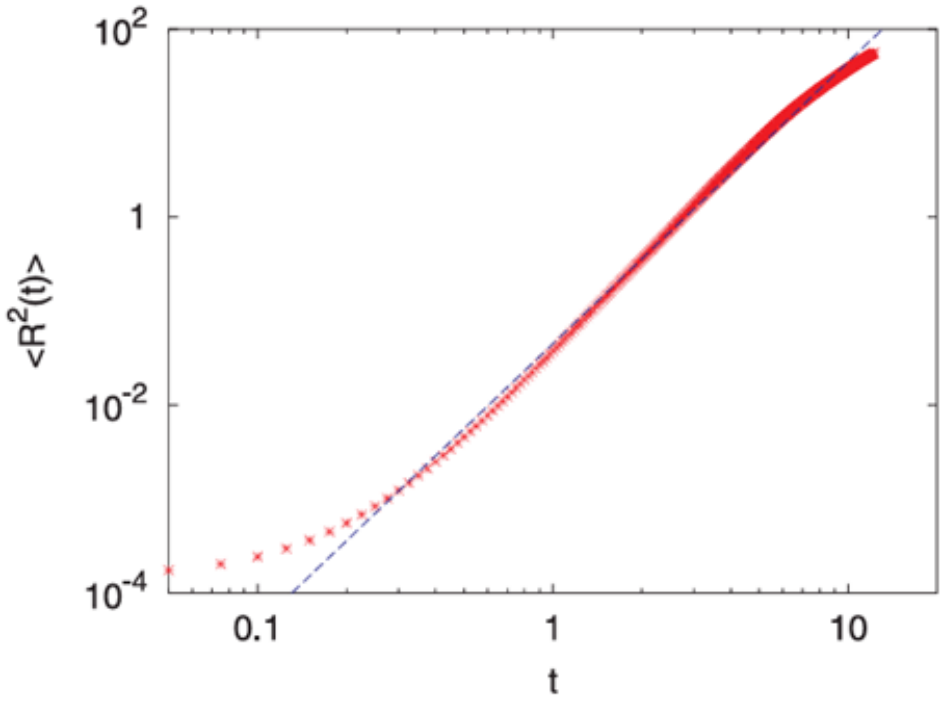

Figure 1.6: Relative dispersion $R^2(t)$ versus time. The blue line is Richardson's t^3 law (Eq. 1.11) [14].

Chapter 2

Boundary Layer and Clouds: Dynamic Mechanisms in the Atmosphere

The Earth's atmosphere is a very complex and dynamic system. It is made of several layers that interact with each other and affect climate and weather. In particular, the atmospheric boundary layer (ABL) is that part of the atmosphere closest to the Earth's surface: it is strongly influenced by the surface itself, as well as by the exchanges with the overlying layers. In this chapter, we will explore the dynamics governing the ABL, analyzing in detail the turbulent phenomena and the energy balance processes that determine its daily cycle. We will then see the crucial role of clouds, whose formation and development are directly linked to the atmospheric conditions, and we will also discuss how entrainment and turbulence influence their growth and evolution.

2.1 The Atmospheric Boundary Layer

The atmospheric boundary layer (ABL) is the lowest region of the troposphere, in direct contact with the Earth's surface. In this region, many interesting dynamics develop due to the interaction between air and surface: atmospheric turbulence, the formation of thermoconvective clouds, and the exchange of energy and matter are just a few examples. It is generally (but not always) limited from above by a thin vertical zone known as the inversion layer, where temperature increases with altitude.

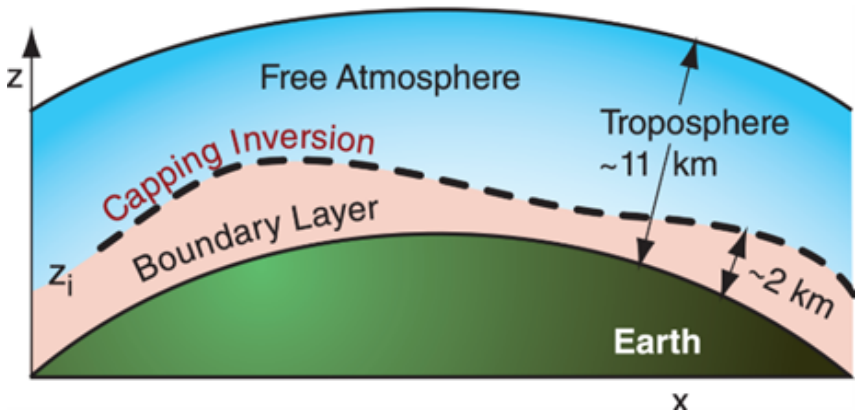

Figure 2.1: Vertical representation of the atmospheric boundary layer, showing the Earth's surface, the inversion layer and the troposphere. [15].

To introduce the subject, let us imagine being on a commercial airplane during takeoff and looking out the window. After gaining a few kilometers of altitude, one may notice changes in the surrounding environment, signaling that the aircraft is crossing the upper limit of the atmospheric boundary layer. Let's try to describe then the ABL through the perceptions of an ordinary passenger.

A first signal indicating that we have left the atmospheric boundary layer could be the crossing of a cloud base: thermoconvective clouds, (cumuli, for example) tend to form near this upper boundary. Indeed, warm and moist air, lifted by convective motions, rises until it encounters a more stable layer above, where cooling induces the condensation of water vapor and the formation of a cloud base.

If no clouds are present, one could still observe an improvement in visibility and in sky color. As anticipated, the layer of the troposphere above the ABL is generally more stable and less prone to convection, especially in the presence of a thermal inversion: being warmer than the air below further suppresses convective motions. Consequently, it acts as a barrier beyond which particles contained in the ABL (dust, pollutants, and water vapor) struggle to pass. This explains why, as one ascends, the sky changes from opaque and hazy to clearer and bluer, and why, when looking down, one often sees a layer resembling haze or smog.

2.1.1 The Role of Turbulence in the Evolution of the Boundary Layer

The central idea is that turbulence is not only a chaotic phenomenon within the atmospheric boundary layer (ABL), but it also plays a fundamental role in the formation, growth, and evolution of clouds. To understand this, we have to explain the generation of turbulence and its role in the daily cycle, as described by Garratt (1992) [16].

There are two main mechanisms that inject turbulent kinetic energy to our system. The first factor is radiative heating and cooling of the surface: daily temperature variations create a vertical thermal gradient, activating convective motions and thus generating what is known as convective turbulence. The second is surface friction: the no-slip condition implies that velocity drops to zero at the surface, producing vertical wind shear that, together with surface roughness, generates fluid-dynamic instabilities. This is known as mechanical turbulence.

To give an idea of the scales involved, it can be said that the largest turbulent structures have dimensions on the order of the ABL height (about 1–3 km), recalling the theoretical notion that the turbulence macroscale cannot exceed the external scale of the system. On the other hand, the smallest scales, at which atmospheric turbulent kinetic energy is dissipated by air viscosity, are on the order of a few millimeters [18].

Different types of ABL can be distinguished based on the stability that characterizes them. In particular, there is the clear weather ABL over land, the neutral ABL (Ekman layer), and the marine ABL. To clarify this distinction, we can begin by addressing the first one (Figure 2.2).

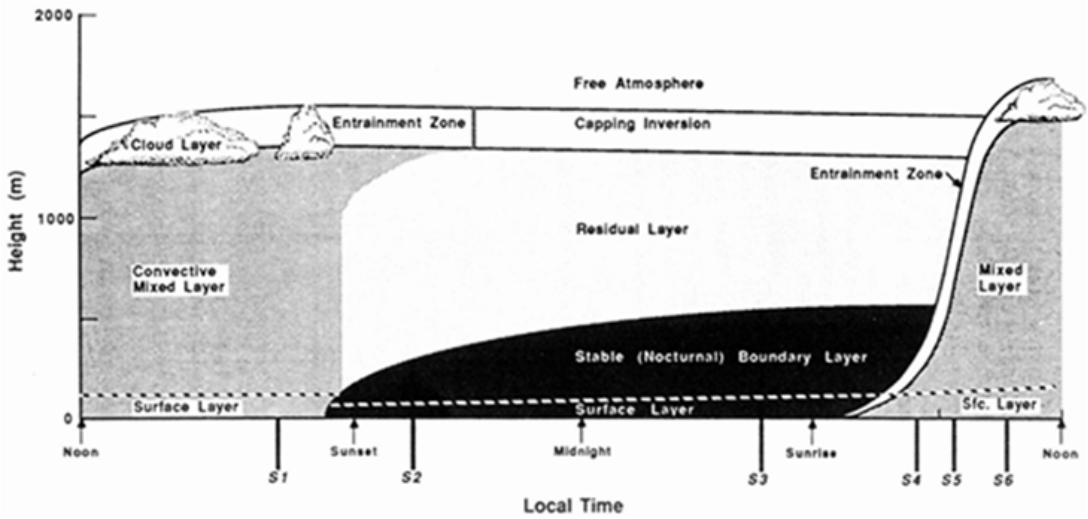

Figure 2.2: Daily cycle of the clear weather ABL over land.

The diurnal cycle starts at sunrise: the Sun warms the Earth's surface, creating a negative vertical temperature gradient $\mathrm{d}T/\mathrm{d}Z < 0$ and thus a buoyant ascent of air parcels. These convective motions, together with turbulence generated mechanically by surface friction, give rise to the so-called mixed layer (ML), and at the same time the ABL takes the name of *Convective Boundary Layer* (CBL). These ascending turbulent eddies are called thermals and are fundamental for cloud formation, because they transport heat, moisture, and aerosols upward. In the figure above, the entrainment zone is also shown, that is, a layer between the boundary layer and the free atmosphere, which will be discussed in detail in Section 2.1.3.

The ML continues to grow until early afternoon, then decreases slowly until sunset, when solar heating ends. From this moment, the opposite happens: the surface cools radiatively, reversing the temperature gradient (now positive, $\mathrm{d}T/\mathrm{d}Z > 0$) and damping convective motions. This new form of the ABL is called the *Stable Boundary Layer* (SBL), where the only turbulence left is mechanical. Above it, the ML is replaced by the residual layer (RL), which is connected to the free atmosphere through a capping inversion zone. It should be noted, however, that the SBL can also show turbulence, even if only intermittently, but in any case its intensity decreases substantially with height.

Now that we have a better idea of the concept of stability, it is easy to explain the distinction from the other two categories. The Ekman layer (also called neutral ABL over land) appears when clouds or strong winds make solar radiative heating less effective at the surface, keeping the daytime temperature gradient essentially zero ($\mathrm{d}T/\mathrm{d}Z \approx 0$) and leaving wind shear as the main source of turbulence. The marine ABL, similarly, shows a weak diurnal cycle: solar radiation is partly reflected and partly refracted by the sea, and oceanic mixing together with the high heat capacity of the ocean keeps sea-surface temperature almost constant. Consequently, turbulence here is generated almost exclusively by surface roughness, which in this case is made by waves, thus dynamic elements that are more variable and less predictable than terrestrial obstacles. It must still be considered that in some conditions there can be strong land–sea thermal contrasts that produce significant advection of heat.

2.1.2 Energy Issues

From what has been discussed so far, it is clear that the structure of the ABL is strongly dependent on what happens at the surface, in particular on its heating or cooling. In principle, we can say that the energy fluxes across the surface are in balance ($E = 0$), unless the energy is used for phase changes at the surface.

Considering the heat fluxes [W/m^2], the energy balance can be expressed as [16]:

$$E = Sw(1 - \alpha) + Lw + SHF + LHF + G \tag{2.1}$$

where:

- Sw is the incoming shortwave radiation flux. It has strong diurnal and seasonal variability, depending on geographical location, cloud cover, and the presence of aerosols.
- α is the surface albedo, that is the fraction of solar radiation reflected.
- G is the soil heat flux. It depends on the temperature gradient between the surface and the subsurface. This term is often the smallest in the surface energy balance and, on a daily scale, may be negligible because it tends to cancel out over time.
- Lw is the net longwave radiation. The outgoing radiation can be approximately expressed with the Stefan–Boltzmann law for an emissive body,

  $$Lw_{out} = \varepsilon \sigma T^4,$$

  while the incoming radiation originates from the atmosphere itself and from reflection by clouds and greenhouse gases, and is much more complex to evaluate.

Finally, SHF and LHF are the sensible and latent heat fluxes, respectively. They can be expressed as:

$$\mathrm{SHF} = \rho \, c_p \, C_h \, V \, (\theta_{\mathrm{air}} - \theta_{\mathrm{sup}}) \tag{2.2}$$

$$\mathrm{LHF} = \rho \, L_v \, C_h \, V \, (q_{\mathrm{air}} - q_{\mathrm{sup}}) \tag{2.3}$$

where ρ is the air density near the surface, c_p is the specific heat at constant pressure, C_h is the heat exchange coefficient (a typical value is 0.001), L_v is the latent heat of vaporization (2.5×10^6 J kg^{-1}), and V is the absolute wind speed, which is essentially a measure of the production of mechanical turbulence near the surface. As these formulas show, SHF and LHF play a crucial role in the surface energy balance: they represent how much heat and moisture, once exchanged with the surface, will then be transported and redistributed by atmospheric turbulence within the ABL.

To express the ratio between sensible and latent heat fluxes, the Bowen ratio β is used, defined as:

$$\beta = \frac{SHF}{LHF} \tag{2.4}$$

A high value of β indicates that the surface transfers more sensible than latent heat (typical of dry environments), while a low value of β indicates that most of the available energy is used for evaporation (typical of wet or aquatic surfaces). Moreover, if one adopts the convention of positive fluxes directed into the surface, it can be stated that both fluxes are generally positive during unstable daytime stratification and negative during stable nighttime stratification [16].

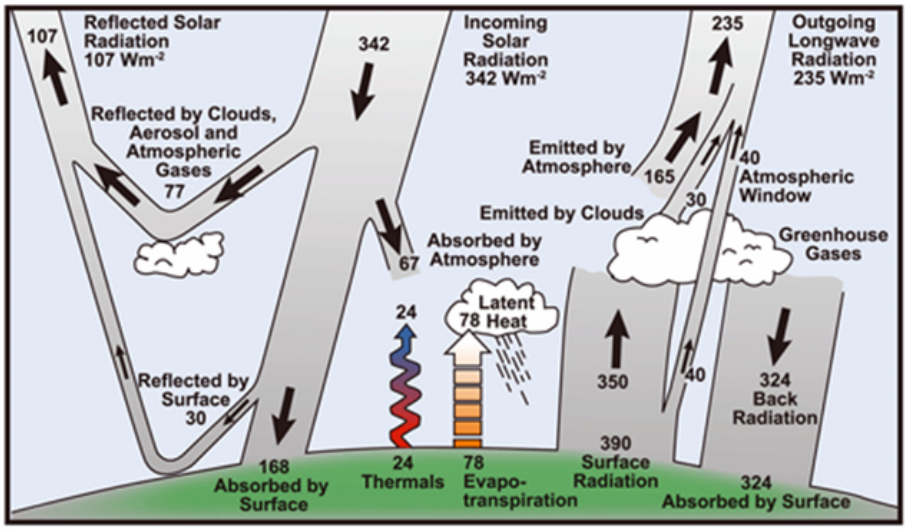

Figure 2.3: The heat balance of the Earth–atmosphere system, globally and annually averaged [16].

2.1.3 Entrainment as a Mechanism of ABL Growth

The ABL undergoes large variability in depth, from a few tens of meters to more than 3000 m, depending on the time of day, atmospheric conditions, season, geographical location, land/ocean, and synoptic influences [17]. What all these cases have in common is the way in which the thickening of the atmospheric boundary layer occurs, namely through two distinct mechanisms: encroachment and entrainment.

The first is a process that we can almost call "passive," since it is a simple thermal expansion of the underlying layers caused by surface heating. This expansion affects the layers above, lifting them and thus gradually increasing the ABL. This phenomenon is particularly evident in the early morning, but as the day progresses (and if the atmospheric conditions allow it) convective motions develop and the dominant process in the ABL growth shifts from encroachment to entrainment.

Quoting P. Dimotakis [19], we can provide a general definition of the entrainment phenomenon:

> "Entrainment phenomenon is typical of the atmosphere, and it occurs whenever a turbulent stream, flows by a non-turbulent stream. It is an irreversible process by which a fluid particle approaches to the turbulent zone and acquires vorticity becoming part of it."

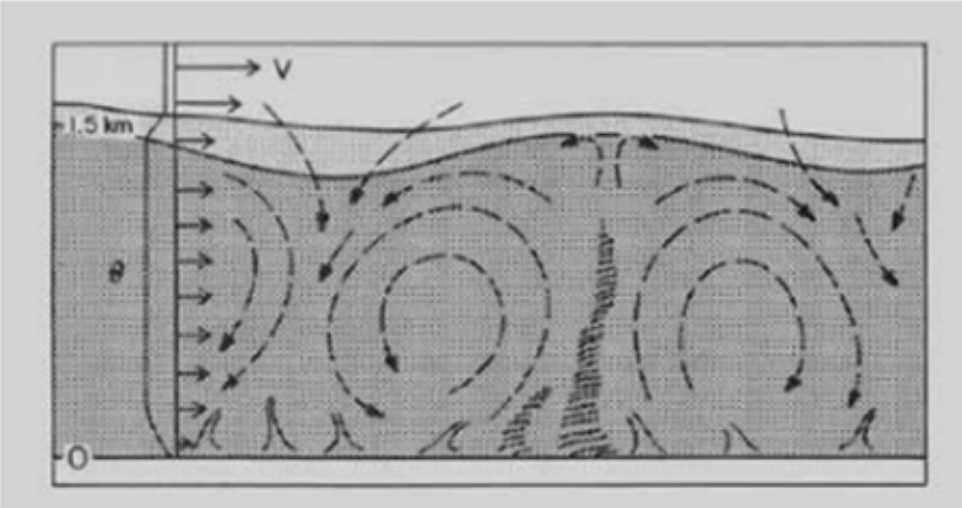

Figure 2.4: Representation of convective boundary layer circulation and entrainment of air through the capping inversion [20].

But how does this affect our case of the atmospheric boundary layer? Consider the dynamics of the convective motions that characterize the mixed layer. During the day, ascending thermals may reach the capping inversion and, in some cases, temporarily overshoot it. This generates turbulence in the transition zone between the ABL and the Free Atmosphere and, as stated by P. Dimotakis, the warmer, drier and non-turbulent particles from the upper layer will be entrained into the lower layer, increasing its depth.

The rate at which free-atmosphere air is incorporated is called entrainment velocity, and it is expressed as:

$$w_e = A \frac{SHF}{\rho c_p \Delta\theta} \tag{2.5}$$

where A is an empirical coefficient ($\sim$ 0.2–0.3 in convective conditions), while $\Delta\theta$ represents the difference in potential temperature between the ABL and the overlying free atmosphere. This formula highlights the main factors that influence the intensity of entrainment and, consequently, the growth of the atmospheric boundary layer:

- The intensity of surface heating (SHF): a greater heat input from the surface strengthens turbulence and mixing, favoring entrainment and ABL growth.
- The intensity of the capping inversion ($\Delta\theta$): a strong thermal inversion acts as a barrier to mixing. When the inversion is strong (for instance, in the early morning), the entrainment zone (EZ) is thinner and the ABL grows more slowly.

2.2 Clouds

The scientific study of clouds began between the 18th and 19th century, when the English pharmacist Luke Howard developed a classification system that became widely accepted, categorizing clouds by height and shape with Latin terms still used today. At the same time, another chemist, John Dalton, focused on clouds as well, describing them not as independent entities but as systems of particles under the continuous action of Earth's gravitational field [21].

These were the forerunners of modern cloud physics, where clouds are far from being mere "airy nothings", but instead they play a fundamental role in Earth's climate system.

First, they regulate the hydrological cycle by condensing atmospheric moisture and returning it to the surface as precipitation, in the form of liquid water or ice. Then, as discussed in Section 2.1.2, clouds also play a key role in the planet's energy balance, affecting both shortwave and longwave radiation. On the one hand, high, thin clouds can have a warming effect by trapping infrared radiation emitted by the Earth while letting most incoming solar radiation pass. On the other hand, low, thick clouds can cool the surface mainly by reflecting incoming solar radiation. Considering the mean net energy balance due to clouds, the latter effect dominates, leading to a net cooling that lowers surface temperatures by about 5 °C. [22].

With this in mind, it should be clear why being able to study clouds formation and evolution turns out to be a crucial achievement.

2.2.1 Warm clouds origin

The classification currently in use is still based on that proposed by Luke Howard. The World Meteorological Organization (WMO) divides clouds into ten genera, classifying them according to the altitude of the base and their shape [21].As illustrated in Figure 2.5, we can distinguish between layered clouds (on the left) and vertically developed clouds (on the right), the latter often extending over a wide range of altitudes.

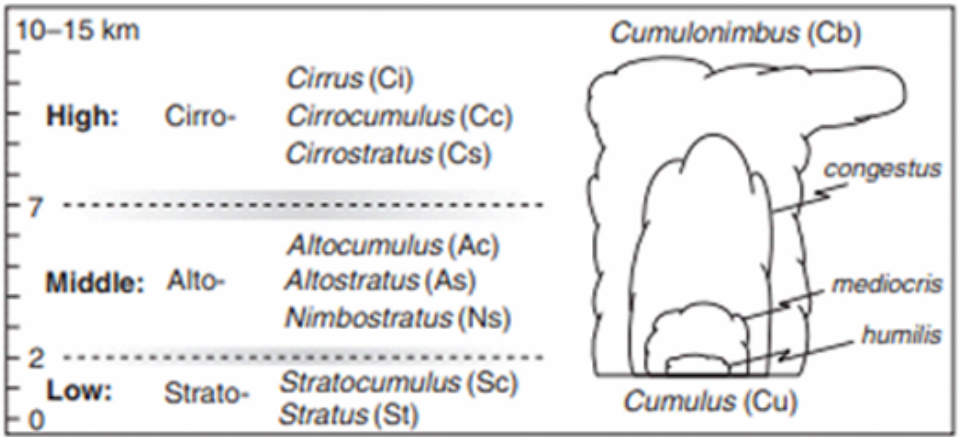

Figure 2.5: Classification currently adopted for cloud types [21].

In this work, we will refer to a subgroup of clouds called *warm clouds*, formations composed exclusively of water in liquid form and whose base is generally located below 2000 m. Unlike cumulonimbus clouds, which can develop in warm and humid conditions but can then grow vertically into much colder layers (where ice and hail can form), warm clouds remain confined to temperature intervals above zero, so they do not contain snow or ice crystals. Among those in Figure 2.5, only cumulus, stratocumulus, stratus, and, in some cases, nimbostratus fall into this category.

The origin of these clouds has to be found in the lifting of moist air masses, whether produced by synoptic-scale turbulence, by local convection generated by surface heating, or, more simply, by orographic lifting action. As the parcel ascends, it expands ($dp/dz < 0$) and cools adiabatically ($dT/dz < 0$) until saturation is reached; at that point condensation can begin, giving rise to cloud droplets.

However, it is important to clarify that this process could not occur without aerosol particles (e.g., sea salt, organic compounds, mineral dust, and soot/black carbon). In fact, looking more closely inside a rising parcel, a droplet does not arise spontaneously; rather, water vapor must condense on water-soluble aerosols, typically a few hundredths of a micrometer in diameter, which act as cloud-condensation nuclei (CCN).

Because many droplets form at the same time and must share a limited amount of vapor, growth by condensation alone is slow and inefficient. As a consequence, warm clouds often remain for long periods in a state reducible to a colloidal suspension, in which numerous small droplets stay suspended within the cloud and interact only weakly. However, this condition can break down when processes that generate relative motion, such as turbulence or differences in fall velocity, come into play and lead to droplet collisions. In that case, droplets can merge through a process known as collection (collision and coalescence), which gradually increases their diameter and may eventually produce rainfall.

Studying the bridge between the condensation process and the collection is one of the central challenges in cloud microphysics and is known as the *growth gap*. As illustrated in Figure 2.6, condensation is effective only at very small radii, whereas collection processes become significant only when droplets exceed roughly 20 micrometers.

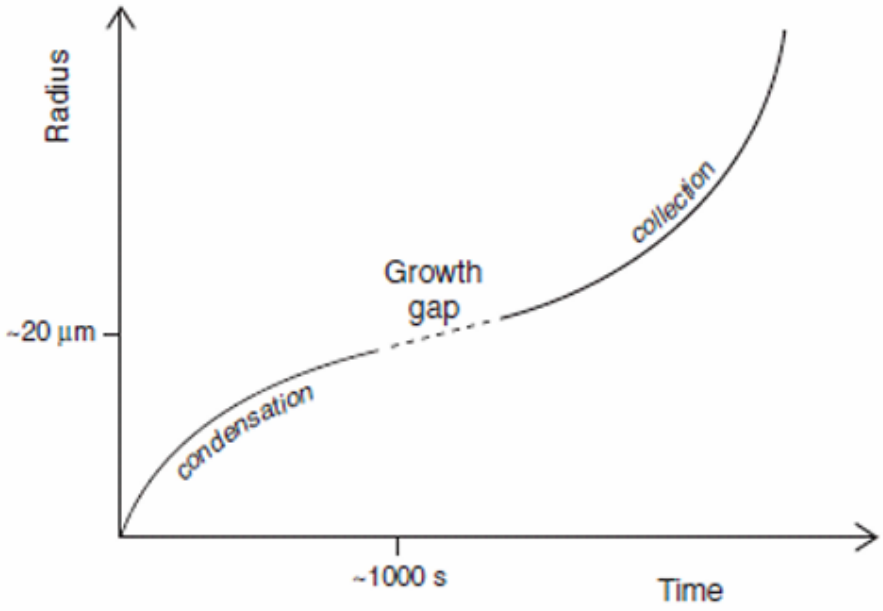

Figure 2.6: Relative growth of droplets by condensation and collection; droplets with a radius smaller than 20 μm grow by condensation, the growth gap represents the uncertain processes by which droplets increase to the size needed for the collection process [23].

The intermediate size range is difficult to achieve, and how droplets manage to cross the gap remains a subject of active research. The most widely accepted theory identifies as determining factors the initial number and distribution of aerosol particles within the ascending air mass: when only a few nuclei are available, vapor competition is weaker and droplets can reach the critical sizes for collision more easily; by contrast, in environments with abundant aerosols one might expect the opposite, namely that growth would stall before bridging the gap [23]. However, although some experimental observations comparing aerosol-poor air masses (such as those in marine environments) with more polluted

ones (such as continental air masses) have supported this theory, it is not fully confirmed, since an excess of aerosols may still allow the breakdown of colloidal stability and the initiation of coalescence.

2.2.2 CCN activation

It now appears clear how the key role in cloud generation, and thus in the initial droplet number and size distribution, is played by condensation nuclei. However, not all aerosol particles are able to act as a CCN: only particles that surpass a critical threshold of growth can be activated, while the others remain interstitial haze droplets.

When an air parcel rises, it expands and cools, and thus sees an increase over time in the environmental supersaturation $S_{\text{env}}(t)$, which becomes positive upon passing through the cloud base. On the other hand, each aerosol particle has its own critical supersaturation S_c, which is determined by its composition, dry size, and water solubility. When the parcel's supersaturation exceeds the particle's threshold, $S_{\text{env}}(t) > S_c$, then activation can occur, and, as stated above, it will be the larger and more soluble particles (lower S_c) that activate first, while the smaller and less soluble ones (higher S_c) will require more extreme conditions.

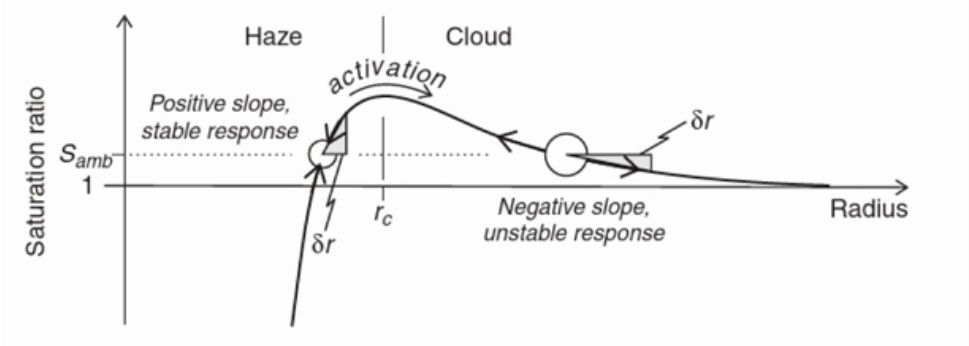

Figure 2.7: Activation process in Köhler theory. The abscissa shows the particle radius, while the ordinate shows the environmental saturation. The process takes place in a supersaturated environment, with $S_{\text{env}} > 1$ [23].

Considering Figure 2.7, we can also see how, after reaching its critical point (that is, the pair S_c and r_c on the Köhler curve), the particle can no longer remain in stable equilibrium and enters self-sustained (negative slope) condensational growth, transitioning from a haze droplet to a cloud droplet.

This behavior is described by Köhler theory, which postulates the presence of two contrasting effects [23]:

- The Kelvin effect, whereby greater curvature increases surface tension, promoting the detachment of water molecules through evaporation;
- The Raoult effect, whereby dissolved solutes reduce the equilibrium vapor pressure, encouraging condensation.

The combination of these two contributions results in a curve with a maximum (Figure 2.7), known as the *critical supersaturation* $S_{\max}$, at a corresponding critical radius

r_c. As already mentioned, below r_c droplets are stable, while above it growth is unstable, increasing the droplet size. Mathematically, the Köhler equation can be written as:

$$S_K = 1 + \frac{A_K}{r_d} - \frac{B_K, iN_s}{r_d^3}, \tag{2.6}$$

where A_K and B_K are coefficients that depend on temperature and surface tension, i is the van't Hoff factor accounting for solute dissociation, and N_s is the solute content of the particle.

In real conditions, activation depends not only on these particle properties, but also on the external dynamics of the ascent motion. Stronger updrafts produce higher supersaturation peaks, also allowing smaller particles to activate, while weaker updrafts promote the activation only of larger and more soluble aerosols.

This sequence, illustrated in Figure 2.8, can serve as a summary of what has been said so far. On the left, the evolution of supersaturation is shown for a rising air parcel: the curve first increases (from negative to positive values when passing through cloud base), reaches a peak, and then decreases again. On the right, we can observe the activation of particles of different sizes: the larger one activates first, the intermediate one at a later stage, while the smallest may not activate if the supersaturation peak is insufficient.

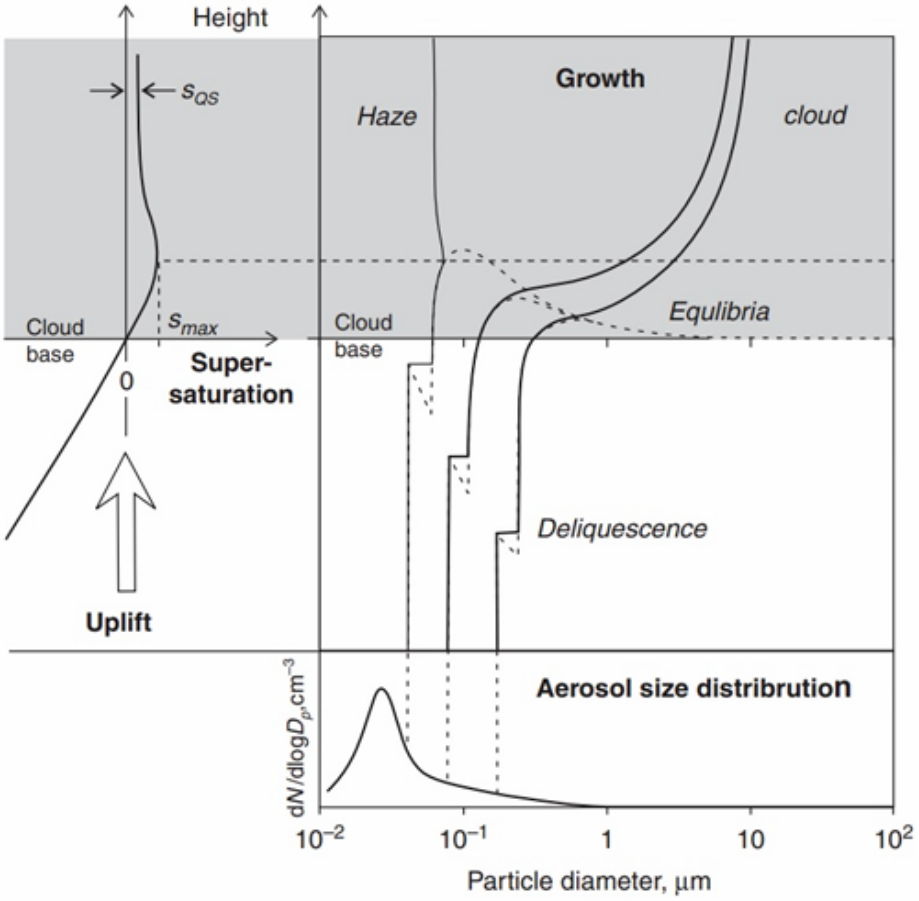

Figure 2.8: Left: supersaturation evolution in a rising parcel. Right: growth of three particles of different sizes, showing how activation depends on both size and supersaturation peak [23].

In conclusion, the balance between activated and non-activated particles defines the initial cloud droplet spectrum, which, together with turbulent atmospheric dynamics, directly influences the subsequent evolution of the system—namely, condensational growth, the efficiency of collision–coalescence, and, finally, the radiative and dynamical properties of the generated cloud.

2.2.3 Turbulence effects and droplets motion

Clouds are systems in rapid evolution, and inside them are the turbulent phenomena to dominate on different temporal and spatial scales. In the middle of these turbulences, the droplets do not have a passive role, on the contrary, they continuously exchange mass (condensation/evaporation), momentum (viscous drag) and energy (latent heat) with the surrounding flow, thus reflecting on the microphysical evolution [27] discussed in the previous section. An example is given by the fact that the continuous effect of phase transitions (condensation and evaporation), releasing or absorbing latent heat, produce buoyancy variations that can influence cloud-scale motions.

Large turbulent eddies, of characteristic size on the order of 10^2 m, can transport and diffuse droplets across the volume, but because of the difference of three orders of magnitude of the density of liquid water compared with that of air, the inertia of droplets cannot be neglected. In fact, this inertia prevents droplets from responding instantaneously to rapid velocity fluctuations in the surrounding flow, making the interaction between turbulence and droplets intrinsically multiscale and non-local [28]. Therefore, despite their small radii ($r < \eta$, with η the Kolmogorov length), droplets experience an inertial response that can be characterized by the timescale

$$\tau_p = \frac{2\rho_p r^2}{9\mu}, \tag{2.7}$$

where r is the droplet radius, ρ_p the liquid water density and μ the dynamic viscosity of air. Comparing τ_p with the Kolmogorov time τ_η, we can define the Stokes number,

$$St = \frac{\tau_p}{\tau_\eta}, \tag{2.8}$$

which characterize different inertial regimes: for $St \ll 1$ droplets closely track the air motion behaving as Lagrangian fluid tracers, for $St \gg 1$ inertial decoupling becomes important, and around $St \approx 1$ preferential concentration with maximum relative velocities are expected [29]. The inertial response time also determines the terminal velocity in a quiescent fluid, expressed as

$$V_T = \tau_p g, \tag{2.9}$$

where g is the gravitational acceleration. With its normalization by the Kolmogorov velocity v_η, we can also obtain the non-dimensional terminal velocity

$$Sv = \frac{V_T}{v_\eta} = \frac{\tau_p g}{v_\eta}, \tag{2.10}$$

where v_η is the Kolmogorov velocity scale. This parameter determines the relative importance of gravitational settling compared to turbulent motions: $Sv \gg 1$ indicates gravity-dominated motion and reduced turbulent interaction, whereas $Sv \ll 1$ implies negligible settling effects; in many cumuliform clouds these two contributions can be comparable

giving overall a $Sv = \mathcal{O}(1)$. The combined dependence of droplet dynamics on both the Stokes number and the non-dimensional terminal velocity can be visualized in the St–Sv diagram of Fig. 2.9.

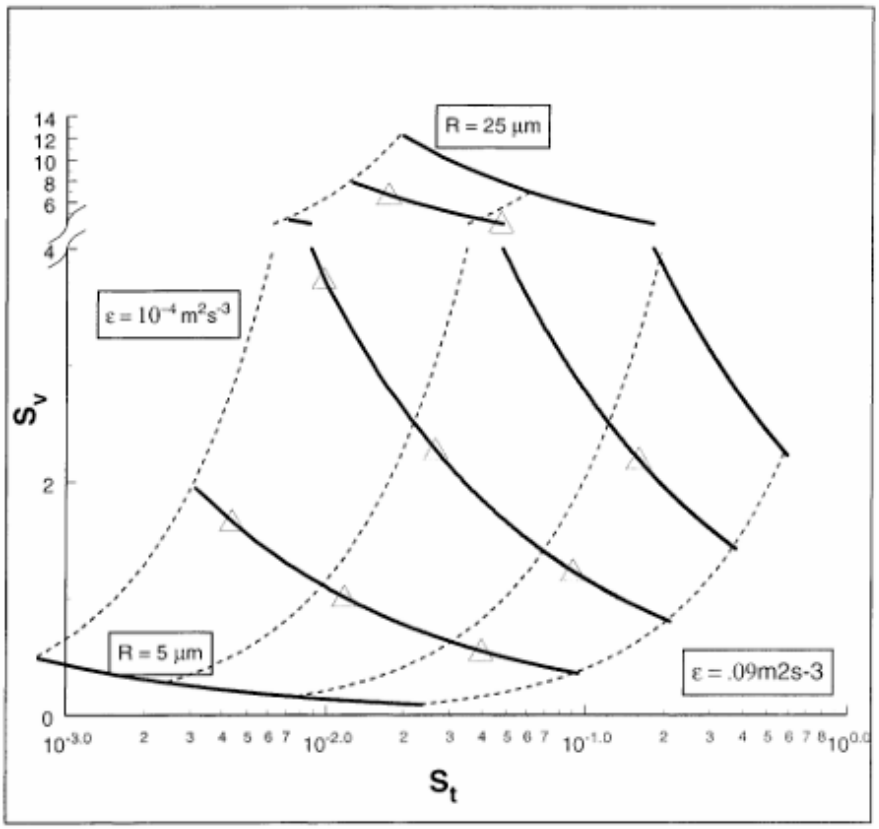

Figure 2.9: Sv–St diagram for typical cloud-droplet sizes; dashed families represent increasing turbulence intensity (parameterized by the dissipation rate ε), while solid curves correspond to constant droplet radius [29].

Finally, the effects discussed above can be expressed more formally through the equation of motion for a small droplet in a turbulent flow:

$$\frac{dv_i}{dt} = \frac{u_i - v_i}{\tau_d} + g_i \tag{2.11}$$

where v_i represents the droplet velocity in the i-th direction, u_i is the local flow velocity and g_i is the gravitational acceleration. When the Stokes number is small ($St \ll 1$), meaning the droplet is strongly coupled to the airflow, the equation simplifies to:

$$v_i \approx u_i + \tau_d g_i - \tau_d a_i \tag{2.12}$$

where a_i represents the Lagrangian acceleration of the fluid at the droplet's location.

This expression shows that droplets generally follow the surrounding air motion, but they also possess a component of relative velocity induced by two primary effects: gravitational settling, which drives them downward with respect to turbulent eddies, and inertia, which limits their ability to respond instantaneously to rapid velocity fluctuations in the airflow [30].

2.2.4 Entrainment in clouds and its consequences

As seen in the discussion of boundary layer growth, the entrainment phenomenon consists of an irreversible process by which ambient air, initially located outside the turbulent region of a cloud, is progressively incorporated into it and becomes part of the turbulent flow field. It is a phenomenon of fundamental importance in the dynamics of clouds, where the mixing it produces causes a widening of the droplet size spectrum [19].

A conceptual representation of the cloud–clear air interface is shown in Fig. 2.10. At the initial time, the interface appears relatively sharp. As turbulence develops, however, a transition layer emerges: on the cloudy side, the liquid water content decreases outward (dilution zone), while on the side of the "dry" environment a humid shell appears [32].

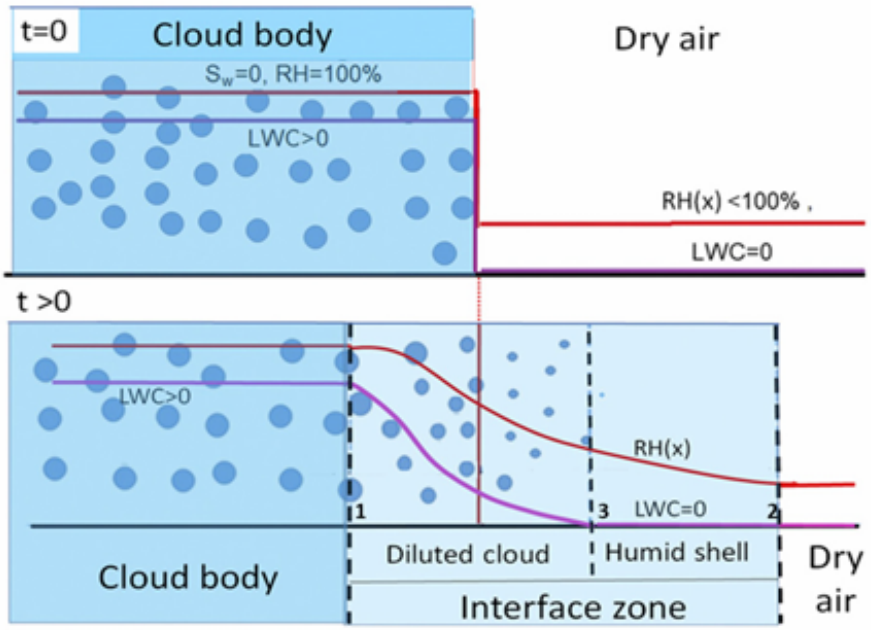

Figure 2.10: Idealized sketch of the evolution of the cloud–dry air interface. At $t = 0$ (top), the separation between cloudy and clear air is sharp. At later times (bottom), turbulent motions generate a mixed region consisting of a dilution zone and a humid shell [32].

The entrainment process involves a large range of scales. The large eddies are those that engulf masses of dry air (engulfment), which are subsequently stretched into elongated filaments (stirring). Then, when these filaments reach scales of the order of η, the Kolmogorov length, molecular diffusion can act by homogenizing the mixture. Besides diluting the liquid water content, entrainment can also encourage microphysical activity. For instance, in shallow cumulus, vortical structures can transport volumes of supersaturated air into the cloud interior, enhancing local supersaturation and increasing the number of potential cloud condensation nuclei (CCN) to be activated [33].

The impact of entrainment on droplets microphysics can be evaluated using the Damköhler number:

$$Da = \frac{\tau_r}{\tau_s}, \tag{2.13}$$

defined as the ratio of a turbulent timescale τ_r to a microphysical timescale τ_s [31]. When $Da \gg 1$, turbulent fluctuations are slow compared to characteristic times of condensation

and evaporation, producing inhomogeneous mixing: some droplets evaporate completely while others remain unaltered, reducing the number of droplets but leaving the mean droplet size practically unchanged. In an opposite manner, for $Da \ll 1$, turbulent mixing is much faster than thermodynamic processes, and the result is homogeneous mixing: evaporation acts uniformly on all droplet sizes, slightly reducing their diameters without altering their total number.

Chapter 3

Radiosondes

Considering the atmospheric modeling, the representation of cloud processes remains one of the most challenging aspects of numerical simulations. In large-scale climate models, the most advanced setups achieve grid sizes on the order of a few kilometers [34], and such resolution is still too coarse to capture the cloud microphysics. In this case, for phenomena that develop on scale of meters such as droplet activation, phase transitions, and turbulent mixing, these models rely to parameterizations of convection and subgrid turbulence which are indispensable but introduce necessary approximations that are misleading for the cloud representation.

As a counterpart, Direct Numerical Simulations (DNS) resolve the full turbulent cascade without the need of parameterizations. This approach is undoubtedly the best to understand fine-scale dynamics, but it is restricted to computational domains of only a few meters [35] due to the enormous computational cost. As a result, DNS cannot reproduce the multi-kilometer interactions inside clouds, while climate models cannot reach the scales at which some essential physical processes occur.

This scale gap is a major limitation for both approaches. Thus, bridging these scales is a current limitation and would require more efficient numerical models. For now, however, the most widely pursued way is to use complementary, consolidated experimental observations that can provide reliable atmospheric measurements. A variety of instruments are used for cloud observations, including ground-based meteorological stations, radar and lidar, satellites, and manned or unmanned aerial platforms (such as aircraft, helicopters, and tethered lifting systems), but the category most relevant to us is weather balloons.

Indeed, this thesis will focus on the development and implementation of an in field measurement system that, while sharing some similarities with conventional balloon–radiosonde systems for atmospheric sounding, introduces several innovative aspects. The idea was developed during the writing of a proposal for a European Horizon 2020 Marie Skłodowska-Curie project, approved in 2016 (H2020 MSCA ITN ETNCOMPLETE, GA675675: Innovative Training Network on Cloud-MicroPhysics Turbulence-Telemetry): an innovative system of mini atmospheric radio probes [37], designed to be carried aloft by biodegradable helium-filled balloons and to passively float in the atmosphere, tracking small-scale cloud fluctuations with a Lagrangian approach.

First, let us explain what it means to adopt a Lagrangian approach. In fluid dynamics, to study a motion in an Eulerian way means to analyze the properties of a flow relative to a fixed control volume, and therefore describing how variables like pressure, temperature, velocity and others change at specific points in space over time. Therefore, rather than tracking the movement of individual fluid particles, this method provides a snapshot of

the flow field and its evolution in time. In contrast, the Lagrangian approach follows the motion of individual fluid particles as they travel through the flow. In this case, it is instead precisely the characteristics of each single particle that are tracked over time.

The goal is then to behave like instrumented floating particle devices that track three-dimensional Lagrangian trajectories after their release into the atmosphere. The radiosondes need to be passively transported by the turbulent flow, perturbing it as little as possible. For this purpose, they must be as small as possible to minimize inertia and have a minimal volume compared to the trajectory they follow during the flight.

Conventional radiosounding devices are not designed to accurately track the turbulent behavior (especially at small scales) of airflow. Commercial devices such as the Vaisala RS41 (220–300 g, 75 mm diameter, 195 mm height) or the NCAR–NOAA Global Hawk dropsonde (167 g, 30.5 cm length, 4.6 cm diameter with a 20 cm parachute) are designed to provide exclusively vertical profiles of temperature and humidity during their ascent or descent, and do not follow Lagrangian trajectories. At a much larger scale, NOAA Low Altitude Balloons (11 feet in diameter, constant volume) can serve as markers to sample lower–tropospheric turbulence over long distances [38], but they are not intended to resolve the small-scale motions.

Our radiosonde, on the contrary, has significantly different characteristics to reach the smallest scales. As will be explored in detail later, the weight of the battery-powered electronic board has been brought to less than 20 grams, including the battery. Consequently, the balloon, which is much larger than the radiosonde itself, has been carefully sized taking count of the payload weight and the target floating altitude. This applies not only to the first prototype, which has already been tested and validated over the years, but also to the second version, where the PCB (Printed Circuit Board) has been further optimized in terms of weight and size. These properties make the sonde a good candidate to play the role of a Lagrangian particle, which, thanks to a set of integrated sensors, can measure three scalar parameters (pressure, temperature, humidity) and four vectorial quantities (position, velocity, acceleration, magnetic field) along its trajectories.

Another important aspect that must be considered is the life cycle of a radiosonde. Although recovering and reusing the probes would be ideal, at least for now they are designed to be expendable, and they are not intended to be recuperated once their journey, which can last many hours, ends on the ground. This choice has led to two key architectural features:

- First, since the probes are not recovered, the data they collect during flight must be transmitted in real time, sending data packets to one or more ground stations with a low-power radio system;

- Second, because of their disposable nature, a path for environmental sustainability must be adopted. To minimize the ecological impact, a biodegradable material has been used for balloons, making their design and construction a real challenge. In addition, future developments aim to explore sustainable alternatives also for the PCB and for the power system as well.

A dedicated chapter will discuss the use of biodegradable balloons.

Finally, but not less important, these sondes are not designed to be launched alone, but in clusters. Deploying multiple mini-expendable radiosondes for in field measurements makes it possible to obtain a multi-Lagrangian dataset, implying a broader understanding of cloud dynamics through simultaneous observations. This approach allows better

estimates of turbulent characteristics such as kinetic energy, dispersion, and diffusion, as well as the small-scale variability of key physical quantities inside warm clouds and other environments [39].

Additionally, the availability of multiple Lagrangian trajectories is ideal for Lagrangian statistical analysis, particularly in correlation studies. These are fundamental for Reynolds-Averaged Navier–Stokes (RANS) models and Large Eddy Simulations (LES), since they rely on statistical closures, such as the parameterization of velocity correlations, to approximate turbulent motion.

3.1 Operating Environment and System Architecture

The radiosonde was originally conceived to be deployed inside atmospheric clouds, but its use has naturally been extended to the study of the atmospheric boundary layer and its turbulent characteristics. Beyond these fields, its potential applications include oceanic research to analyze small-scale fluctuations, pollution monitoring, and solar radiation measurements through the integration of additional sensors, making it a versatile tool for environmental studies.

The greatest challenge, however, lies in designing radiosondes specifically for warm clouds, as this environment is the one that imposes the most restrictive requirements on instrumentation. These clouds, originating from thermoconvective processes (as discussed in Chapter 2), are typical of the spring and summer months, forming over alpine and hilly terrain as well as over vast plains [40].

In such clouds, eddies range from scales of about one meter, with characteristic frequencies of 0.5–1 Hz and kinetic energies of 10^{-3}–10^{-2} m^2/s^2, up to structures of the order of kilometers, whose frequencies fall to the order of 10^{-4} Hz [40].

Temperature conditions rarely exceed the range 0–30 °C, while pressures extend between 400 and 1100 mbar, corresponding to altitudes from the surface to the lower troposphere. Looking at such values, fortunately most sensors cover a much broader range, so this does not present a major limitation. On the other hand, however, humidity represents a greater challenge, because standard sensors cover the 0% to 100% range but cannot directly measure supersaturation, crucial for microphysical processes. A possible alternative approach, which will be explored in future developments, is to infer it indirectly by combining multiple sensor readings.

Finally, concerning position measurements, the ideal scenario would be to have an uncertainty comparable to the size of the radiosonde itself. At the state of the art, GPS technology is limited to accuracies of the order of a few meters, but this level of precision can be considered for now more than sufficient for our purposes.

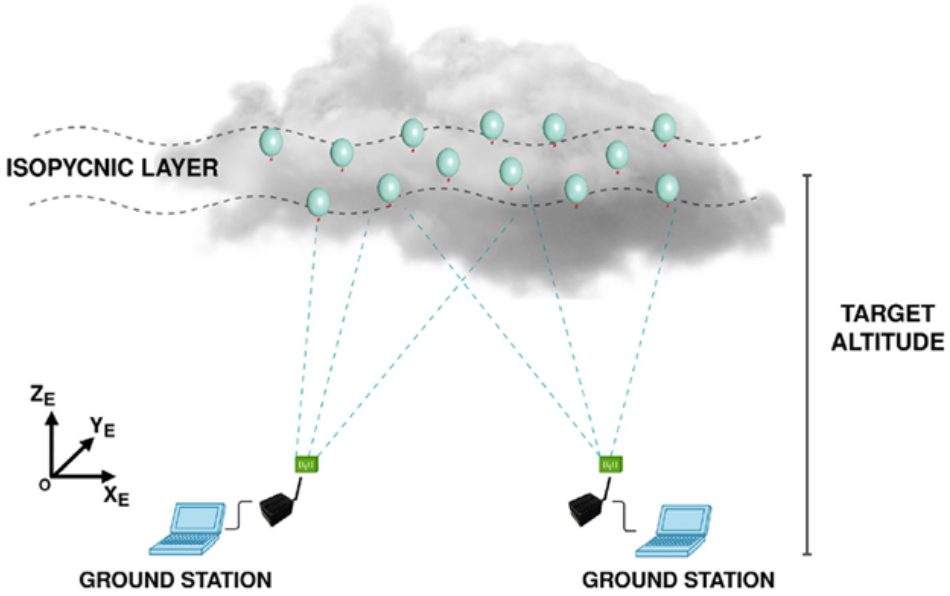

Figure 3.1: Schematic of an in-field setup, with a radiosonde cluster and ground receiver stations. The cluster floats within an isopycnic layer at the configured target altitude, and the launch location defines the origin of the experiment frame X_E, Y_E, Z_E [39].

The whole system, schematized in Fig. 3.1, can be considered as a Wireless Sensor Network (WSN) [39]. Each radiosonde unit, suspended from a bio-balloon, acquires physical quantities with solid-state sensors and transmits data to the ground stations using LoRa/LoRaWAN technology, wich is a low-power, long-range communication system operating on license-free ISM (Industrial, Scientific, and Medical) bands. The ground receiver stations then have the task to store and forward the data to the post-processing system, which will instead handle database management, filtering operations, and visualization of the dataset. To ensure redundancy and minimize data loss, a network of multiple stations that can receive the same data can be adopted.

3.2 Radiosonde Design and Technical Specifications

It is important to clarify from the outset that the term radiosonde refers essentially to two main components: the radioprobe electronic board and the biodegradable aerostatic balloon. Although the initial design considered placing the electronic instrumentation inside the biodegradable balloon, experimental tests aimed at verifying the accuracy of the measurements led to the decision to keep the PCB outside the balloon. Furthermore, at this stage, the use of a casing for PCB has been avoided to reduce unnecessary weight.

Figure 3.2: Cluster of radiosondes connected to Mater–Bi balloons, ready for launch.

While Chapter 4 will discuss the biodegradable balloon in detail, the focus here is on the electronic board. Figure 3.3(a) displays the present prototype (in red) together with the second, miniaturized version (green), whereas Figure 3.3(b) shows the current prototype connected with its battery.

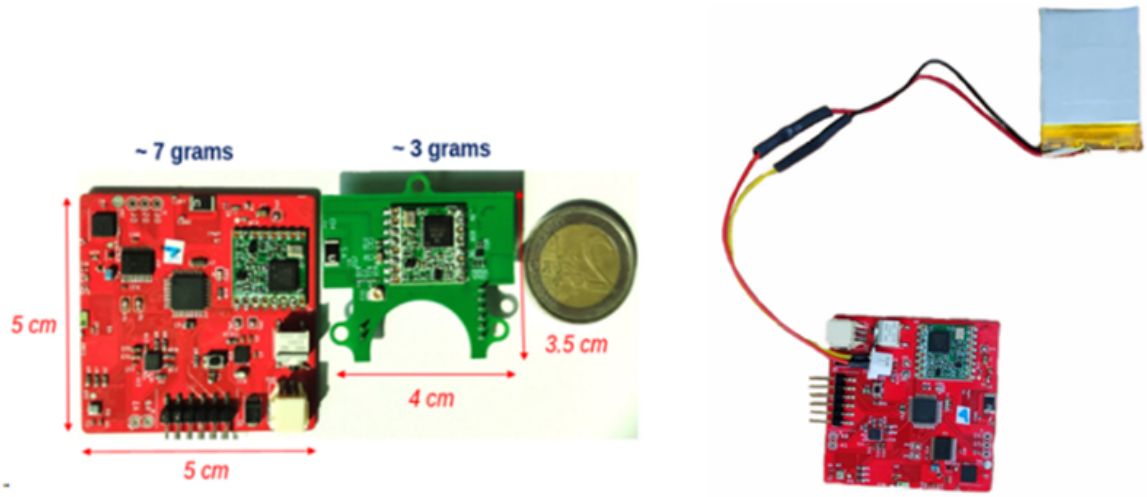

(a) (b)

Figure 3.3: (a) Comparison between the first prototype (red), a prospective two-layer design (green), and a two-euro coin. (b) Current version of the radioprobe with battery.

The same electronic system configuration has been used for both version. As illustrated in Figure 3.4, the board can be divided into five functional units: a data processing and control unit (1), a radiocommunication system (2), a set of environmental sensors (3), a positioning and tracking module (4), and finally the power supply unit (5)[40].

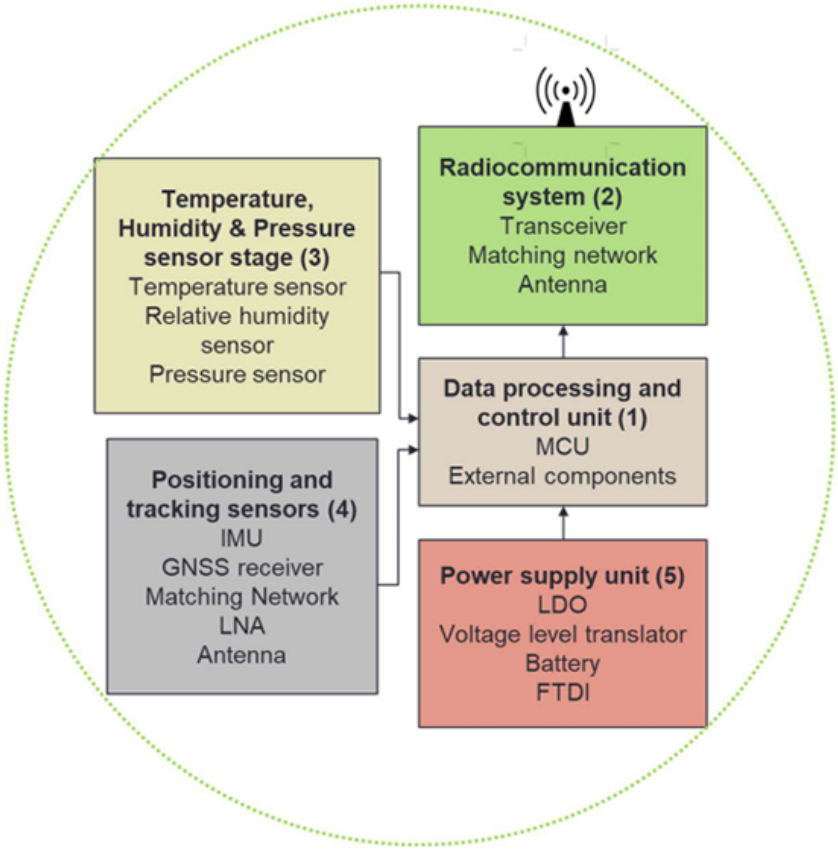

Figure 3.4: Block diagram of the radioprobe PCB showing the interconnections between modules [40].

The **processing unit** is implemented with the ATmega328 8-bit CMOS microcontroller (Microchip), which manages sensor acquisition, basic preprocessing, and transmission tasks. Compact and energy-efficient, it operates with supply voltages between 1.8–5.5 V and withstands a temperature range of -40°C to $+85$°C. Its power consumption is particularly low: 0.2 mA in active mode, 0.1 μA in power-down, and 0.75 μA in power-save mode. It measures $9 \times 9 \times 1$ mm and weighs only 70 mg.

The **radio system** uses the RFM95 transceiver (HopeRF) configured for LoRa (Long Range) communication. Although often implemented under the LoRaWAN specification, here it is set as a private point-to-point (P2P) network. The device works between 1.8–3.7 V and within -20°C to $+70$°C. Current consumption varies from 20 mA ($+7$ dBm) to 120 mA ($+20$ dBm), depending on the output power, and it drops to 1.5 μA and 0.2 μA if used in idle and sleep modes, respectively. Two miniaturized ceramic antennas, of quarter-wave type, are mounted on the PCB: the first one uses frequencies at 868 MHz to transmit data to the ground station, while the second one, tuned at 1575 MHz, receives GNSS signals. Both are impedance-matched with L-type networks and shielded to minimize interference.

As an **environmental sensor** for pressure, temperature and humidity, the BME280 (Bosch) was selected, which combines the detection of these three parameters in a single compact device ($2.5 \times 2.5 \times 0.93$ mm). It works within 1.2–3.6 V and covers the full atmospheric range: -40°C to $+85$°C for temperature (accuracy ± 1°C), 300–1100 hPa for pressure (± 1 hPa), and 0–100% RH for humidity (± 3%).

For **positioning and tracking** function, the system consists of two components.

The LSM9DS1 IMU (STMicroelectronics) provides acceleration, angular velocity, and magnetic field data, operating at 1.9–3.6 V and −40°C to +85°C, and measures 3.5 × 3 × 1 mm. The ZOE-M8B GNSS receiver (u-blox) supports multiple GNSS constellations, measures 4.5 × 4.5 × 1 mm and requires 1.71–1.89 V, allowing a 2.5 m accuracy in continuous mode, while 3.5–4 m in power-saving configurations.

Power supply is a critical aspect of the design: as seen throughout the component selection, minimizing power consumption is essential, since increasing energy storage inevitably adds weight. Thus, a careful balance must be done between operational autonomy and overall system mass. Current flights employ a lithium metal oxide (LMO) battery with the following specifications: capacity 400–500 mAh, weight 12–13 g, volume 4 cm^3, and operating temperature range from −55°C to +85°C. Voltage regulation is managed by an onboard low-dropout (LDO) regulator supplying the 1.8 V and 3.3 V lines. A USB interface is also available, mainly for code uploading.

Table 3.1 reports the main specifications of the adopted modules.

Device code	Property	Sample rate	Range
BME280	Humidity	1 Hz	0 % — 100 %
BME280	Pressure	1 Hz	300 — 1100 hPa
BME280	Temperature	1 Hz	-40°C — +85°C
LSM9DS1	Acceleration	10 — 952 Hz	± 16 g
LSM9DS1	Angular velocity	14.9 — 952 Hz	± 2000 dps
LSM9DS1	Magnetic field	0.625 — 80 Hz	± 16 Gauss
ZOE-M8B	Longitude	4 — 10 Hz	± 180°
ZOE-M8B	Latitude	4 — 10 Hz	± 90°
ZOE-M8B	Altitude	4 — 10 Hz	0 — 50 km
ZOE-M8B	Velocity	4 — 10 Hz	± 500 m/s

Table 3.1: Specifications of the main sensors and modules [41, 42, 43].

3.3 Validation and Testing of the First Prototype

The first operative launch involving a cluster of free-floating radiosondes took place at the Astronomical Observatory of the Aosta Valley (OAVdA), in Saint-Barthélemy, on November 3, 2022. To obtain this result, before (but also after) several tests were carried out for the validation of the radiosondes, starting from the single components up to a complete multi-sonde system. Therefore, the aim of this section will be to give a short review of the most important steps that made possible to reach the current design of the electronic system.

3.3.1 Validation of Temperature, Humidity, and Position Tracking

The first stage of the validation campaign focused on assessing the accuracy of the sensors used to measure pressure, temperature, and humidity, as well as on verifying the correct

functioning of the positioning system. The goal was to confirm that the integrated units performed according to specifications before moving on to more complex in-field launches.

To ensure the accuracy and reliability of the PHT unit (BOSCH BME280), a Kambic KK190 CHLT climatic chamber was used, provided by the Applied Thermodynamics Laboratory of INRiM (Italian National Metrology Institute). This instrument is designed for high-precision meteorological and climate metrology, and can span a wide thermal interval (–40 °C to +180 °C) with controlled humidity from 10 % to 98 %. For reference, four Pt100 platinum resistance thermometers, connected to a FLUKE 1594A Super Thermometer, were employed for temperature comparison, while a Delta Ohm probe, also calibrated at INRiM, was used for reference humidity readings.

The experimental procedure consisted in carrying out stepwise changes of one of the two environmental parameters, keeping the other fixed. Figure 3.5 illustrates the temperature test procedure: after setting the humidity at 30%, the chamber was first stabilized at +24°C, then lowered to −5°C, and from that point incremental steps of 5°C or 10°C were followed, up to +10°C. Each step was maintained for about one hour to ensure thermal stabilization. The same procedure was used for humidity: the temperature was kept constant at 30°C while RH was adjusted to 10%, 20%, 40%, and 60%, each level maintained for approximately 30 minutes [40].

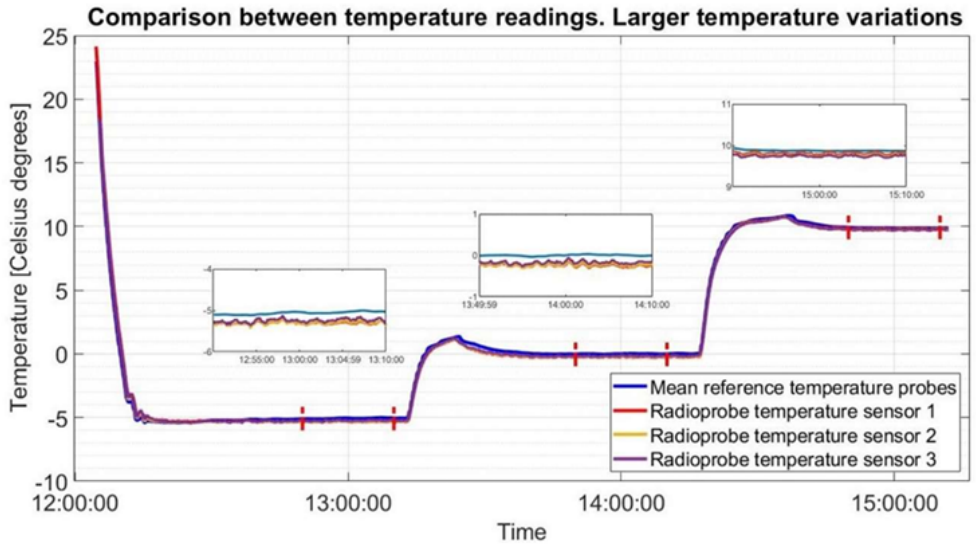

Figure 3.5: Thermal response of the BME280 sensor during climatic chamber tests. Each set-point was maintained for approximately one hour. Notably, some overshoots can be observed following abrupt temperature changes, which further justifies the need for a stabilization period at each step. [40]

Tables 3.2 and 3.3 report the statistical comparison between the radioprobe sensor readings and the reference instruments. Both temperature and relative humidity measurements were consistent with the manufacturer's declared specifications (±1 °C accuracy for temperature and ±3 % RH for humidity), and the only exceptions were observed in some relative humidity readings, which, however, may be attributable to the intrinsic uncertainty of the reference sensor itself [40].

		Sonde 1		Sonde 1		Sonde 1	
Temp. set point [°C]	Ref. sensor T [°C]	Mean [°C]	Mean error[°C]	Mean [°C]	Mean error[°C]	Mean [°C]	Mean error[°C]
-5	-5.063	-5.31	0.25	-5.30	0.24	-5.25	0.18
0	0.002	-0.25	0.25	-0.23	0.23	-0.17	0.18
10	9.878	9.82	0.065	9.75	0.13	9.74	0.13

Table 3.2: Comparison of radioprobe temperature measurements with INRiM reference thermometers. The "Set Point" indicates the programmed value of the climatic chamber. [40]

		Sonde 1		Sonde 1		Sonde 1	
Humidity set point [%RH]	Ref. sensor RH [%RH]	Mean [%RH]	Mean error[%RH]	Mean [%RH]	Mean error[%RH]	Mean [%RH]	Mean error[%RH]
10	10.50	13.12	2.62	14.74	4.24	14.16	3.66
20	19.75	19.85	0.09	21.35	1.60	21.09	1.34
40	37.68	35.31	2.37	35.64	2.04	36.06	1.62
60	59.70	56.13	3.57	54.53	5.17	55.69	4.01

Table 3.3: Comparison of radioprobe humidity measurements with INRiM reference sensors. The "Set Point" refers to the RH programmed in the climatic chamber. [40]

The positioning system was validated through a simple comparative test: walking along a certain path, the positional data recorded by the radioprobe were compared with those obtained from a smartphone, used as reference. The onboard IMU was configured to provide acceleration, angular velocity, and magnetic field data, while the GNSS module supplied temporal and geolocation updates [40]. It is noteworthy that in this experiment, since the two devices operated at different update rates (2 s for the probe versus 1 s for the smartphone), the IMU measurements were integrated between GNSS fixes, obtaining a more complete trajectory. This method at that time was used to make the two collected datasets comparable, but it can also be used in current experiments to reconstruct in a more detailed way the trajectories and velocities of a sonde.

As shown in Figure 3.6, the two trajectories closely agree, indicating that the positioning module is properly integrated into the radiosonde and is suitable for free-floating deployments.

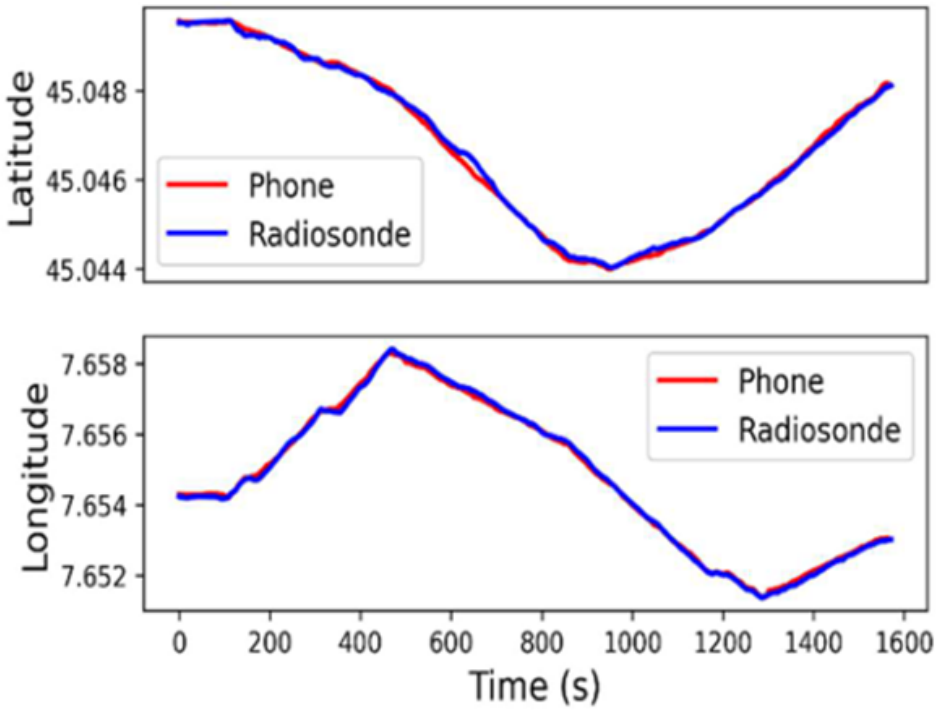

Figure 3.6: Comparison between the GNSS trajectory of the radiosonde and the GPS signal from a smartphone reference device. The test was conducted by walking along a predefined path. [40]

3.3.2 Dual launch experiments

Another type of experiment conducted for the validation of the radiosonde system concerns the dual launch experiments, during which temperature, humidity, pressure, and positioning data were compared with those of commercial Vaisala radiosondes. In total, three experiments of this type were conducted: the first two launches were carried out together with ARPA Piemonte at Levaldigi Airport (Cuneo, Italy) on October 28, 2020, and June 9, 2021; a third launch took place on July 6, 2023, at the Chilbolton Observatory (UK) during the Wessex Convection Campaign. A Vaisala RS41-SG at Levaldigi and an RS41-SGP at Chilbolton were used as reference instruments, respectively. During the first of these tests, interferences were observed, probably related to the direct connection of the radioprobe to the structure of the Vaisala sonde, but this issue was resolved in the second launch by mounting the radioprobe with an 80 cm offset [39].

One of the aspects investigated in the dual-sounding campaigns was the reliability of the data transmission between sondes and ground stations. Transmission from the radiosondes to the ground stations was evaluated in terms of the number of packets successfully received. In these experiments, communication relied on a LoRa peer-to-peer system, operating through private single-channel Dragino receivers. All transmission statistics reported below therefore refer to this setup.

During the June 9, 2021 Levaldigi test, continuous transmission was maintained for almost one hour, while the sondes reached altitudes close to 9 km and horizontal distances of about 13 km [39]. Figure 3.7 reports the average number of packets received as a function of time and altitude.

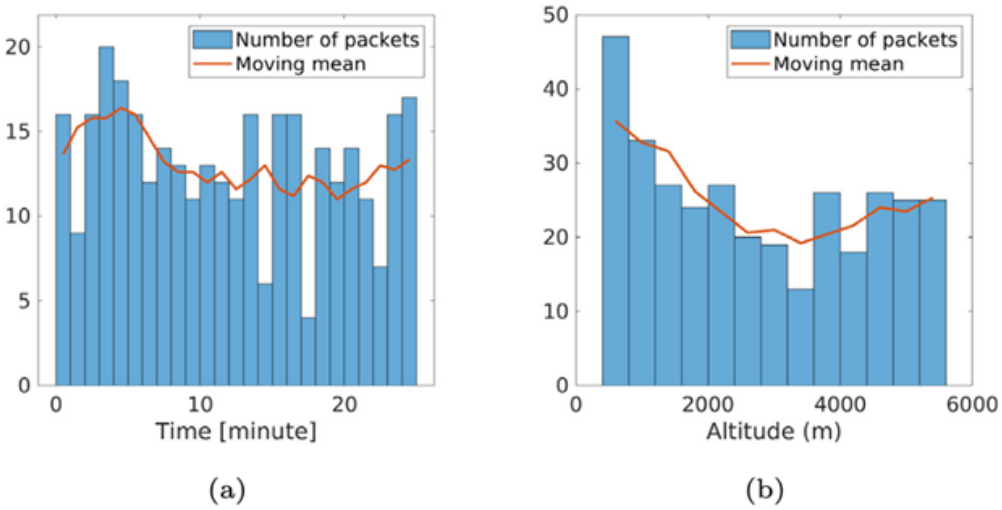

Figure 3.7: Long-range transmission test during the 2021 Levaldigi dual launch for packet size of the order of 100 bytes: (a) average packets per minute in the first 25 min; (b) average packets vs. altitude between 400 and 6000 m. Red lines show mean trends [39].

In general, packet loss is not negligible and can be caused by physical obstacles between the sonde and the ground station, or more naturally by the increase in distance between them. However, two countermeasures proved effective against data gaps: the first is, in the post-processing phase, to use interpolation to reconstruct missing samples; the second is the deployment of multiple receiving stations to increase redundancy. The latter was especially useful at Chilbolton, where adding a mobile station enabled data reception even beyond 34 km. Perhaps, it was precisely the advantages obtained from this latter method that anticipated the transition toward a distributed network of receivers. Such an evolution, in the form of LoRaWAN gateways integrated with the existing peer-to-peer infrastructure, was addressed in subsequent experimental campaigns and will be presented in Chapter 6.

The GNSS positioning was tested by direct comparison with the reference sondes. For the 2021 Levaldigi launch (Fig. 3.8), the agreement was generally good, and the estimated errors were: longitude RMSE 2.97×10^{-4} and MBE 2.95×10^{-5} degrees; latitude RMSE 3.7×10^{-4} and MBE -2.41×10^{-4} degrees; altitude RMSE 22.3 m and MBE 11.05 m [39].

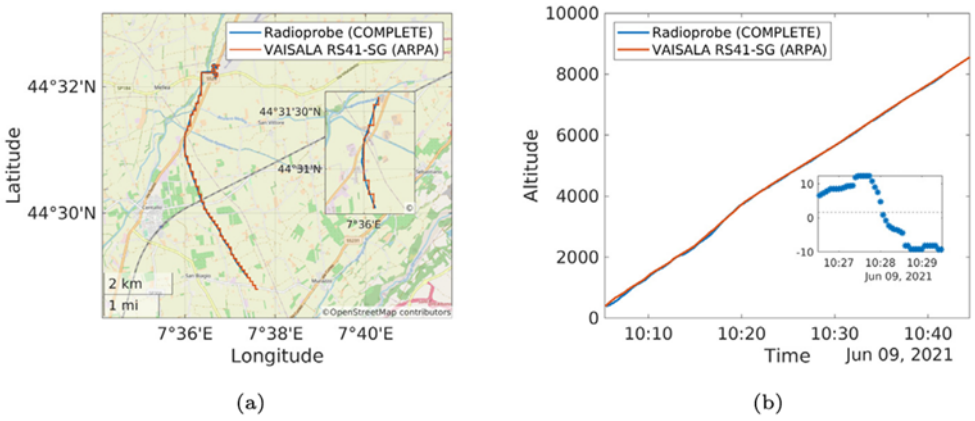

Figure 3.8: Levaldigi 2021 dual launch: comparison between our GNSS position (COMPLETE) and the reference RS41-SG. (a) Trajectories on map; (b) altitude vs. time with inset showing the altitude difference over a selected interval. Metrics reported in text. Adapted from [39].

The GNSS receiver also provides velocity in the North–East–Down frame, enabling horizontal wind estimation. As shown in Fig. 3.9(a), the wind speed measurement follows well the series of values obtained from the Vaisala, and the fluctuation spectrum in Fig. 3.9(b), computed via FFT (Fast Fourier Transform), displays a slope close to the $-5/3$ law, despite the non-ideal, anisotropic conditions typical of real atmospheric conditions.

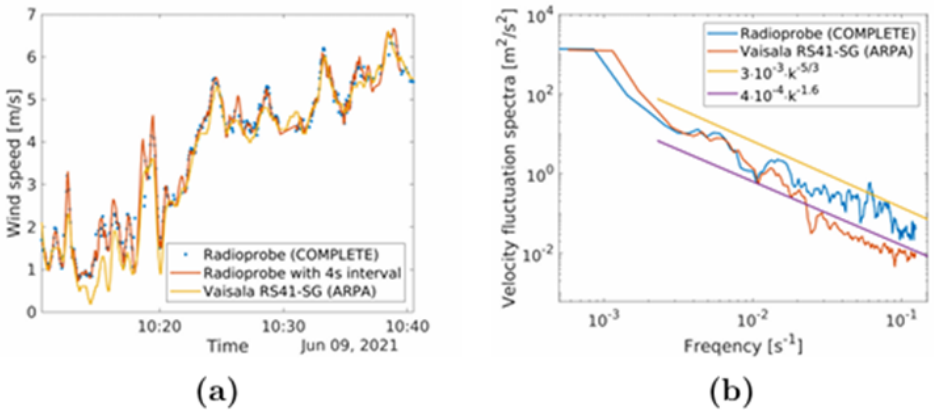

Figure 3.9: (a) Horizontal wind speed derived from GNSS velocity (COMPLETE) vs. RS41 during the 2021 Levaldigi launch; raw points (blue) and interpolated trend (red) are shown. (b) Power spectrum of velocity fluctuations from a 30 min time series. A 4 s resampling was used, corresponding to a frequency range from 5×10^{-4} s^{-1} to 0.25 s^{-1}, and a Nyquist frequency of 0.12 s^{-1}. The slope is compatible with a $-5/3$ trend. [39]

Regarding the evaluation of the PHT unit, Fig. 3.10 shows that the pressure profile is well-tracked by our sensor. Temperature readings (Fig. 3.11), instead, exhibited a constant bias (panels (a) and (d)) and, even after offset correction (panels (b) and (e)), a residual linear divergence with altitude became evident above the atmospheric boundary layer, which was about 4000 m during the 2021 Levaldigi test and around 3000 m in the 2023 Chilbolton launch [39]. This behavior can be attributed to solar-radiation effects, which are compensated in the reference sondes but not yet corrected in the present prototype.

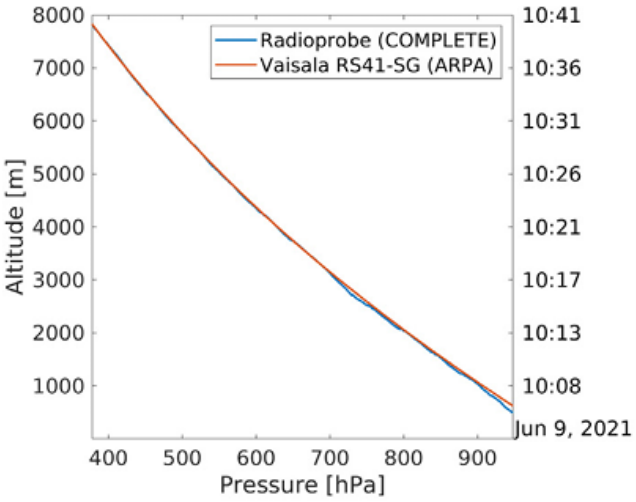

(a)

Figure 3.10: Pressure comparison between RS41-SG and the COMPLETE probe for the Levaldigi 2021 dual launch [39].

Chilbolton, UK. July 6th, 2023. COMPLETE probe was directly fastened to Vaisala RS-41 SGP probe with a scotch tape, **possible heating from RS41-SGP**.

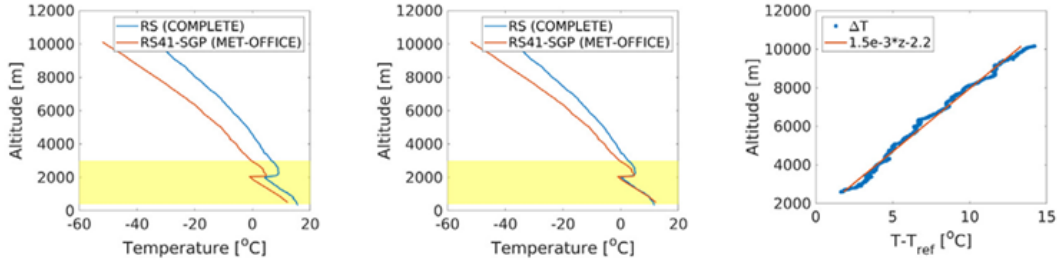

(a) (b) (c)

Levaldigi Airport, Cuneo, Italy. June 9th, 2021. COMPLETE probe attached with a 80-cm long wire to RS41-SG. **No heating from RS41-SG**.

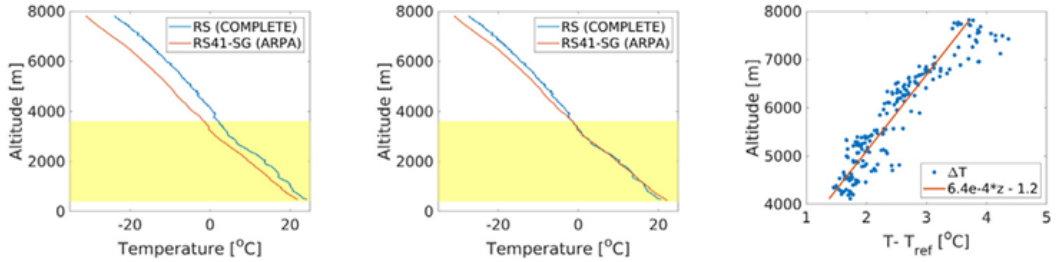

(d) (e) (f)

Figure 3.11: Temperature vs. altitude for dual-sounding experiments. The larger error at Chilbolton is plausibly linked to thermal interference from the adjacent sonde [39].

For humidity, the BME280 sensor showed a relatively slow dynamic response: high

relative humidity (65–85%) tended to be underestimated, whereas lower ranges (20–40%) were slightly overestimated (Fig. 3.12). Nevertheless, the overall trend and fluctuations were correctly tracked.

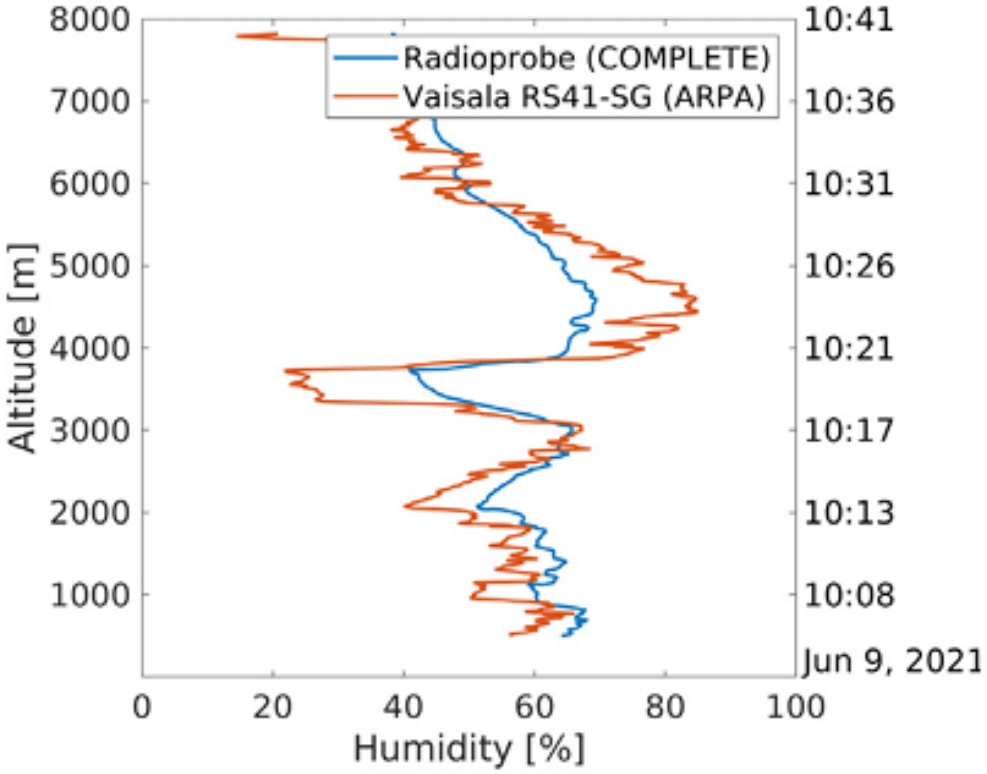

Figure 3.12: Relative Humidity comparison between our radioprobe (COMPLETE) and the Vaisala RS41-SG radiosonde of ARPA-Piemonte. The BME280 response shows bias at low/high RH ranges [39].

It must be considered that the PHT sensor measures humidity through a small vent hole, whose placement was carefully chosen during the PCB design phase and validated through several experiments [40]. However, ensuring proper airflow through this vent during flight remains a challenge, and insufficient air exchange may affect measurement accuracy (according to the sensor datasheet, it requires an airflow velocity of approximately 1 m/s [41]).

3.3.3 Cluster tests

Until now, we have exclusively focused on the validation of individual radiosonde systems. However, the ultimate goal is the deployment of large clusters of radiosondes for multi-Lagrangian measurements.

The first multi-sonde experiments took place in tethered mode, and were carried out at the INRIM campus on September 29, 2021, and at OAVdA, Saint-Barthélemy, on February 10, 2022. The process then advanced to free-floating cluster launches, with the first operational free-floating cluster deployed at OAVdA on November 3, 2022.

Subsequently, other cluster launches (each involving 10 radiosondes) took place at the Chilbolton Observatory: two in July 2023, within the framework of the Wessex Convection (WESCON) campaign, and two more in September 2024, all principally dedicated to

studying relative dispersion and Lagrangian correlations. Finally, a further cluster launch was carried out at the CISM center of Udine, Italy, in June 2024. In this section, however, we will focus exclusively on the two OAVdA campaigns, since they were the ones that marked the transition from component-level validation to multi-sonde free-flight operations.

The first of these experiments, carried out in tethered configuration, aimed at validating position and trajectory measurements by means of stereo vision analysis. Five tethered sondes were connected to two Dragino receivers, while at the same time two Sony HDV cameras tracked the motion of two marked sondes (red and black in Fig. 3.13). In this way, it was possible to calculate the distances between the radiosondes both from GNSS coordinates (longitude, latitude, altitude) and from stereo vision analysis, and the two methods were directly compared to assess positioning accuracy. The video sequences were captured with a pinhole camera model (with basic calibration) and then processed with the CSRT tracker from OpenCV, chosen for its ∼90% reliability in the presence of partial occlusions [44]. The estimated accuracy was within ±0.5 m horizontally and ±0.8 m vertically for distances of 20 m, and about ±4 m in depth over 100 m [39]. The comparison with GNSS (Fig. 3.14) showed good agreement: the mean absolute difference was 2.6 m in the initial minute and increased to about 5 m in the later part of the test due to strong winds. Even so, the deviations stayed within the nominal GNSS accuracy in Super-E mode, corresponding to ±4 m horizontally (and a vertical accuracy typically 1.7–2 times worse than the horizontal one) [39].

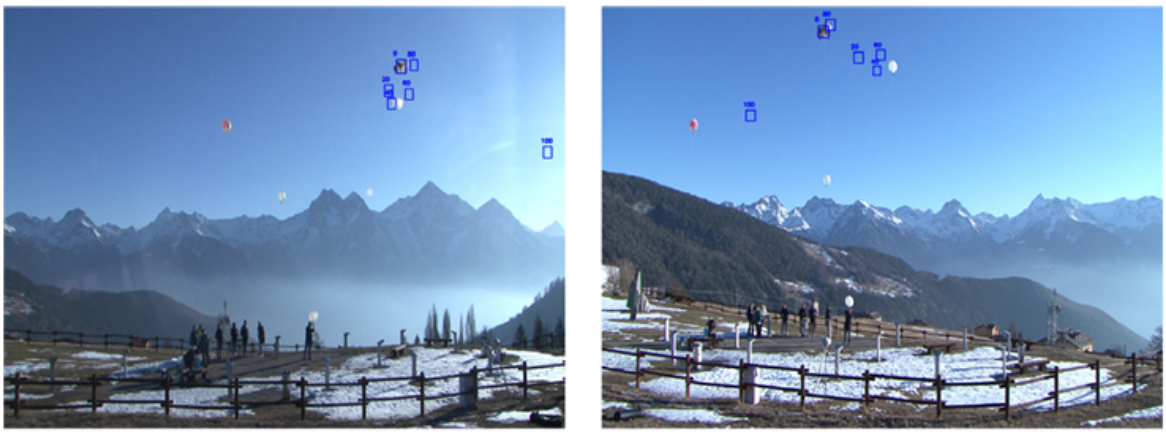

(a) (b)

Figure 3.13: Views from the two cameras during the tethered flight test on February 10, 2022. (a) Initial frame from Camera A; (b) Initial frame from Camera B. The blue rectangles highlight the subsequent positions of the black-balloon radiosonde, with the corresponding elapsed time displayed above each rectangle. [39]

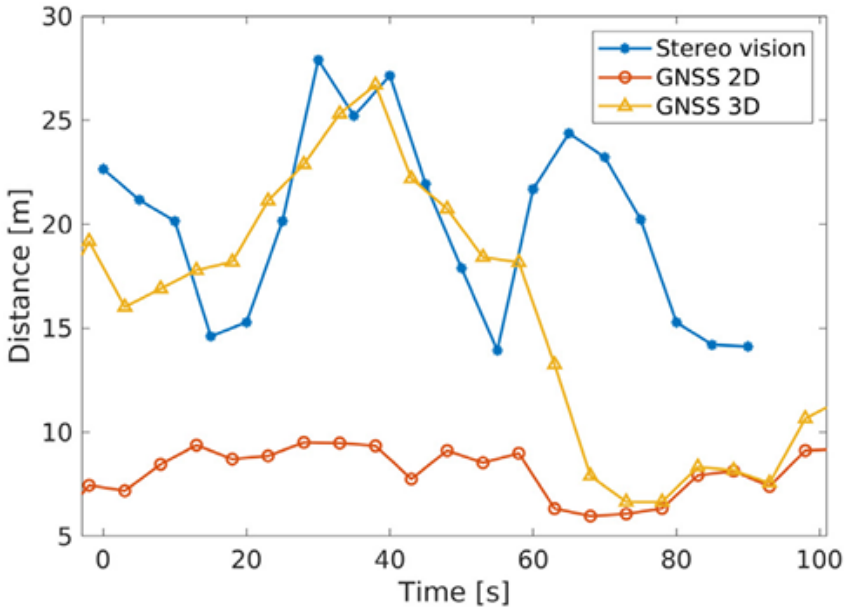

Figure 3.14: Relative distances between the black and red balloons obtained by GNSS (2D and 3D) and by stereo vision technique. [39]

The other experimental campaign in OAVdA, in November 2022, was the one that marked the first cluster free flight, releasing 10 sondes simultaneously. Before launch, they were fixed to a fence and calibrated using a portable Fluke DAQ 1586A multimeter connected to three PT100 thermometers, of which two unshielded and one shielded. This choice was made in order to distinguish the sensor bias from the effects of solar irradiance. As seen in Fig. 3.15, the measurements of the sondes were aligned with the two unshielded sensors (yellow and violet) used for calibration, while the shielded PT100 (green triangles), used to highlight the radiative effect, recorded temperatures on average 1.3°C lower [39].

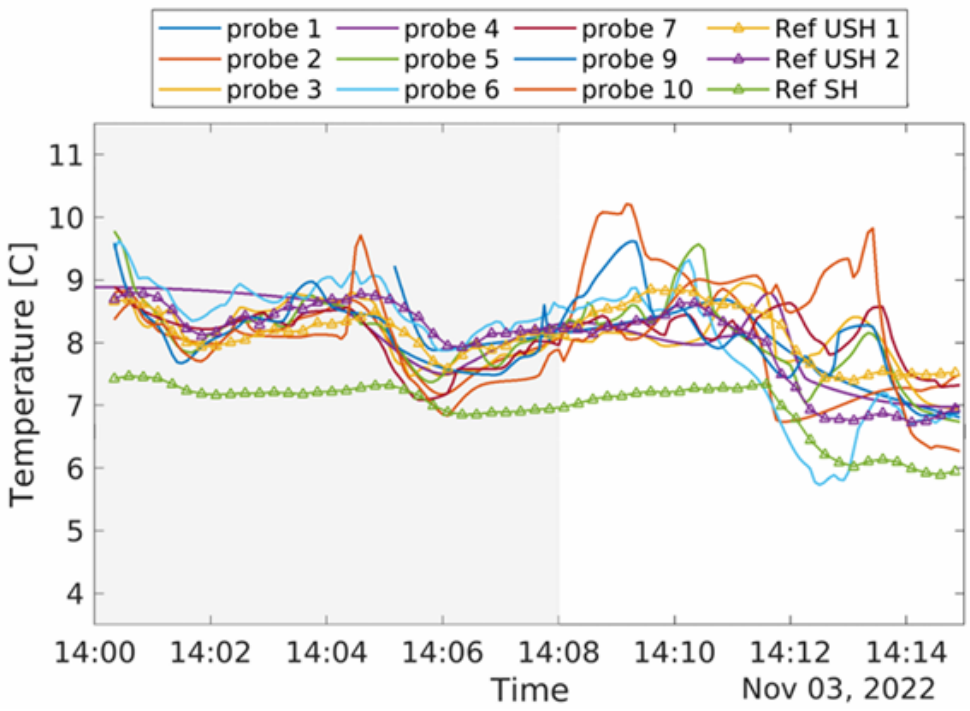

Figure 3.15: Comparison of temperature measurements from the radiosonde cluster and INRIM reference sensors. Initially, while the sondes were secured to the fence, their measurements were in good agreement with those from the unshielded references. After 14:08, however, some spikes were observed, mainly due to manual handling during preparation for free flight. [39]

After the pre-launch checks and calibration phase, the radiosondes were simultaneously released from the same initial position to free float in the skies of the Aosta Valley. In Fig. 3.16 their first 25 minutes of flight are shown. The probes covered a horizontal distance of up to 8300 m, ascending from an initial altitude of 1700 m and reaching a maximum of 3950 m [39]. Some probes lost data because of GNSS reception issues or mechanical stress, but most of them provided usable datasets. Panels (a) and (b) of Fig. 3.17 show the temperature and humidity measurements recorded over a 35-minute window (unfortunately, pressure data were invalid due to an error in the software library code). Several radiosondes stabilized at an equilibrium altitude and floated horizontally across the isopycnic layer, a behavior observed in Probes 2, 4, and 6 [39]. As an example, this horizontal floating is illustrated for Probe 6 in Panels (c) and (d) of Fig. 3.17, where the probe's altitude is plotted alongside the corresponding temperature and humidity measurements.

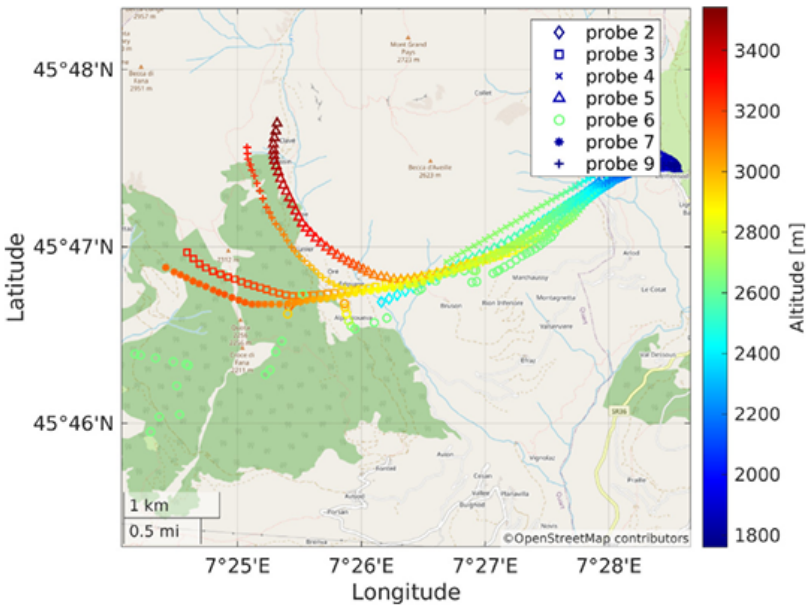

Figure 3.16: Trajectories of the radiosondes during the first 25 minutes of the free-flight phase (14:15–14:40), with marker colors representing the altitude reached along each path, starting from an initial elevation of 1700 m. [39]

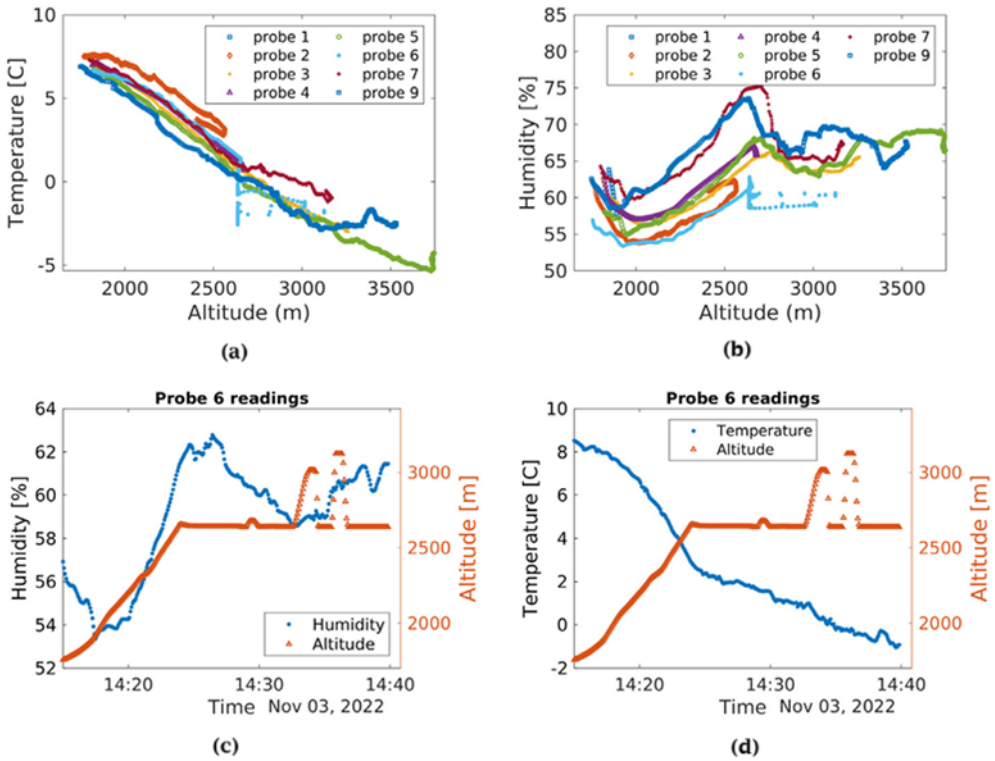

Figure 3.17: Temperature and humidity measurements. Panels (a) and (b) display the temperature and humidity readings from all radiosondes. Panels (c) and (d) show the temperature and humidity data from Probe 6, along with its corresponding altitude profile. [39]

Another goal of the free-flight experiment was to analyze turbulent dispersion of atmospheric flows. Power spectra of wind speed fluctuations, obtained from a 5-second resampling of GNSS velocities, are shown in Fig. 3.18. In these spectra it can be noted that the slopes follow the classical $-5/3$ law of the inertial subrange. In Fig. 3.19 the evolution of the distance-neighbor graph Q_L over time is shown, illustrating how the cluster spread as time passes: in the initial minutes, each probe had on average 2–3 neighbors within 100 m, while later this number drops close to one.

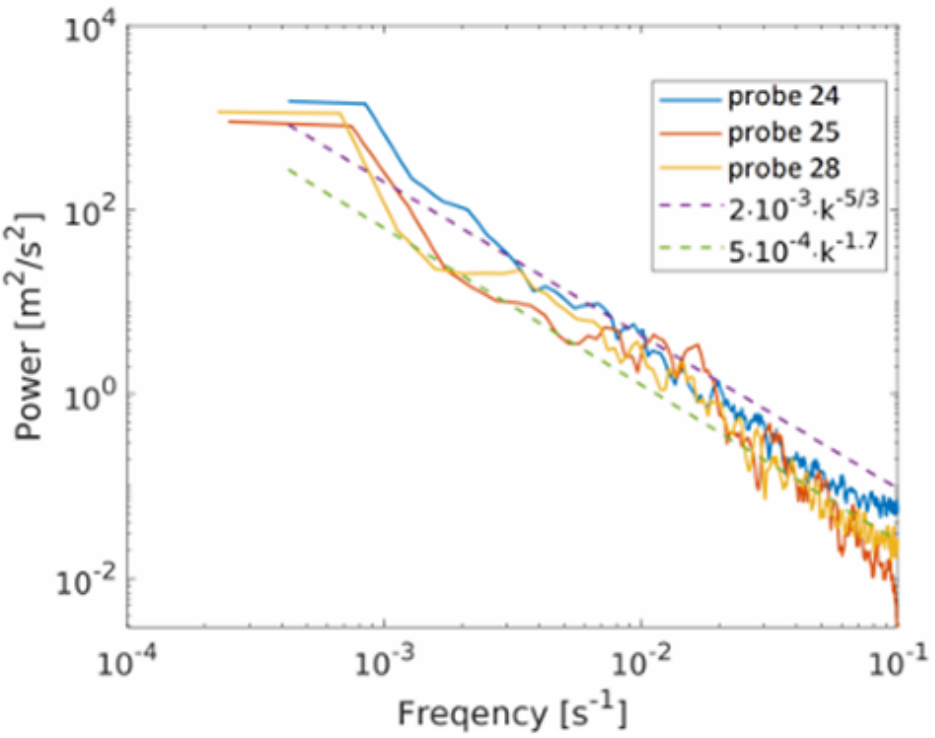

Figure 3.18: Power spectra of horizontal wind speed from three selected radiosondes during the OAVdA free flight. The original time series were resampled to a uniform 5 s dataset before applying FFT. Two trend lines are added for comparison. [39]

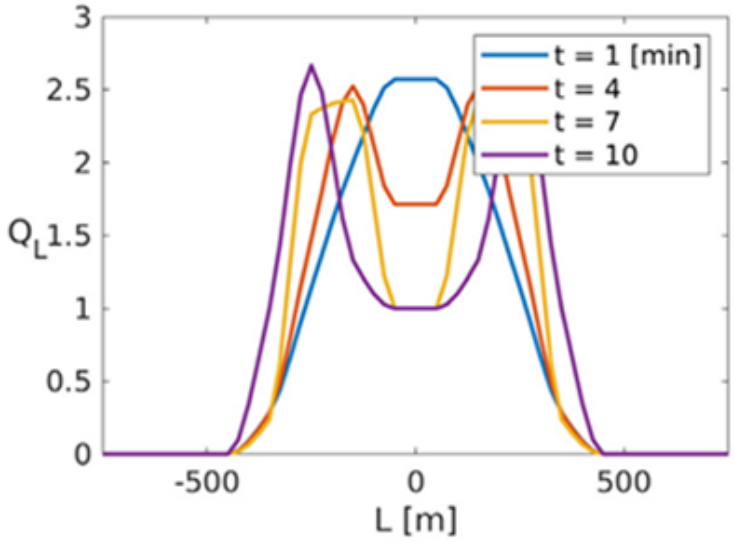

Figure 3.19: Evolution of the Q_L distance-neighbor graph for the radiosonde cluster (3D bins of $h = 100\,\mathrm{m}$). The progressive widening of the distribution reflects cluster dispersion. [39]

Chapter 4

Mater Bi Air Balloon

Even though at first the balloon might appear to be the simplest component to design, over time it has instead turned out to be one of the most delicate aspects to consider. In order to behave as a Lagrangian particle passively transported by turbulent motions, the balloon must possess characteristics that minimize the disturbances it could induce on the surrounding flow; the only way to achieve this, is by adopting a geometry as close to spherical as possible. Moreover, to float stably within an isopycnal layer at the target altitude, its volume must stay nearly constant throughout the entire duration of the experiment. Uncontrolled expansions during ascent could otherwise lead to unintended bursting or result in reaching altitudes different from those originally set. The balloon must also be capable of operating in challenging environments such as those found in saturated or supersaturated warm clouds, meeting specific requirements that will be discussed later in this chapter. In addition to these design constraints, another key requirement is the use of a biodegradable material and, as far as possible, one that is readily available on the market. Balloons represent a substantial portion of the radiosonde's total mass, and being able to build them with sustainable alternatives would significantly reduce their environmental impact. Taking all these factors into account, Mater-Bi®, a material developed by Novamont and commonly used in the production of biodegradable bags, was selected for our balloons. The following sections will describe the reasoning behind this choice, the sizing process of the balloons, and finally the issue of thermal sealing, which is addressed in this thesis through a proposed alternative: a manually operated thermal sealer that allows for pressure and temperature control.

4.1 Material Choice

First of all, it is necessary to clarify why Mater-Bi was chosen as the material for our balloons. At the beginning of the COMPLETE project, Basso et al. [45] analyzed several options in terms of materials, production processes, and polymer coatings. In collaboration with the Italian Institute of Technology (IIT, Genoa), two bio-based polymers such as Mater-Bi and PLA were compared with traditional materials used for weather balloons, such as Mylar and latex. In addition, combinations of surface coatings (e.g. carnauba wax, pine resin, and SiO_2 nanoparticles) were tested in order to improve the surface properties.

One of the most relevant properties to be tested was surface hydrophobicity, since the accumulation of droplets can significantly increase the overall weight of the radiosonde. Therefore, the contact angles on 5 μL water droplets were measured to quantify wettability, and the results showed that, while Mylar achieved the best result (95°), both PLA

and Mater-Bi reported lower values (below 90°), indicating their (relatively) high wettability. However, when coatings made of carnauba wax and SiO_2 nanoparticles were used, the contact angles of the green materials increased to values close to 140° (Fig. 4.1), very close to the superhydrophobic threshold of 150°.

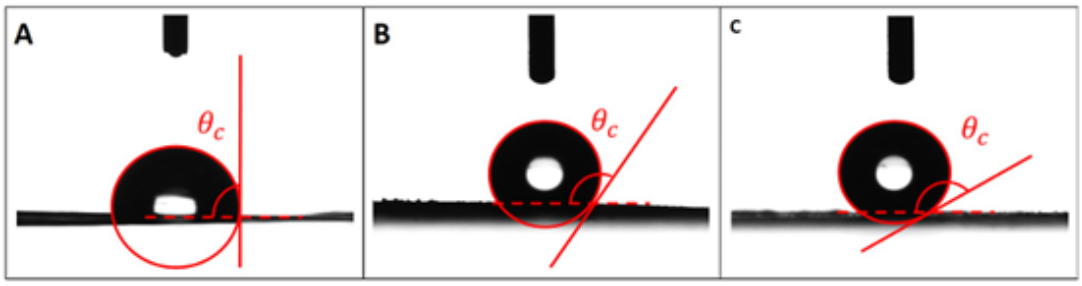

Figure 4.1: Increase in contact angle (and thus hydrophobicity) through the use of coatings. From left to right: (A) pristine Mater-Bi, (B) Mater-Bi coated with carnauba wax, and (C) Mater-Bi coated with carnauba wax + SiO_2 NPs. [45]

In addition to the surface properties, mechanical strength and deformability were also evaluated, factors of crucial importance given that the balloon must both maintain a constant volume and withstand slight overpressures during ascent. Mechanical characterization was conducted using an INSTRON 3365 uniaxial testing machine at a deformation rate of 1 mm/min, and the results are summarized in Table 4.1. PLA exhibited good mechanical strength and high rigidity, but, due to an elongation at break < 0.1 mm/mm, it could not tolerate even the small overpressures encountered during ascent. Mater-Bi, in contrast, displayed a Young's modulus between 100 and 200 MPa and elongation at break of about 3 mm/mm, values that make it sufficiently elastic to withstand them [45]. Moreover, the toughness of Mater-Bi ($\sim$30 J/m^3) was found to be comparable to that of Mylar, whereas PLA showed a much lower value ($\sim$6 J/m^3). The coatings also seem to slightly soften both green materials.

Material	Young's Modulus (MPa)	Tensile stress at yield (MPa)	Ultimate stress (MPa)	Elongation at break (mm/mm)	Energy (J/m^3)
Latex	4 ± 1	7 ± 1	27 ± 1	18 ± 0.3	125 ± 6
Mylar	1185 ± 33	30 ± 1	55 ± 3	0.8 ± 0.1	35 ± 4
Mater Bi	161 ± 13	8 ± 1	12 ± 1	3.2 ± 0.1	34 ± 2
Mater Bi + Cwax + Pine Resin	121 ± 10	6 ± 0.2	10 ± 1	3.1 ± 0.7	26 ± 6
Mater Bi + Cwax + SiO_2 NPs	108 ± 11	4 ± 1	7 ± 0.5	1.1 ± 0.1	8 ± 1
PLA	1578 ± 93	18 ± 2	24 ± 4	0.09 ± 0.05	4 ± 2
PLA + Cwax + Pine Resin	925 ± 22	15 ± 1	17 ± 1	0.07 ± 0.04	6 ± 3
PLA + Cwax + SiO_2 NPs	993 ± 112	14 ± 1	17 ± 1	0.06 ± 0.01	2 ± 1

Table 4.1: Characteristic average values of Young's modulus, tensile stress at yield, ultimate stress, elongation at break, and total absorbed energy. [45]

The last parameter of interest is the gas permeability of the material, since a loss of helium during the flight would affect lifting capacity and the maintenance of the set altitude. Balloons produced with different films were filled with helium and their weight was monitored for 3 hours. Pure Mater-Bi lost $0.02 \pm 0.005\%$ of its weight per minute, but when coatings were applied this value decreased to $0.01 \pm 0.005\%$, approaching that of Mylar ($0.008 \pm 0.005\%$) [45]. With such leakage rates, a descent of about 100 m over 3 hours can be expected, which is acceptable. PLA, on the other hand, showed higher losses (0.05–$0.06 \pm 0.04\%$), even after coating.

In conclusion, while hydrophobicity and helium permeability can be improved with coatings, Mater-Bi overall performed better than PLA, especially in terms of mechanical properties and gas retention. It should also be noted that the tests were conducted using Mater-Bi of 30 μm thickness, while in recent launches, a thickness of 20 μm (density 1.24 g/cm^3) was used, reducing the balloon mass by at least 50% (see the next chapter on sizing). Furthermore, Mater-Bi showed suitable characteristics even without coatings, even if it benefits from the improvements provided by them.

4.2 Balloon sizing

The sizing of the balloon is necessarily dependent on the weight of the payload, which in our case is composed of the radioprobe, the battery connected to it and the connections necessary to tie them to the balloon. Considering the first prototype of the probe and a 500mAh battery, the components of the total weight are reported in Table 4.2.

Part	**Mass [g]**
Radioprobe	6.5
Battery	12
Connections	1
Total	**19.5**

Table 4.2: Distribution of the total payload of the first prototype carried by the balloon.

Recalling Archimedes' principle, we can equalize the hydrostatic thrust to the total weight of the radiosonde, in order to define a condition of equilibrium necessary for neutral buoyancy at the desired altitude. The relationship can be expressed as:

$$M_t g = T = V_b g \left(\rho_{air} - \rho_{He}\right) \tag{4.1}$$

where M_t is the total mass of the radiosonde, g is gravitational acceleration, T is the lifting force generated by the balloon, and V_b is its volume. The term in parentheses represents the density difference between ambient air and the helium inside the balloon.

The total mass M_t can be considered as the sum of the balloon mass m_b and the payload mass m_p, which, as given in Table 4.2, is known and equals 19.5 g. Applying the ideal gas law, we can further express the density difference in terms of molar masses:

$$V_b = \frac{M_t}{\rho_{air} - \rho_{He}} = \frac{m_p + m_b}{\rho_{air}\left(1 - \frac{M_{He}}{M_{air}}\right)} \tag{4.2}$$

where $M_{He} = 4.003$ g/mol and $M_{air} = 28.96$ g/mol are the molar masses of helium and dry air, respectively. Approximating the balloon as a perfect sphere, its volume and mass can be written as:

$$V_b = \frac{4}{3}\pi R_b^3 \tag{4.3}$$

$$m_b = S_b t \rho_m = 4\pi R_b^2 t \rho_m \tag{4.4}$$

where S_b is the surface area of the sphere, t is the thickness of the Mater-Bi film, and ρ_m is its density. Substituting these expressions into Eq. 4.2 leads to a cubic equation in R_b. For given values $t = 23\,\mu$m, $\rho_m = 1.24$ g/cm^3 and a defined payload mass m_p, and using ρ_{air} from the ICAO standard atmosphere at the target altitude, the balloon radius R_b can then be obtained by solving this cubic equation numerically.

The figure below shows the relationship between balloon radius and attainable altitude for different payload weights. The purple line corresponds to the first prototype: a radius of 22 cm allows the probe to reach about 2600 m above sea level, while a radius of 23 cm increases the attainable altitude to roughly 3500 m.

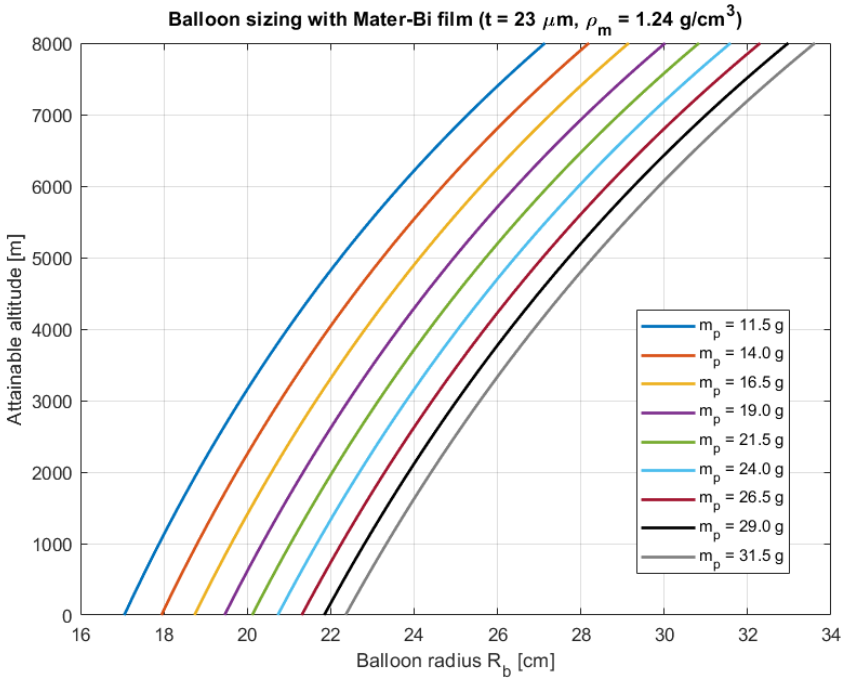

Figure 4.2: Plot that links balloon radius to the attainable altitude for different values of the payload m_p, considering Mater-Bi as the balloon material. [39]

Assuming a 22 cm radius, the balloon mass can be calculated as:

$$m_b = 4\pi R_b^2 t \rho_m \approx 17.5\,\text{g} \tag{4.5}$$

This brings the total weight of the radiosonde to approximately 37 g.

4.3 Balloon production

The most challenging aspect of the balloon design has undoubtedly been its physical production. Turning flat Mater-Bi sheets into a spherical shape that can hold helium, while keeping good mechanical strength and low gas leakage, can be a big challenge. Over time, several students have worked on the design and construction methods, converging in a method that is based on thermal sealing of four petal-shaped pieces (see Fig. 4.3). Each petal has a flap on one side to create the neck, which is where helium will be filled in, and a section on the other side for attaching a circular closing cap.

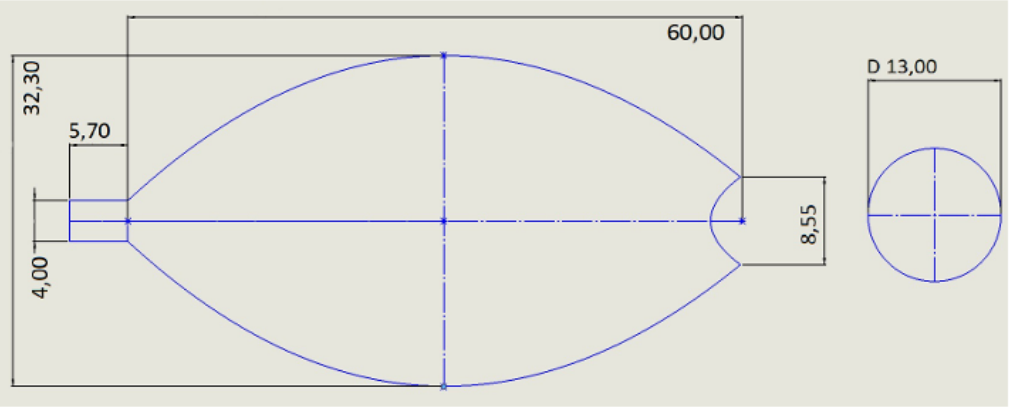

Figure 4.3: CAD model of the Mater-Bi components used for balloon fabrication. Here, the dimensions are designed to produce a balloon with a 40 cm diameter.

The Mater-Bi arrives in large rolls of bubble-blown film, double-layered and wound onto spools. Therefore, as a first step they must be cut and opened in order to have a single film from which it is then possible to cut out the petal shapes, adding about 1 cm to the edges to allow for overlapping during thermal welding.

Up to now, the welds have been carried out using a small plastic welder equipped with a heated wheel, typically used for sealing standard plastic films. The device includes a potentiometer to adjust the working temperature, but it is not originally designed for biodegradable materials such as Mater-Bi, which require significantly lower temperatures. In particular, the optimal welding temperature for ultra-thin overlapping Mater-Bi films was found to be around 60–70°C, well below the standard operating range of the welder.

Figure 4.4: Hand-operated wheel sealer with a temperature control knob.

To overcome this limitation, during the welding process a thin layer of Teflon can be placed between the heated wheel and the plastic film. In practice, its advantages are multiple: in addition to guaranteeing better thermal regulation, it prevents the wheel from sticking to the film and reduces mechanical stress on the material, which could otherwise lead to micro-cracks. Such damage may not be immediately visible and is not always repairable.

Each weld must be visually inspected and, if necessary, reinforced by repeating the welding process. Once all petals are joined, the balloon is turned inside out (so that the welded flaps remain on the inside) and is then ready for inflation. For closure, the neck can be tied with the same thread that will then be used to connect the PCB before launch.

Chapter 5

The project

The development of the Mater-Bi balloon during the last years highlighted the critical limitations of manual thermal welding. The hot-wheel sealer, although extensively used, proved imprecise, unreliable, and inefficient: even a 1 mm variation in radius could cause significant differences in flight altitude, micro-cracks often led to helium leaks, and the manual process required several hours per balloon. These issues motivated the search for new welding methods.

A first approach was to investigate possible collaborations with external companies, and in 2025 a partnership was established with Grabo Srl, one of the global leaders in foil balloon manufacturing. This collaboration led to the first experimental production of Mater-Bi balloons, in the form of circular sheets sealed using well-calibrated industrial machines (Fig. 5.1). Even though the path to achieving spherical shapes may still be long, these balloons showed adequate helium retention and turned the idea of industrial-scale production into a concrete option.

Figure 5.1: First production test of Mater-Bi balloons using two circular sheets, developed in collaboration with Grabo Srl.

In parallel, alternative technologies were considered. On paper, ultrasonic welding and laser welding both appeared promising for thin thermoplastic films, and several studies in the literature reported their successful application to biodegradable polymers such as

PLA and PHB blends composites [46, 47, 48]. However, these methods remain too costly and complex for our current context. In the future, dedicated tests could be carried out at the J-Tech interdepartmental center of Politecnico di Torino, where a six-axis robotic system for laser welding is available, potentially adaptable to Mater-Bi if settled at low power levels.

Attention was also given to more accessible options. A first idea concerned the use of adhesives, but it was discarded since hot-melt types are incompatible with the thermal stability of Mater-Bi, while cold-applied glues (e.g., water-based or natural resins) lack sufficient mechanical performance, and in any case they would add non-negligible weight. Heated plates and hot-air systems were also considered, but in the end they were not regarded as suitable for thin biodegradable films.

After this evaluations, the only viable option that remained was the hot-wheel technique. The project therefore focused on improving and optimizing this method, leading to the design of a double-wheel thermal sealer wich will be described in the following sections.

5.1 Design of the Double-Wheel Thermal Sealer

Before developing a new thermal sealer, it was necessary to identify the main factors that can influence the quality of a thermal weld. In particular, three parameters were considered:

- The temperature of the wheel that comes into contact with the Mater-Bi films;
- The pressure applied by the system on the material;
- The rotation speed of the heated wheel, which determines the time during which the material remains in contact with the hot surface.

The starting point was the existing hot-wheel sealer, chosen not only for the familiarity brought by its use in past years, but also for the undeniable advantage of already possessing an integrated temperature control system. The concept was to add an external system around the original thermal sealer to provide pressure and feed-rate control; the sealer remains untouched, enabling easy installation or removal of the additional parts and keeping it available as a backup. From the outset, the design moved toward a benchtop configuration, abandoning the portable form of the original tool. A spring-based mechanical solution was selected for the compression system, considered simpler and more precise than a lead-screw mechanism.

To obtain indicative measurements of the operating ranges of the three welding parameters, preliminary manual trials were conducted. The device alone weighs about 400 g, but including cables and the potentiometer, it almost reaches 700 g. According to the manufacturer's specifications, the wheel temperature can be adjusted up to 200 °C, although the accuracy of this control is not specified. During these preliminary tests, performed at the lowest temperatures and with a Teflon sheet used as protection, the force required to achieve satisfactory welds was found to be in the range of 1.2–2 kg. As expected, the result was also influenced by the feed rate of the wheel, since a slower progression increases the heat transferred to the films.

A key design question concerned whether to keep the wheel fixed and move the sheet, or vice versa. Fixing the sheet and guiding the wheel along predefined paths (e.g., the

petal contours or the upper cap) would be easier than manually handling thin Mater-Bi films ($\sim$23 μm). However, a mobile-wheel system would introduce excessive mechanical complexity and limit adaptability to future geometries. For this reason, it was decided to keep the heated wheel fixed while the two overlapping sheets were driven forward. To prevent slippage between the films, a second unheated wheel was introduced instead of a flat sliding surface, ensuring that welding occurred precisely at the nip point between the two rollers. An auxiliary platform could also be added to keep the sheets aligned with the sealing point.

5.1.1 CAD Modeling and Prototype Iteration

At this stage, several design concepts were considered, particularly regarding the spring-based compression system. After initial sketches on paper, the solutions were modeled in SolidWorks. The design process was iterative, with two preliminary versions developed before reaching the final prototype. The following section briefly retraces these steps.

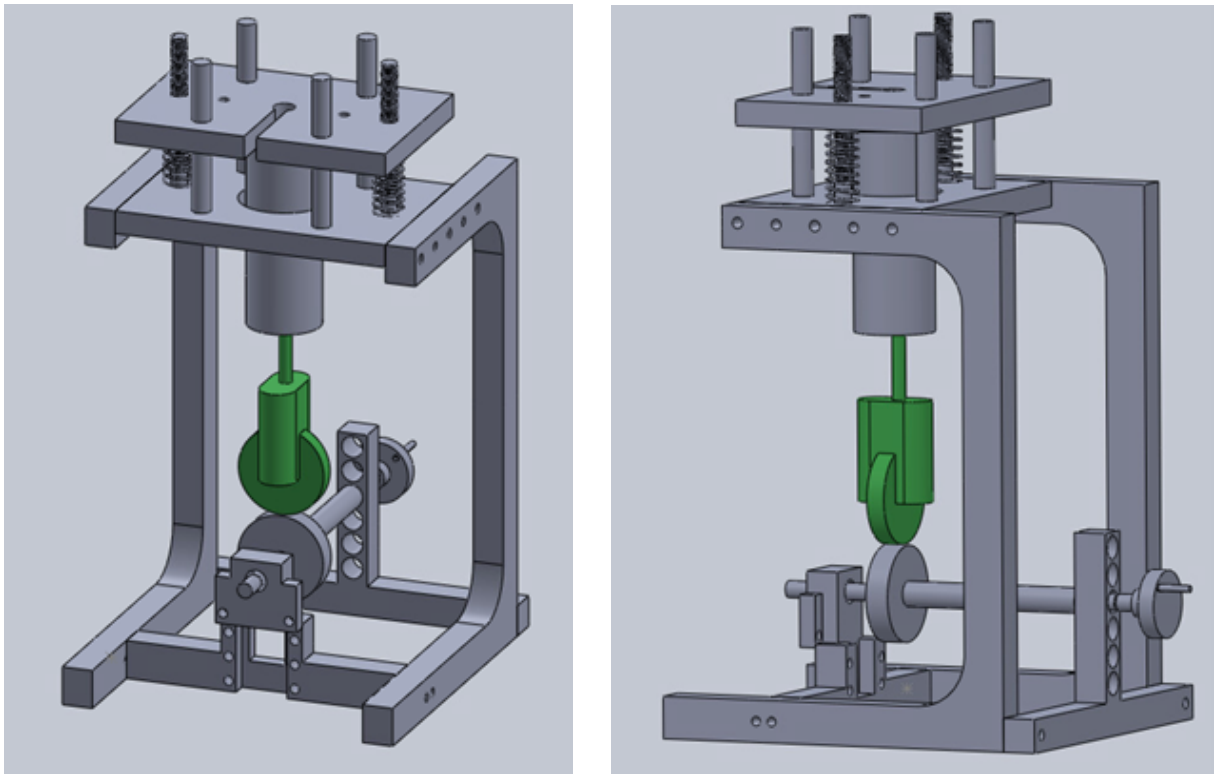

(a) (b)

Figure 5.2: CAD model of the first prototype version. The compression system with two springs, four guide pins, fixed and movable plates, and threaded rods is shown. The shaft height can be adjusted. The original hot-wheel sealer is highlighted in green.

Figure 5.2 shows the CAD model of the first version of the prototype. The compression system consisted of two springs positioned between two plates: a fixed lower plate anchored to the vertical supports, and a movable upper plate. The hot-wheel sealer (shown in green) was held in position by a metallic handle attached to the movable plate. Four guide pins and two threaded rods were fixed to the lower plate and passed through corresponding holes in the upper plate. By tightening wing nuts (not shown in the figure)

on the threaded rods, the upper plate could be progressively lowered toward the lower one, bringing the two rollers (upper and lower) into contact. Pressure on the overlapping films was then adjusted by further tightening the nuts.

The shaft of the lower roller could be inserted at different height positions. Since the combined weight of the movable plate, the handle, and the sealer compressed the springs to different extents depending on their stiffness, the vertical position of the heated wheel was not known a priori but only estimated within a certain range. For this reason, the limiting heights were evaluated according to the mechanical properties of commercially available springs. The lower roller was connected to a knob with a locking pin, which allowed manual rotation. In this way, the operator could control the feed rate of the sheets with one hand while guiding their direction with the other, in a manner similar to a sewing machine.

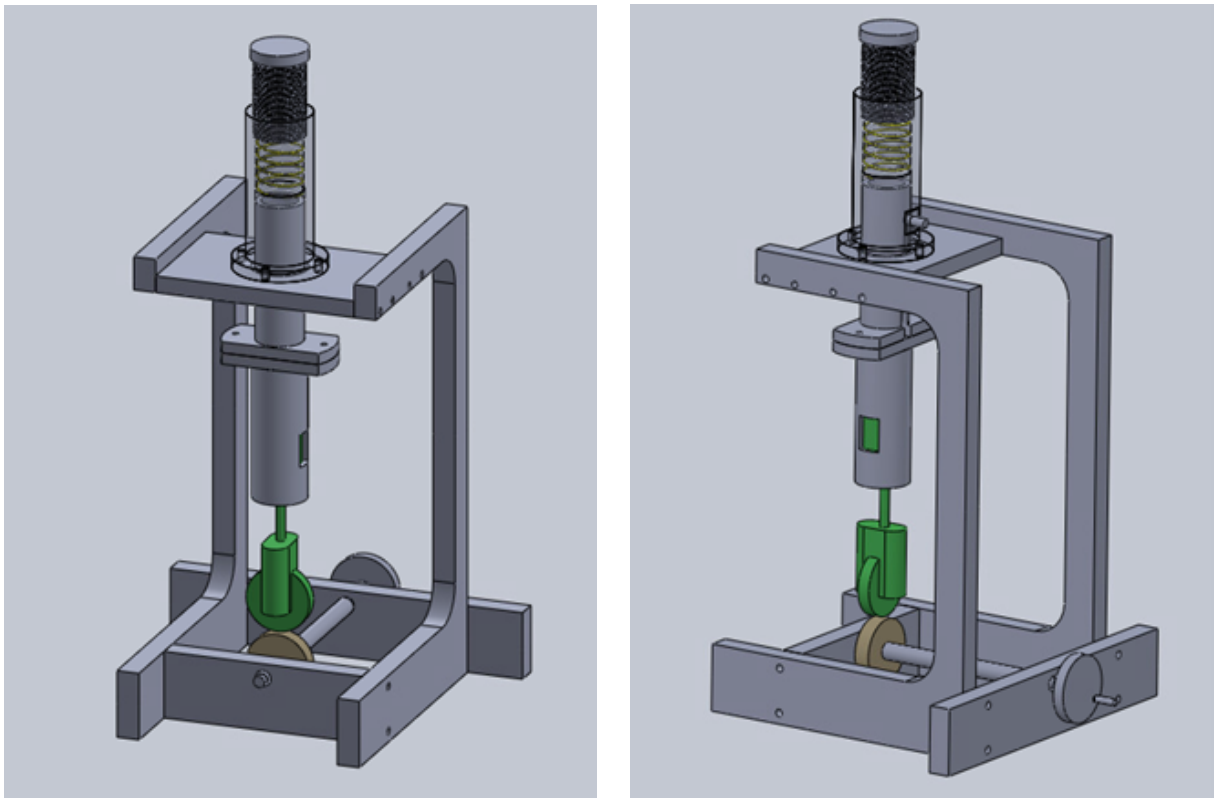

(a) (b)

Figure 5.3: CAD model of the second prototype version. Pressure control is simplified with a single spring, a threaded knob, and a cylindrical housing for the spring (highlighted in yellow). In this version, the lower roller shaft has only one fixed slot.

Figure 5.3 illustrates the second prototype version. The main difference concerned pressure control: in this version, the heated roller was no longer suspended on springs between two plates but instead pressed by a single spring whose only function was to increase the force applied on the counter-roller. Pressure adjustment was achieved with a threaded knob inside a cylindrical housing (transparent in the figure for clarity). A spring, inserted in this housing (indicated by the arrow), pushed against a cylinder attached to the original heated roller.

This solution was preferred to the previous one because it was expected to ensure greater simplicity in construction (fewer components and less strict dimensional toler-

ances) and greater ease of operation, since regulating a single spring is more practical than manually handling a system of multiple springs. In addition, for the lower roller shaft it was decided to adopt a single fixed position, with simple perforated plates used as bearing slots, further simplifying the prototype.

Finally, based on this second version, a further simplification was introduced: the sealer was no longer fixed to the machine by clamping its cylindrical handle, but instead by gripping the green protective plate of the tool (see Fig. 4.4). This modification, together with other optimizations, led to the development of the third and final version of the thermal sealer (Fig. 5.4).

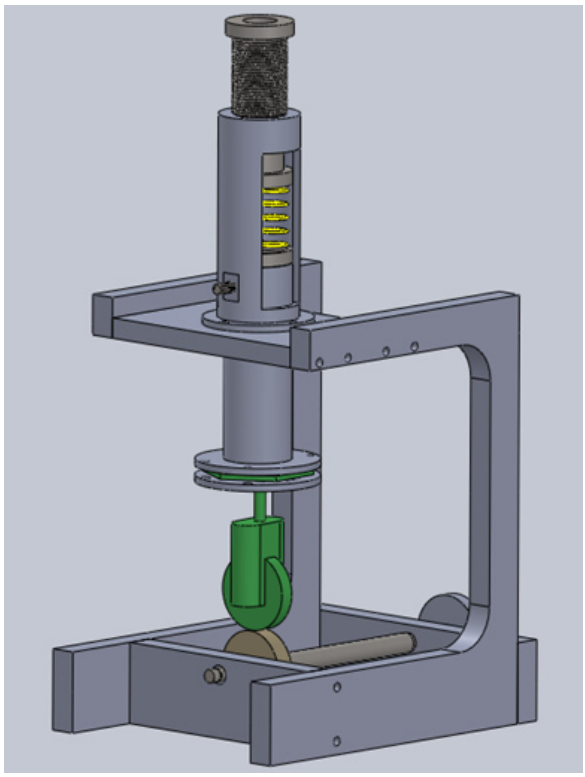

(a)

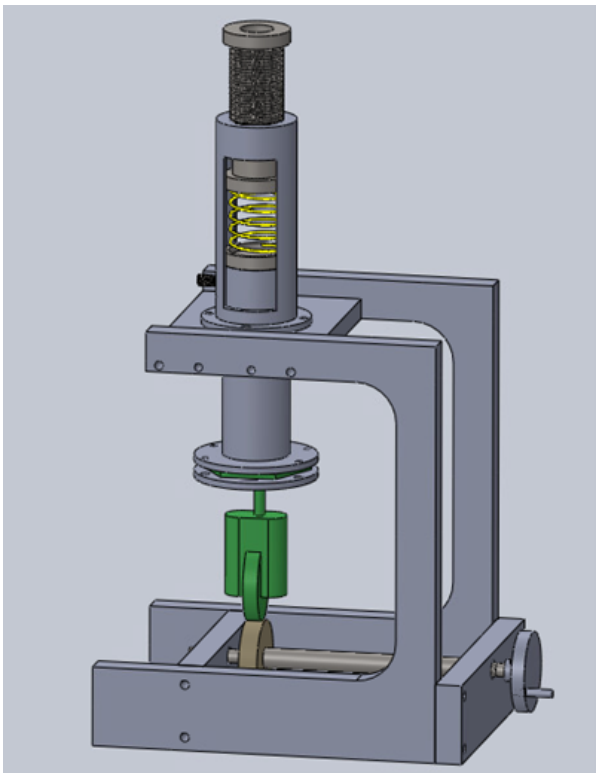

(b)

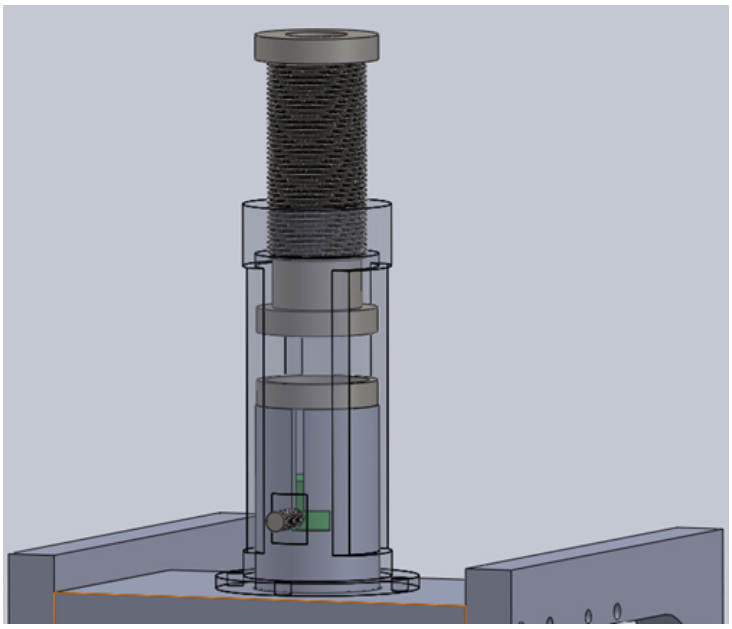

(c)

Figure 5.4: Final version of the thermal sealer: (a) and (b) overall views, with the spring highlighted in yellow and the sealer in green; (c) internal compression mechanism and sliding system with set screw for axis alignment and wheel positioning. Figures (a) and (b) also show how the new clamping system, based on the protective plate, makes the sealer more compact and stable.

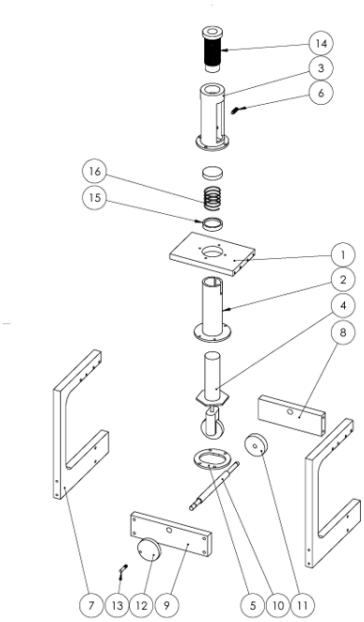

Distinta materiali

Num. articolo	Num. parte	Quantità
1	Piastra superiore	1
2	Cilindro contenitivo	1
3	Cilindro di scorrimento	1
4	Saldatore originale	1
5	Piastra per fissaggio	1
6	Grano per scorrimento	1
7	Supporto laterale	2
8	Supporto frontale	1
9	Supporto posteriore	1
10	Albero	1
11	Ruota	1
12	Manopola	1
13	Perno manopola	1
14	Manopola di compressione	1
15	Rondella per molla	2
16	Molla	1

Figure 5.5: Exploded view and bill of components of the final version. The clamping system through the protective plate can be observed.

In Figs. 5.4(a) and 5.4(b), the complete sealer is shown. The spring inside the cylindrical housing is highlighted in yellow, and, as also visible in the exploded view of Fig. 5.5, the clamping of the sealer is now achieved through its protective plate. Fig. 5.4(c) shows the internal compression mechanism and the sliding system with a set screw, which locks the cylinder in place and maintains the alignment between the axes of the two rollers. The same sliding system also provides a way to keep the heated wheel in a raised position when required.

5.1.2 Spring Selection and Pressure Control System

The focus can now be placed on the pressure generation system, which required the design and selection of a suitable compression spring. From the preliminary manual tests, the optimal compressive force needed to weld the sheets was estimated between 1.2 and 2 kgf. Since the heating wheel and its attached components weigh between 400 and 700 g, the spring had to provide an additional force in the range of 0.5–1.5 kgf.

The design process began with a survey of commercially available springs in order to identify a realistic range of geometric parameters, including outer diameter, free length, wire diameter, and number of active coils. For the calculations, harmonic steel was considered as the material, with a shear modulus $G = 79 \times 10^3$ MPa adopted for stiffness estimation. The standard theoretical formula for cylindrical helical compression springs was applied:

$$k = \frac{Gd^4}{8D^3n} \tag{5.1}$$

where d is the wire diameter, D the mean coil diameter, n the number of active coils, and G the shear modulus of the spring material. Since catalogues often do not provide the stiffness k directly, this expression was used to estimate it from the geometric parameters of the available springs.

The ranges considered in the research are reported in Table 5.1.

Characteristic	**Value**
Outer diameter	30–40 mm
Free length	40–60 mm
Active coils	3–7
Wire thickness	1.5–2.5 mm

Table 5.1: Ranges considered for compression spring parameters.

From the values shown in the table above, it was decided to consider harmonic steel springs with outer diameters of 30, 35, and 40 mm, a free length of 50 mm, wire thickness between 1.5 and 2.5 mm, and 3 to 7 active coils.

The results were represented as force–displacement maps for the three different outer diameters. In each case, the influence of wire diameter and number of active coils is shown as families of straight lines with different slopes (Figs. 5.6a–c).

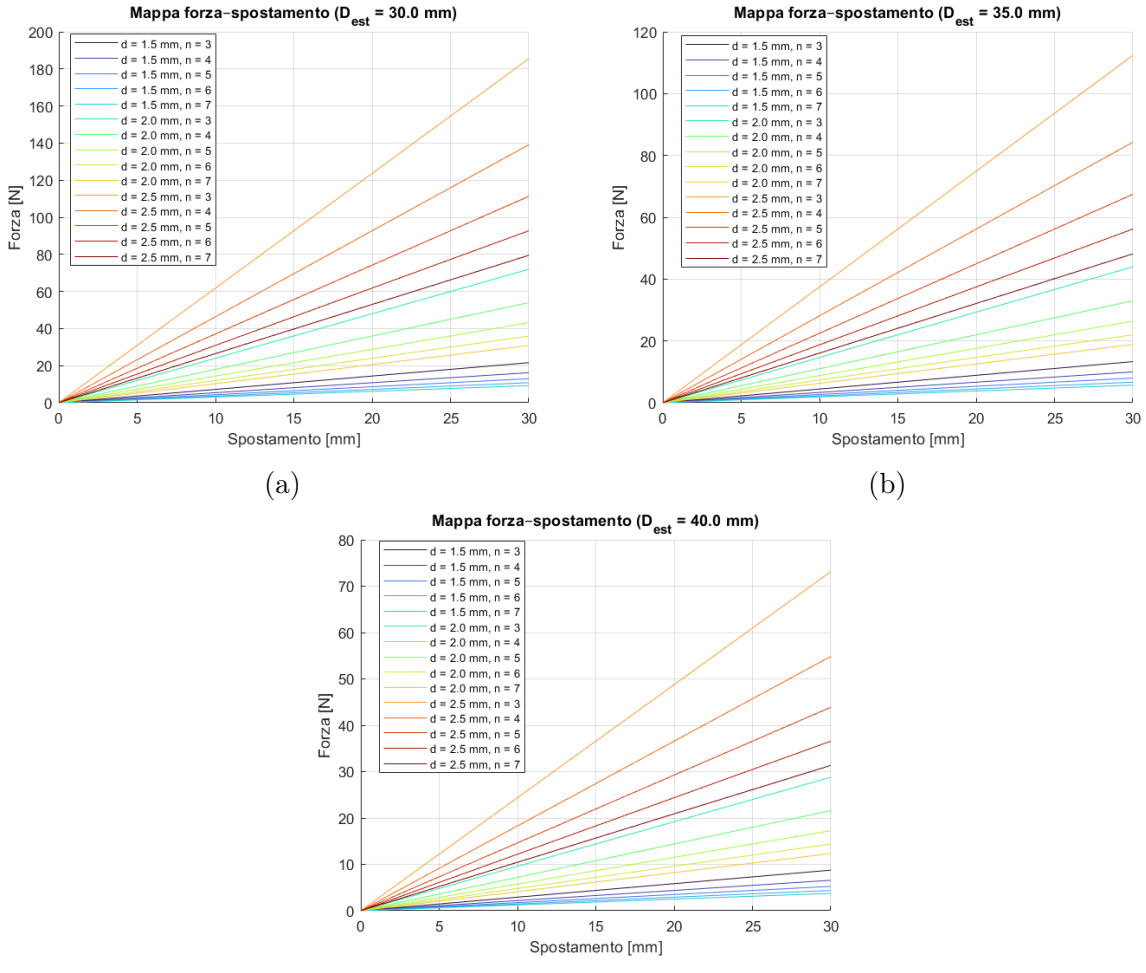

(a) (b)

(c)

Figure 5.6: Force–displacement curves for compression springs with an outer diameter of 30 mm (a), 35 mm (b), 40 mm (c). Different slopes correspond to variations in wire diameter and number of active coils.

These plots were compared with the required force range (0.5–1.5 kgf) and used to verify whether the expected deformations were compatible with the available space of the compression system, in particular the vertical movement and the related geometric clearances. Based on this analysis, several spring configurations were excluded. Springs with a wire diameter of 2.5 mm and a low number of coils exhibited excessive stiffness, producing deformations too small to allow fine adjustment of the applied pressure. Conversely, springs with a wire diameter of 1.5 mm produced deformations that were too large, making the system impractical. According to a commonly used empirical guideline in spring design, the maximum compression Δx_{max} should not exceed 30% of the free length L_0:

$$\Delta x_{max,el} \leq 0.3 L_0 \tag{5.2}$$

Otherwise, the spring may exit the linear elastic region, with unpredictable behavior and a risk of permanent deformation [49].

Another limiting factor is coil binding (contact between adjacent coils), which sets an absolute upper limit on the allowable deformation. The maximum deformation before coil binding can be estimated as:

$$\Delta x_{max,imp} = L_0 - n \cdot d \tag{5.3}$$

As shown in Fig. 5.7, this condition (red dots) is illustrated for the case with an outer diameter of 35 mm. Similar results were obtained for the other diameters considered: in all cases, coil binding occurred at deformations greater than 15 mm (30% of the 50 mm free length). Therefore, the elastic design criterion proved to be the most restrictive.

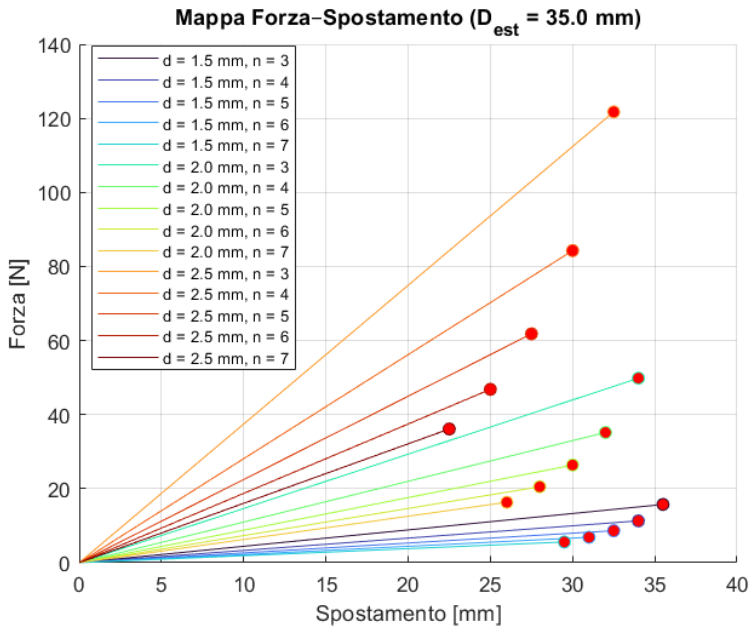

Figure 5.7: Coil binding limits for compression springs with an outer diameter of 35 mm.

5.1.3 Material Choice and Structural Analysis

The selection of materials represented the final step before the start of prototype production. Aluminum alloy EN AW-6082 was chosen for most of the structural components of

the sealer, due to its corrosion resistance, low density, and good machinability. Carbon steel C40 was adopted for parts subject to continuous rotation or sliding, such as the threaded knob for pressure adjustment and the shaft of the lower roller. For the lower roller itself, Teflon was selected mainly for thermal reasons: its low thermal conductivity prevents undesired heat transfer from the heated wheel, while its stability under moderate mechanical loads ensures proper operation.

Once the material choice was completed, a preliminary finite element analysis was carried out. The objective was not optimization, but to confirm that the structure was largely over-dimensioned and able to withstand the expected loads with wide safety margins. The analysis focused on two critical components: the aluminum side supports and the carbon-steel central shaft.

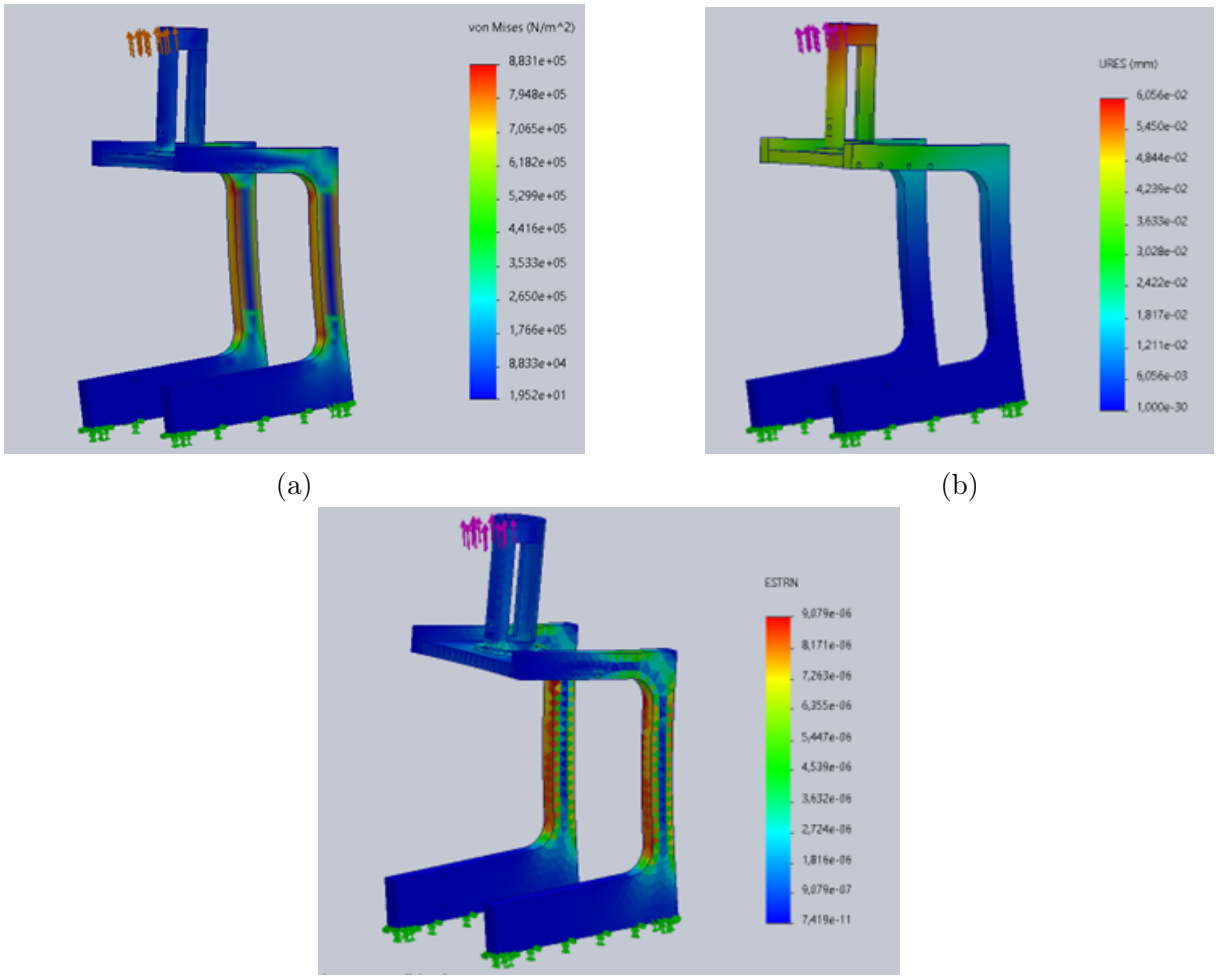

(a) (b)

(c)

Figure 5.8: Structural analysis of the aluminum side supports: (a) Von Mises equivalent stress; (b) total displacement (URES); (c) strain distribution (ε, ESTRN).

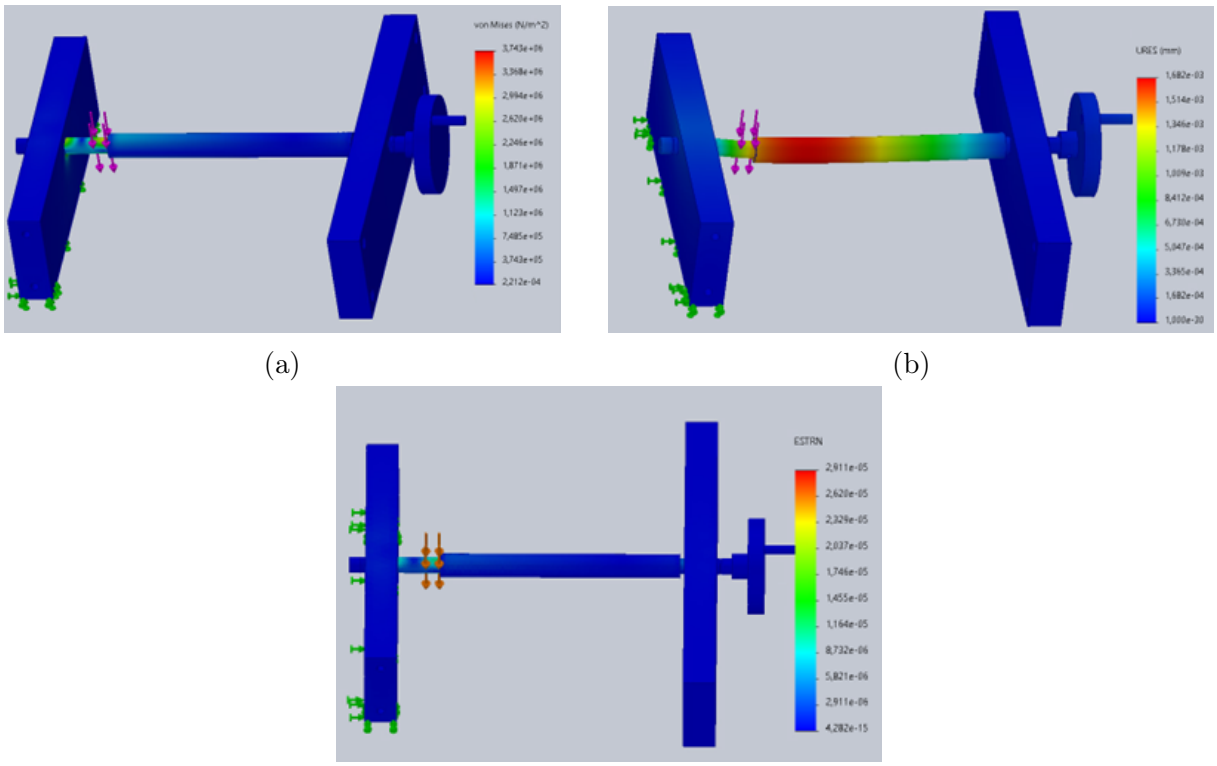

(a) (b)

(c)

Figure 5.9: Structural analysis of the carbon-steel shaft: (a) Von Mises equivalent stress; (b) total displacement (URES); (c) strain distribution (ε, ESTRN).

The results are shown in Figs. 5.8 and 5.9. For the side supports, the maximum Von Mises stress reaches 0.88 MPa, compared to a yield strength of over 100 MPa for aluminum EN AW-6082 (Fig. 5.8a). The corresponding total displacement (URES) and strain distribution (ESTRN) are negligible (Figs. 5.8b and 5.8c), confirming a fully elastic response. For the central shaft, the maximum stress is approximately 3.74 MPa, against a typical yield strength above 250 MPa for carbon steel C40 (Fig. 5.9a). Again, displacements and strains (Figs. 5.9b and 5.9c) are minimal, showing that the shaft also works entirely in the elastic region.

These results clearly indicate that the system was deliberately oversized. This choice was made at the prototyping stage to ensure robustness, simplicity of construction, and wide safety margins. If a second version of the prototype is developed in the future, weight reduction and geometric optimization can then be considered.

5.1.4 Prototype realization and balloon production tests

After the design and conception phase, the actual realization of the device was carried out. All the components were manufactured and assembled with particular attention to the mechanical couplings and joints. The spring, selected on the basis of the design considerations discussed earlier, was integrated into the compression system, making the thermal sealer ready for use.

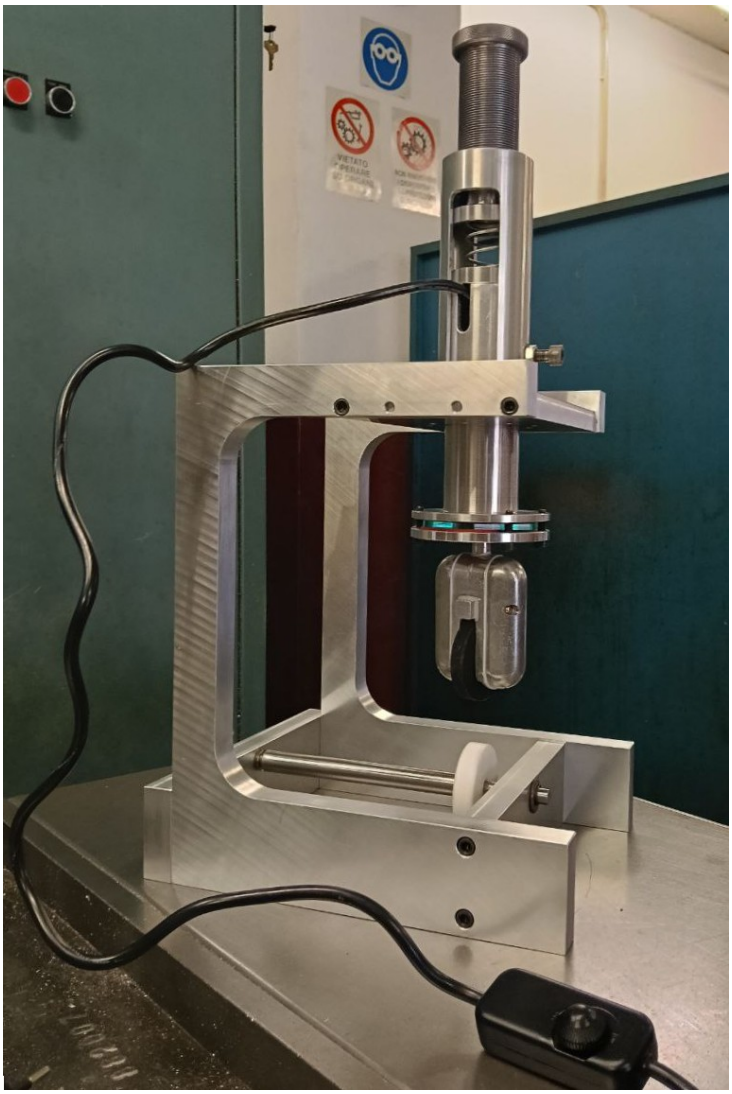

Figure 5.10: Prototype of the double-wheel thermal sealer after assembly, with integrated spring-based compression system and all structural components ready for testing.

Once the assembly was completed, the first experimental tests were carried out to verify the actual functionality of the device on Mater-Bi samples. Each sample was prepared by overlapping two layers of 30 μm film, inserted between two sheets of 0.1 mm Teflon and fixed at the edges with staples. After a short period of practice, it was almost immediate to acquire the manual skills necessary to control the advancement of the sheets through the knob connected to the shaft, immediately obtaining satisfactory welds both along linear and curved paths.

To make the tests more repeatable, two references were introduced: a graduated scale drawn on the cylinder containing the spring, useful for monitoring the position of the compression knob and therefore the level of applied load, and a second graduated scale on the potentiometer knob, for temperature adjustment. Thanks to these measures, it was possible to carry out systematic tests by varying the process parameters: combinations between four pressure settings and four temperature settings were considered, while the feed rate remained manual, with the attempt to keep it as constant as possible and adapt it to the different configurations of temperature and pressure.

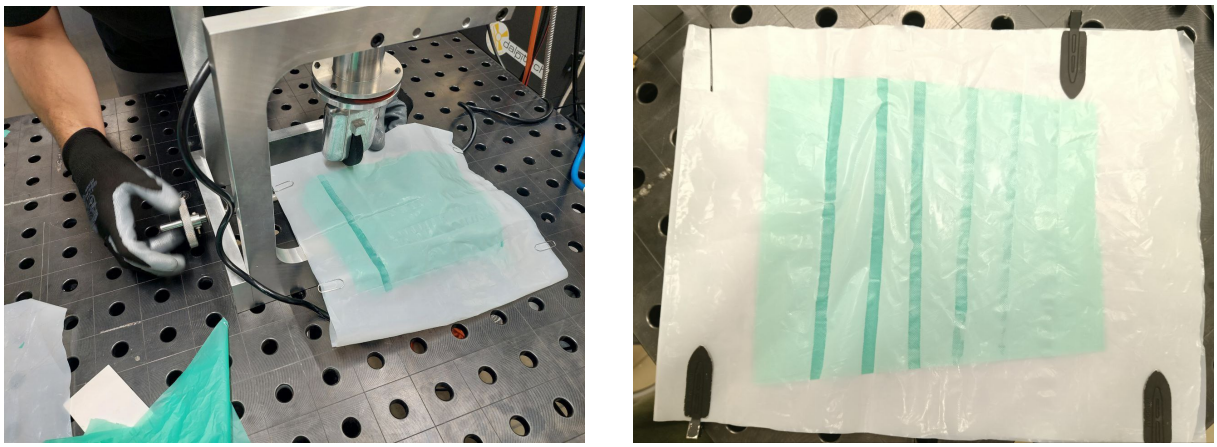

(a) (b)

Figure 5.11: (a) Experimental setup for preliminary welding tests on Mater-Bi samples: two layers of 30 μm film are inserted between sheets of 0.1 mm Teflon and fixed with staples. (b) Different welding grades obtained at constant temperature ($\sim$80 °C) and varying pressure values, showing the effect of different applied loads

The tests showed that the Teflon layer, being semi-transparent, allowed observation of color differences in the welded zones (Fig. 5.11), corresponding to different degrees of fusion of the two Mater-Bi layers. However, the visual appearance was not always indicative of the actual quality of the joint: excessive pressure, for example, caused the formation of micro-holes, almost invisible to the naked eye but dangerous from a mechanical point of view, reducing both the strength of the weld and the ability of the material to retain gas once the balloon was inflated.

Based on the experimental observations, it was possible to identify an optimal configuration of the parameters. The minimum temperature of the sealer (about 80 °C) proved to be the most suitable, associated with a spring compression of 6.60 ± 0.01 mm. Using Eq. (5.1) and considering $G = 79.3$ GPa (harmonic steel), wire diameter $d = 2$ mm, $n = 4$ active coils, and a mean diameter $D \approx 28$ mm (corresponding to an external diameter of 30 mm), the corresponding additional force was estimated to be about $F \approx 12$ N, in agreement with the range predicted during the preliminary analyses.

The feed rate was estimated at around 6.40 mm/s by timing the average rotation of the heated wheel (one revolution every 28 s).

After the optimal welding settings were confirmed on samples, production shifted to the welding of the actual components, namely the petals and the upper cap.

The four main petals were welded together with the same procedure adopted for the samples: the spring is compressed up to the desired pressure and the sealer advances along the overlapping edges of two petals. until completing the entire cycle of joints. At the end of this phase, the balloon is almost complete, but a circular hole remains open at the top, generated by the intersection of the upper edges of the four petals.

The closure of this hole with the upper cap represents the most critical part of the entire process. In previous years, in fact, this operation caused numerous difficulties: once the petals were joined, the balloon could no longer be laid flat on a surface, and it therefore became difficult to obtain a uniform and regular weld.

To overcome this issue, a special multilayer configuration was devised, specifically designed to adapt the operation to the new sealer: the upper edges of the petals and the cap are pinched together between thin sheets of Teflon, while additional thicker sheets

(see Fig. 5.12b) act both as thermal protection, concentrating the heat only on the area to be welded, and as a circular guide, allowing to follow the welding path precisely along the edge of the cap.

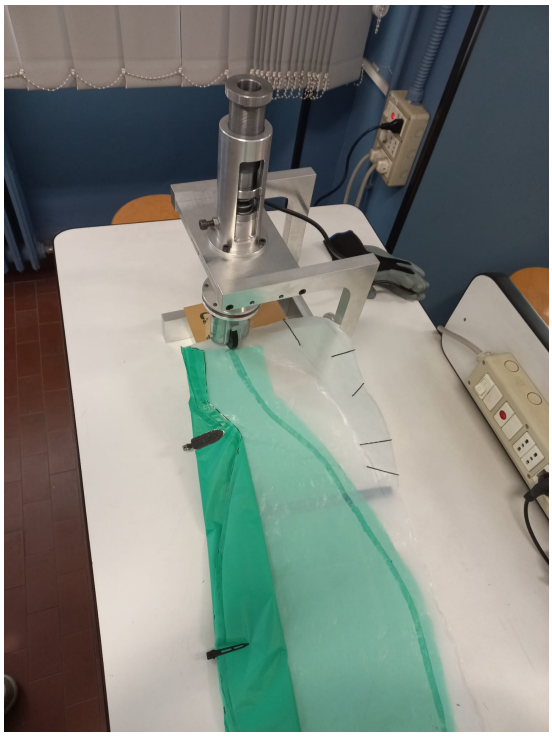

(a)

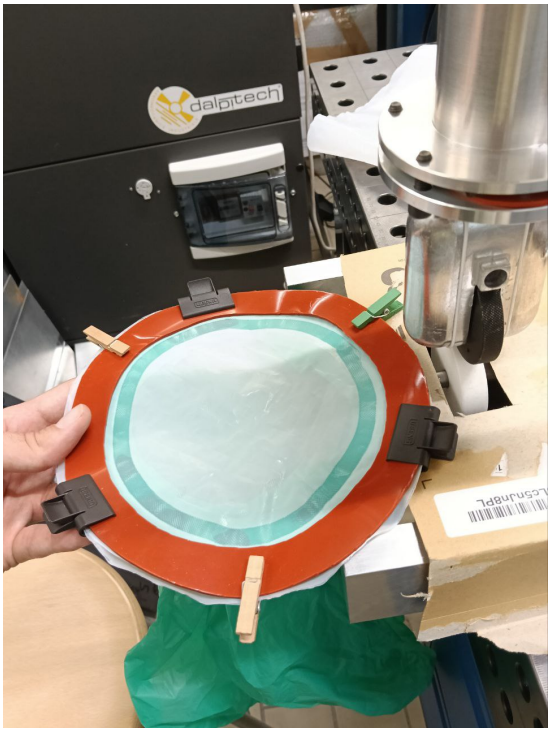

(b)

Figure 5.12: Critical phases of balloon assembly: (a) welding of petals along their overlapping edges; (b) welding of the upper cap using the multilayer configuration, providing both thermal protection and circular guidance.

Using this multilayer solution proved to be particularly effective, because it meant obtaining a good weld through a repeatable method.

Overall, a significant improvement in production times was also observed: the realization of a single balloon dropped from about 4 hours required in the past to only 30–40 minutes per unit, with a substantial gain in efficiency and repeatability.

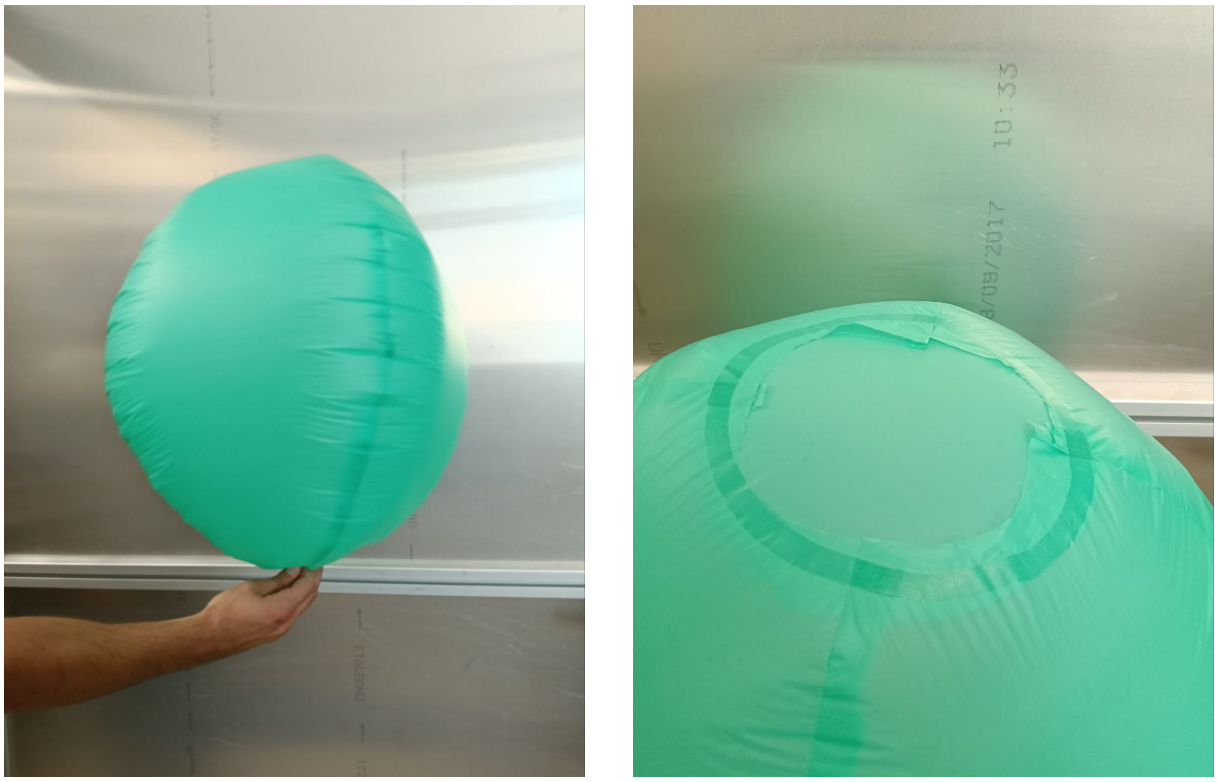

(a) (b)

Figure 5.13: Mater-Bi balloons after assembly: (a) completed and inflated balloon; (b) detail of the upper cap weld, showing the effectiveness of the multilayer configuration.

5.1.5 Gas retention test

In order to validate the reliability of the welding process, tests have been conducted on gas retention of the helium-filled balloons. Three different configurations were tested:

- a balloon welded with the thermal sealer and closed with the circular upper cap;
- a balloon welded with the thermal sealer but completed with a "double-neck" petal design;
- a test balloon provided by Grabo Srl, consisting of two circular Mater-Bi sheets welded together, originally developed as a simplified geometry for machine testing purposes.

The motivation for testing an additional double-neck solution was to check if tying one of the two necks could still ensure good retention properties, while making the overall manufacturing procedure easier, since the welding of the top cap represents the most delicate step.

All balloons were inflated with helium and connected to a ballast of 200 g. The balloons with their respective loads are shown in Fig. 5.14.

Figure 5.14: Helium retention test setup: the three balloon configurations (double-neck, top cap and Grabo sample) tied to a ballast of 200 g each. The balloons were periodically weighed together with the ballast to evaluate gas leakage over time.

The total weight of each system was measured every 30 minutes for 2.5 h, and Figure 5.15 shows the results obtained. In particular, linear fits were used (for longer time periods, exponential trends should instead be considered) to estimate the average mass-increase rate.

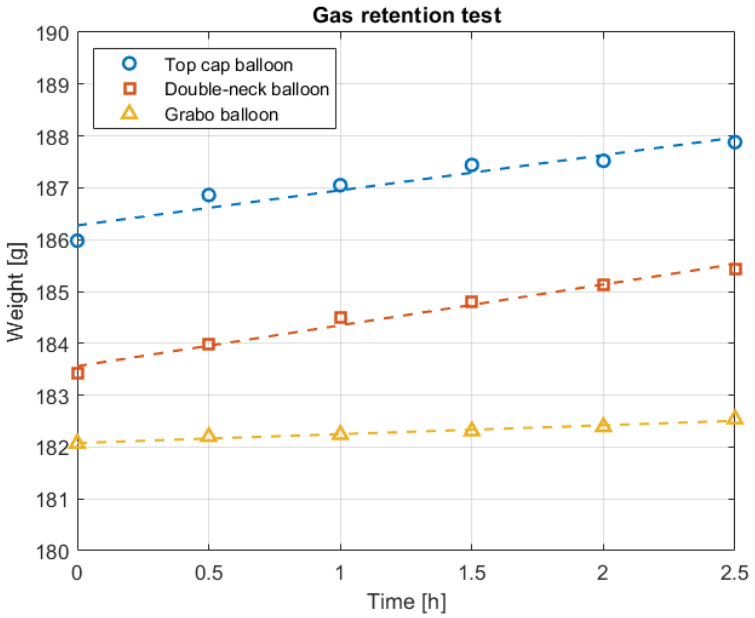

Figure 5.15: Weights measured every half hour, over a 2.5 h test window, for the three balloon configurations. Linear fits are represented by dashed lines. Measurement uncertainty is ± 0.01 g.

At this point, the helium volume loss can be derived from the mass variation using

$$\Delta V = \frac{\Delta m}{\rho_{\text{air}} - \rho_{\text{He}}},$$

where the density difference $\rho_{\text{air}} - \rho_{\text{He}} \approx 1.038$ kg/m^3 was calculated under the ambient conditions (20°C and about 1 atm) of the experiment. Table 5.2 reports the results for each balloon in terms of net mass loss, relative mass loss, and helium volume loss.

Configuration	Mass loss [g/h]	Rel. mass loss [%/h]	Vol. loss [L/h]
Top cap balloon	0.678	0.365	0.653
Double-neck balloon	0.788	0.430	0.759
Grabo balloon	0.171	0.094	0.165

Table 5.2: Net mass loss, relative mass loss, and helium volume loss over the 2.5 h test window, calculated from the linear fits. Helium volume loss is computed using $\rho_{\text{air}} - \rho_{\text{He}} \approx 1.038$ kg/m^3.

As can be seen, the Grabo balloon clearly performed better than our prototypes. This was expected: their industrial hot-stamping process is designed for reliable mass production, therefore this balloon underwent less mechanical stress compared to the prototype sealer. In addition, it should be noted that the Grabo sample has only one circular seam, which is very different from having to join four petal edges (plus the extra closure).

Focusing on our two designs, the difference is small but not negligible. The upper-cap closure performed slightly better than the double-neck solution, most likely because tightening the thread on one of the two necks locally damages the material and the nearby welds. In both cases, the helium retention may be regarded as acceptable, though far from exceptional. To give a concrete idea, considering a balloon sized as in Section 4.2 (radius 22 cm and attainable altitude $\approx$ 2000 m), the estimated altitude loss is about 162 m/h with the upper-cap closure, 188 m/h with the double-neck, and only 42 m/h for the Grabo balloon. These results can, however, suggest the direction to be pursued: reducing the number of seams (and the stress around the closure) should improve sealing and reduce the altitude loss rate.

5.1.6 Thetered launch

A further step in the validation process of the welds (and, consequently, of the thermal sealer) was carried out by performing a tethered launch of two radiosondes on the roof of Politecnico, tied to the ground with wires of about 5 m. Such a configuration by itself does not allow a detailed analysis of the turbulent dynamics (fluctuations, dispersion, Lagrangian correlations), but for this reason we adapted our objectives to what the adverse conditions predicted that day (rain and wind) could offer. In fact, we had the opportunity to evaluate, in the presence of water and gusts, the resistance of all the elements of the radiosonde, from the electronics to the balloon and the welds themselves.

Since the experiment was carried out after several launches dedicated to the validation of the communication system (discussed in detail in the next chapter), for now it is enough to say that the sondes used a standardized LoRa protocol (LoRaWAN), which allowed the transmission of data not only to a single-channel peer-to-peer receiver, but to a network

of ground stations belonging to The Things Network (TTN), in parallel with our private LoRaWAN gateway WisGate RAK7244.

Before entering the operational part of the experiment, a further consideration about the balloons produced is needed. For their production we used Mater-Bi film of 30 μm (instead of the 23 μm initially planned). If we follow the same sizing of Chapter 4.2 and keep $R = 22$ cm, we obtain a reachable altitude of 1200–1300 m. Such values could also be sufficient for a tethered test, but what was observed when connecting probe and battery to the balloons is that the system tended to neutral buoyancy, as if the payload was 4–5 g heavier. This surplus, however, was expected: neck, overlapping flaps of the petals and of the upper cap add to the balloon a weight 15–20% higher than the theoretical mass, with a non-negligible impact on the net lifting force.

As a consequence, we decided to increase the petal size up to $R = 28$ cm (+6 cm compared to the previous version). It was estimated that 6–7 g of material were in excess compared to the theoretical spherical case, and subsequent weighting tests confirmed our estimates, measuring a balloon mass of 45 g against the theoretical 38 g. Even with this increase, the maximum altitude would still have remained above 4,000 meters, a margin considered more than conservative to tolerate possible micro-damages and leakage greater than those observed in indoor tests. It is clear that this variation in weight and altitude must be integrated in the sizing when the balloons will be used in free flight launches.

With this background clarified, we can now move to the experimental phases: weighting of the components, radiosonde configuration, and tethered observations. The following table shows the weight distribution averaged over the two sondes:

Component	**Weight (g)**
Balloon (30 μm thickness)	43
Battery (450 mAh)	11.5
Probe	6.5
Connections	1.5
Protection	0.5
Total	**63.5**

Table 5.3: Weight distribution of the radiosonde system.

What makes this case different from the others is the addition of a protection: in view of rain it was necessary to cover the PCB circuits with a thin adhesive tape, leaving free the ventilation hole of the humidity sensor to avoid compromising the measurements.

Figure 5.16: Weighting phase of the radiosonde system using a precision balance. The PCB is connected to a 450 mAh battery, and the protective adhesive tape leaves free the ventilation hole of the sensor (visible in the bottom right corner).

Each of the two radioprobes was connected to its battery and balloon, and after checking the correct functioning of sensors and LoRaWAN transmission, the sondes were tied to weights, starting the experiment.

Figure 5.17: Tethered radiosondes on the roof of the Politecnico. This photo captures the moment just after the rainfall, when the decrease in wind allowed the balloons to return to a nearly vertical position.

As soon as they were tethered at 1:30 PM CEST, the radiosondes encountered a phase

of strong winds (horizontal gusts typical of a downburst associated with a thunderstorm cell) that stressed the balloons mechanically, with ground impacts and jerks of the tether. When the rain arrived shortly after, the wind calmed and the balloons more easily kept a vertical position. The increase in weight due to droplets on Mater-Bi and on the PCB casing did not affect much their lift, and the balloons always maintained a certain altitude above the ground. Subsequently, the sky cleared (Figure 5.17) and the weather remained partly cloudy for the rest of the day, until the last transmissions around 9:00 PM CEST.

Looking at the environmental data received, it can be stated that the probe transmitted correctly in any meteorological condition, until battery depletion, whose autonomy was estimated around 8 hours.

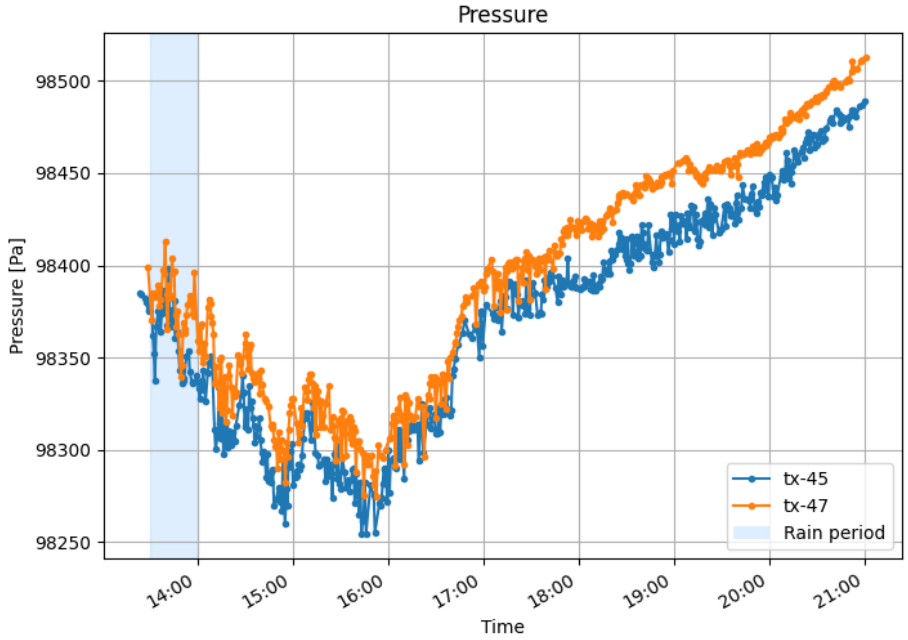

Figure 5.18: Atmospheric pressure recorded during the tethered experiment. Variations remain small over the entire time window of the experiment. The blue-shaded region indicates rainfall.

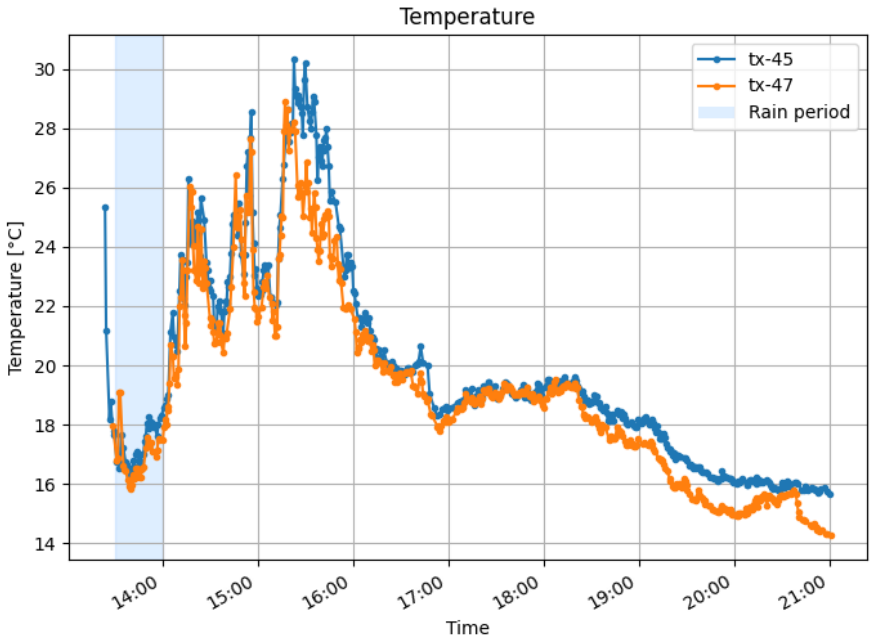

Figure 5.19: Temperature measured during the tethered experiment. An initial decrease during rainfall (blue-shaded region) was followed by oscillations on the scale of tens of minutes, attributable to intermittent radiative heating under variable cloud cover.

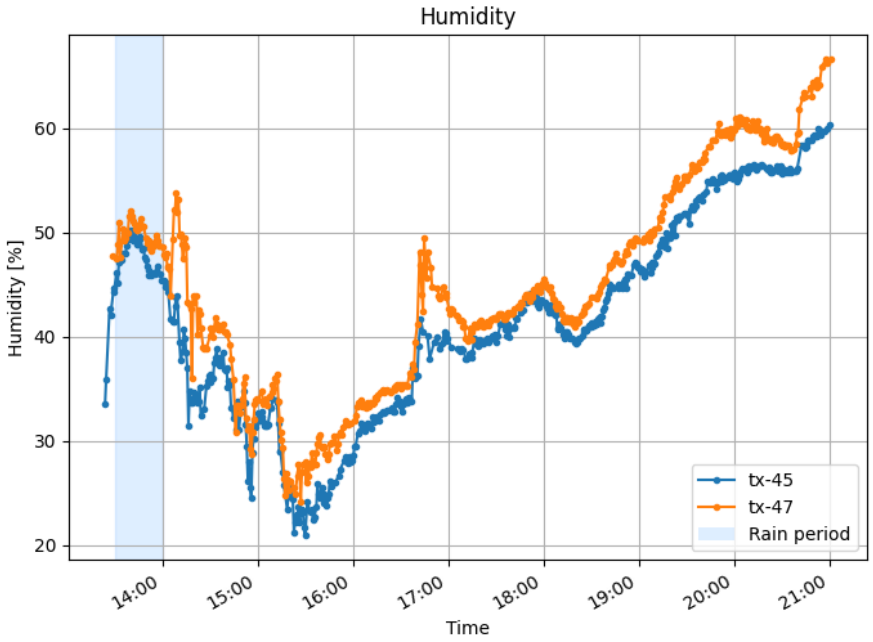

Figure 5.20: Relative humidity recorded during the tethered experiment. The rainy phase (blue-shaded region) shows an RH increase, while subsequent oscillations exhibit peaks opposite to those of temperature.

Figure 5.18 shows the pressure trend, where the variations are very small (on the order of a few tens of Pa), compatible with normal diurnal oscillations or the effects of the passage of a storm cell.

Figures 5.19 and 5.20 show instead the temperature and relative humidity. In the first phase of the experiment, the blue region highlights the presence of rain, which caused an increase in relative humidity and a parallel decrease in temperature due to cooling induced by the convective downburst.

Later, oscillations with a period of some tens of minutes can be observed, showing opposite peaks between them. These oscillations are most likely linked to intermittent radiative heating due to cloud cover and to residual turbulence associated with the passage of the thunderstorm cell.

It might then be interesting to use this opposition of peaks between temperature and humidity o briefly describe how the relative humidity measurement of our Bosch BME280 sensor works. This device uses the variation of electric capacity of a polymeric film to associate the absorption of water molecules with the effective vapor content in the air (absolute humidity). By integrating this measurement with the temperature one (coming from the same sensor), the relative humidity is calculated, defined as

$$RH = \frac{e}{e_s(T)} \times 100,$$

where e is the partial vapor pressure (derived from the absolute humidity) and $e_s(T)$ is the saturation pressure at temperature T.

It follows that, in the moments when temperature increases, the capacity of the air to contain vapor increases, and conversely when it cools down. Therefore, going back

to our data, what could have happened is precisely that relatively rapid variations of temperature, accompanied by a more stable actual vapor content, may have significantly varied the relative humidity, giving those opposite peaks compared to the thermal profile.

Regarding the measurements provided by the IMU (Inertial Measurement Unit), the acceleration and magnetic field components acquired by both probes were analyzed. To make their comparison more immediate, the local PCB reference system was transformed into the North–East–Down (NED) system using quaternions (i.e., rotation matrices). The components were then summed vectorially to obtain the magnitudes of acceleration and magnetic field, and the overall results are reported in the subfigures of Figure 5.21.

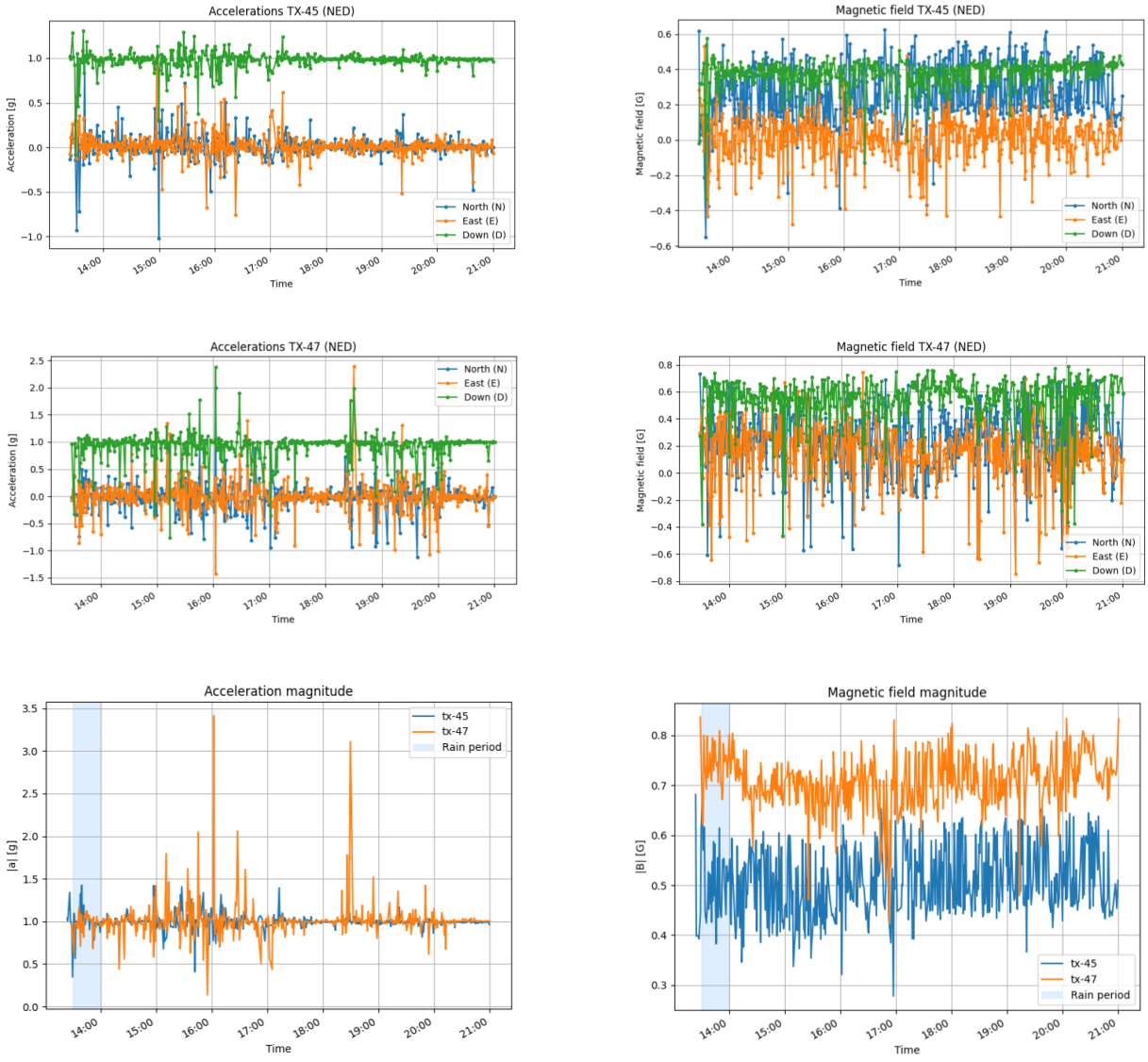

Figure 5.21: IMU measurements in the NED reference frame. Left column: acceleration components for sondes 1 and 2, and their magnitude (panels a–c). Right column: magnetic field components for sondes 1 and 2, and their magnitude (panels d–f). Components are rotated from the probe frame to NED using quaternions, and magnitudes are obtained by vector sum.

As for the accelerations, the measured values can be considered reliable: the Down component has a mean value close to $1\,g$, representing the influence of the gravitational

acceleration, while the other two components oscillate around zero. The large oscillations of the magnitude (panel (e)), particularly for sonde 47, are almost certainly attributable to impacts with the ground due to some stronger wind gusts.

For the magnetic field, sonde 47 shows a *bias* offset of the mean value with respect to what is expected for Turin (0.45–0.50 G), which is instead observed in the other sonde. However, both sondes exhibit anomalous oscillations of the magnitude $|\mathbf{B}|$, and further analyses will be necessary to identify the nature of the problem.

Overall, this tethered experiment can be considered a success for the radioprobe, which was able to withstand adverse weather conditions and continue transmitting until the batteries were depleted. Even more importantly, in the context of this chapter devoted to the soldering prototype, the integrity of the balloons and the solder joints was preserved, despite being immediately tested in a harsh and challenging environment.

Chapter 6

In Field Experiments

6.1 Preliminary LoRaWAN Experiment

This experiment was mainly focused on testing data transmission collected by a radiosonde using the LoRaWAN protocol. For the first time in the history of the project, this communication protocol was implemented, taking advantage of a public network for the reception and collection of data.

Before discussing the results obtained, it is helpful to briefly introduce what LoRaWAN technology is and what advantages it brings to our project.

The term LoRa refers to a Long Range communication technology, characterized by low power consumption and a low bitrate (from 0.3 kbps to 50 kbps). The frequency band in which it is employed is typically 868 MHz (unlicensed in Europe), and it is well suited to cases such as ours, where the volume of data to be communicated is limited, but at the same time long transmission ranges and as low power consumption as possible are required. If we speak of LoRaWAN, instead, we are referring to a higher-level protocol, built on top of LoRa. It is based on a star architecture, where nodes (our sondes) communicate with one or more gateways (receiving stations), which in turn forward the data to a central network server. But what are the benefits of adopting LoRaWAN communication in our project?

- Extended coverage: LoRaWAN gateways form a highly distributed network, allowing us to track the sondes over long distances (as long as they remain within the network coverage).
- Redundancy: Data from the same probe can be received at the same time by multiple gateways, reducing the chances of data loss.
- Resistance to packet collisions: A property of LoRaWAN gateways is that they can receive packets using multiple channels and different Spreading Factors (SF). This diversification greatly increases the number of sondes that can potentially be used simultaneously and significantly reduces the risk of collisions among their transmissions.
- Simple scalability: It is easy to increase the number of sondes operating on the same network, because in such a case no hardware changes on the node are required.

Up to this point in the HOUSEFLIES project, communication was done in LoRa peer-to-peer (P2P) mode, using a private channel. The reason is to be found in the ease

and flexibility of implementation of this mode, as it did not impose strict constraints on communication: no rigid rules on packet formats, authentication, or other aspects, and the data transmission could then be customized ad hoc for the needs of the project. By contrast, adopting a standardized network protocol such as LoRaWAN introduces several constraints: packets must follow a standardized format, payloads must be encrypted, devices must implement authentication, and transmissions are subject to duty-cycle limits (maximum 1% in Europe), which in turn constrain the management of parameters such as the spreading factor (SF) and the time-on-air (ToA).

The LoRaWAN network used in this experiment was *The Things Network (TTN)*. Its gateways are distributed worldwide, allowing sondes' trajectories to be tracked from virtually anywhere.

6.1.1 Experiment Setup

The experiment was set up with the following instruments:

- Radioprobe V1: The first, consolidated version of the radioprobe.
- Mylar Globe 15" Balloons: Manufactured by Grabo S.r.l. and filled with 99% helium. Each balloon had a capacity of 31 L and dimensions of 38×38×38 cm.
- Laptop: Used for managing the experiment and collecting data.
- LoRaWAN Portable Gateway: A WisGate RAK7244 model.

The current version of the radioprobe comprises a set of components, as detailed by Paredes Quintanilla et al. [40] and Abdunabiev et al. [39]:

- Radio transmission module;
- GNSS (Global Navigation Satellite System) sensor;
- IMU (Inertial Measurement Unit), including accelerometer, gyroscope, and magnetometer sensors;
- PHT (Pressure, Humidity, Temperature) sensor.

The radioprobe was configured to communicate via the LoRaWAN protocol with both the private gateway and the public network. The communication parameters were set as follows:

Parameter	**Value**
SF (Spreading Factor)	8
CR (Code Rate)	4/5
Bandwidth	125 kHz
Operating Frequency	868 MHz

Table 6.1: LoRaWAN Transmission Configuration Parameters

Specifically, the choice of SF8 allowed for a good maximum signal range and an expected packet transmission rate of about one every 23 seconds.

(a) (b)

Figure 6.1: (a) Radiosonde mounted with Grabo balloons; (b) LoRaWAN private receiving station.

Finally, the choice to use Globe balloons by Grabo S.r.l (Figure 6.1a), instead of the usual Mater-Bi balloons, was made to avoid problems related to balloons and focus more on the proper functioning of the radioprobe. Their higher weight and lower capacity compared to the classic balloons required the use of three balloons simultaneously.

6.1.2 Phases of the Experiment

The experiment was divided into two main parts: what happened before the launch and what happened after.

Before the Launch

Before launching the radiosonde, we went through several preparation steps:

1. **Weighing Components:** First, we carefully weighed all the parts of the radiosonde system. This was important to know exactly how much the whole system weighed, which helped us predict how it would fly. Here are the results:

Component	Weight
Radioprobe (instrumented PCB)	6 g
Battery	13 g
Balloon x 3	15 x 3 = 45 g
Connections (Thread + adhesive tape)	5 - 6 g
Total	**70 g**

Table 6.2: Weights of the radiosonde system components.

2. **Radioprobe Configuration:**
   In this first phase, we powered the radioprobe from the PC (to preserve battery charge), and we verified that each onboard sensor was providing valid data. We then checked the stability of the connection and the integrity of the packets received by our private LoRaWAN gateway.

3. **System Assembly and Balloon Integration:**
   After making sure that the electronic system was working properly, we proceeded with the assembly of the radiosonde. We connected the battery to the probe, secured all components, and finally attached the probe to the three helium-filled Grabo Mylar balloons. At this point, the probe was ready to be launched.

After the Launch

The radiosonde was launched at 2:24 PM Italian local time (CEST), from the roof of Politecnico di Torino. The packets transmitted by the probe were received by several LoRaWAN stations across the region, and by connecting to the cloud server The Things Network (TTN) it was possible to verify that they had been transmitted correctly. Overall, we received data from 2:24 PM until after 6:00 PM. A total of 158 packets was received during the experiment, although the last 28 were sent when the probe had already landed, so they show ground-level conditions or noise, not flight data.

6.2 Data Analysis

Trajectory and Raw Measurements

As shown in the figures below, the radiosonde began with a fast and straight vertical climb, remaining almost above the launch site. Then, it gradually changed direction, first moving southeast and later turning back toward the northwest. The total lateral displacement was limited, with the landing point located about 2.3 kilometers away from the launch location in a straight line. This modest drift was likely due to an almost complete absence of wind at low altitudes. However, if we also consider its vertical movements, the radiosonde actually traveled a total of nearly 14 kilometers, as shown in Figure 6.3.

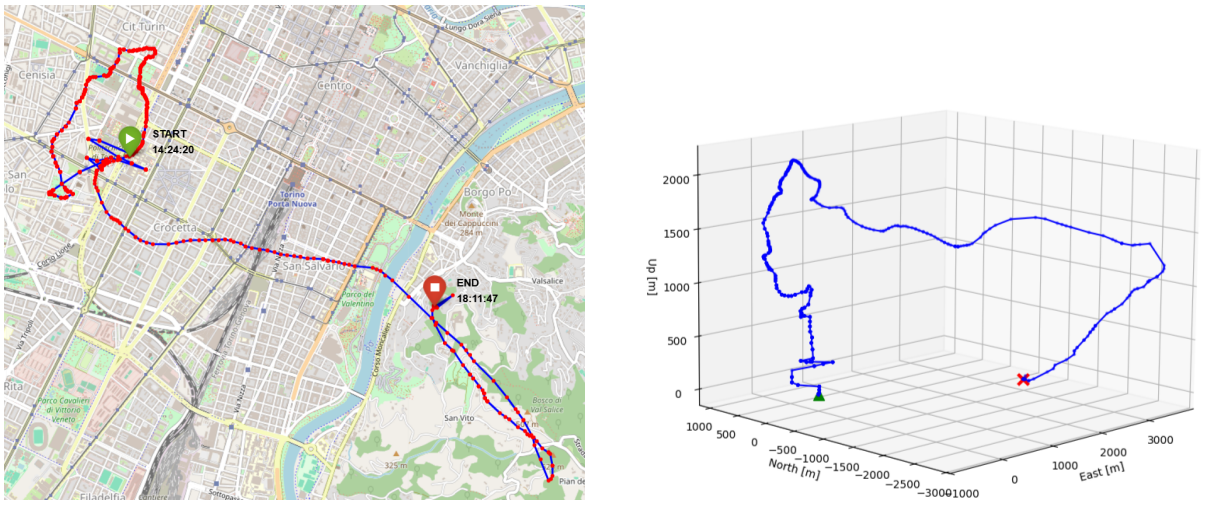

(a) (b)

Figure 6.2: (a) 2D map of the radiosonde's trajectory over Turin, showing launch and landing points; red dots represent locations where packets were received. (b) 3D plot of the trajectory in NED (North-East-Down) coordinates, with launch (green) and landing (red).

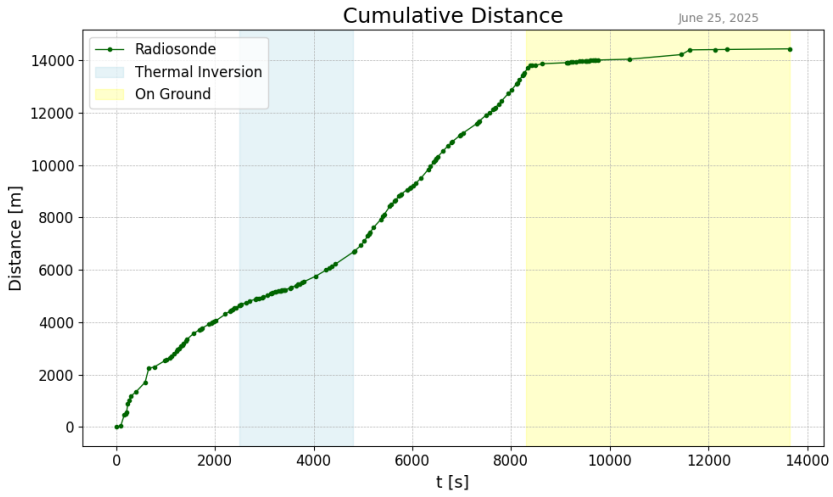

Figure 6.3: Cumulative three-dimensional distance covered by the radiosonde over time. The continued increase even when on the ground is attributed to GPS drift.

Due to firmware-related issues affecting the GPS sensor's ability to read altitude and speed, altitude data was obtained indirectly using a simplified barometric formula for the standard atmosphere:

$$h = h_0 + 44300 \left(1 - \left(\frac{p}{p_0}\right)^{\frac{1}{5.255}}\right)$$

where h_0 and p_0 represent the altitude and pressure at the launch site, respectively.

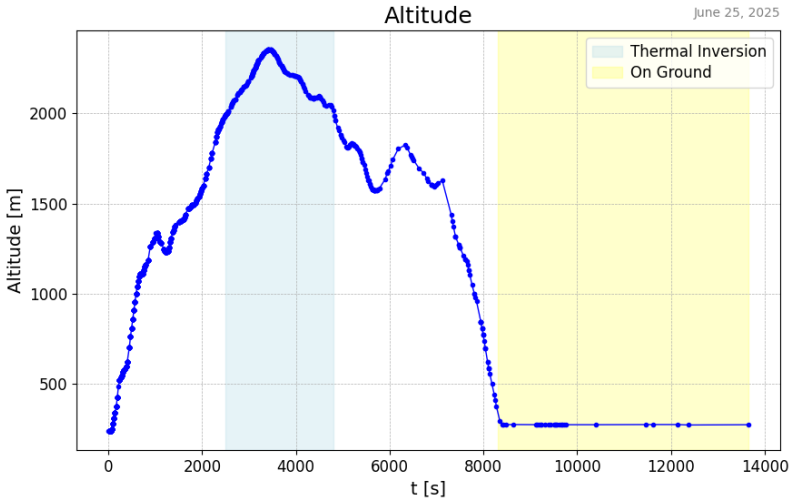

Figure 6.4: Altitude of the radiosonde over time, calculated indirectly with the barometric formula. At about 3500 s the sudden transition from ascent to descent can be observed.

The radiosonde was released at 2:24 PM and reached its highest altitude at 3:20 PM, then descended and landed around 4:42 PM. The sudden transition from an ascent phase to a descent phase, as shown in Figure 6.4, could be attributed to the detachment or damage of one or more balloons. Nevertheless, this incident did not interrupt data transmission, which continued until 6:12 PM.

During the initial phase of ascent, the radiosonde recorded a gradual decrease in temperature accompanied by an increase in relative humidity, with the latter reaching values close to 48%. Starting from around 2500 seconds after launch (approximately 3:06 PM), at an estimated altitude of about 2000 meters, a clear change is observed: the temperature reverses its trend and begins to rise, while the relative humidity drops sharply from 50% to 15% . This behavior, clearly visible in the graphs (Figures 6.5b and 6.5c), likely means that the radiosonde passed through a thermal inversion layer containing a pocket of drier air, which helps explain both the temperature inversion and the sudden drop in humidity. It is after this transition that one or more balloons appear to have failed or detached, causing the radiosonde to descend and exit the thermal inversion layer around 4800 seconds (3:44 PM).

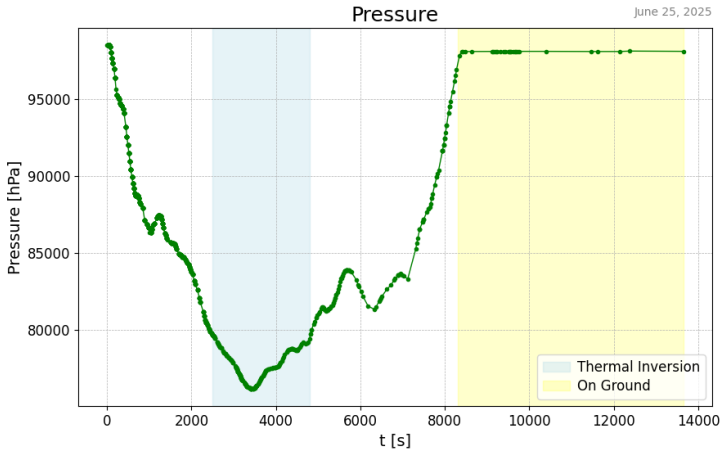

(a)

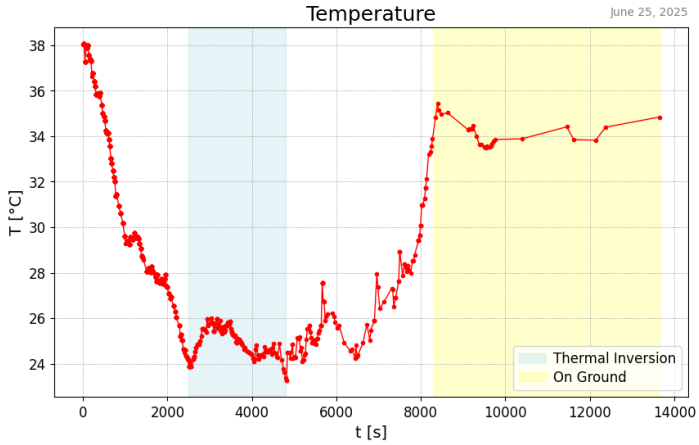

(b)

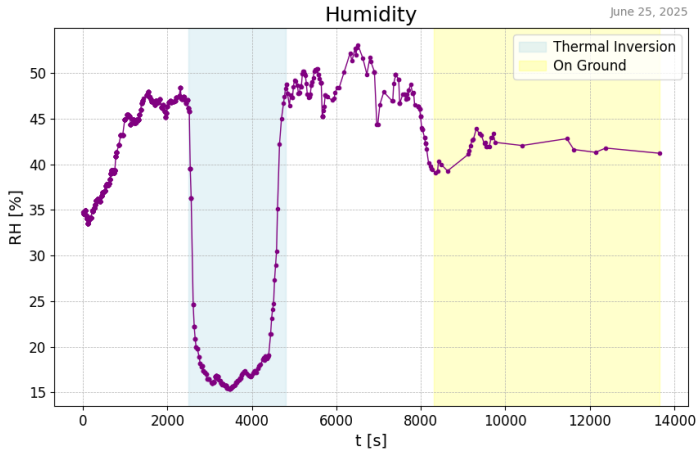

(c)

Figure 6.5: Time series of key environmental parameters recorded by the PHT module: (a) Atmospheric pressure over time, used to derive the altitude profile; (b) Temperature variation over time, highlighting the temperature trend inversion; (c) Relative humidity over time, showing a sharp decrease within the thermal inversion layer.

As previously mentioned, the velocity of the radiosonde was also estimated indirectly,

calculated from the position data derived from the GPS. This approach was preferred over integrating acceleration measurements from the IMU sensor, as the GPS data proved to be more reliable and less noisy.

Figures6.6a and 6.6b show the three components of velocity (North, East, Down) and the velocity magnitude, all expressed in the NED (North-East-Down) coordinate system, which describes the motion of the radiosonde relative to the ground.

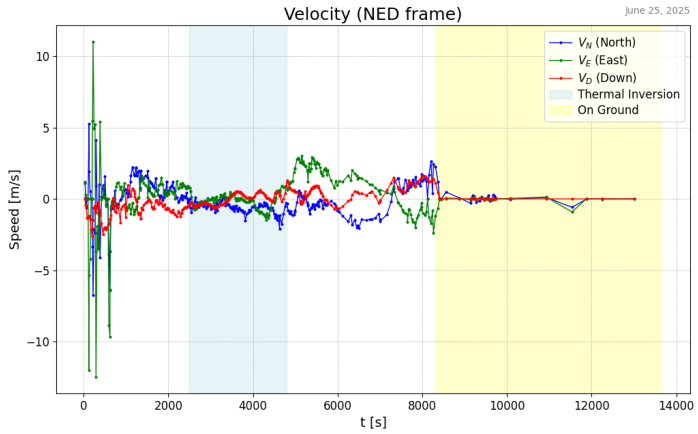

(a)

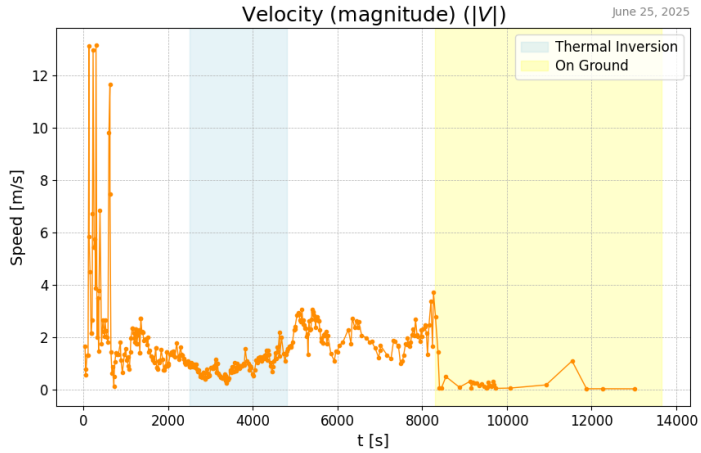

(b)

Figure 6.6: Velocity analysis based on GPS-derived position data: (a) Components of velocity in the North-East-Down (NED) reference frame; (b) Velocity magnitude over time.

Following this, Figures 6.7a and 6.7b present the components of acceleration and its magnitude, measured directly in the radiosonde's own reference frame, the body frame.

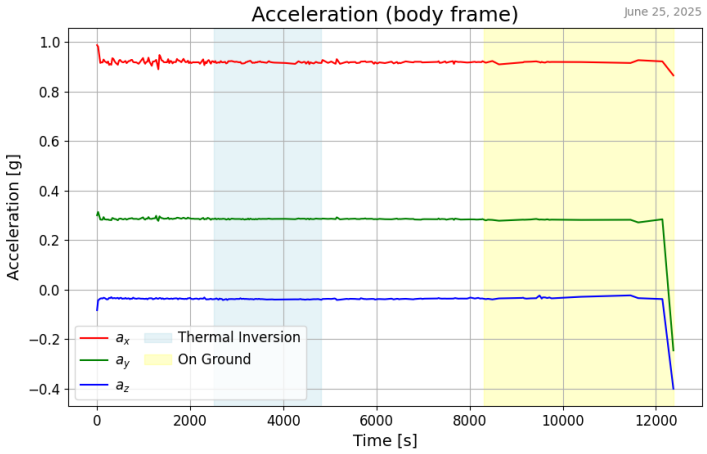

(a)

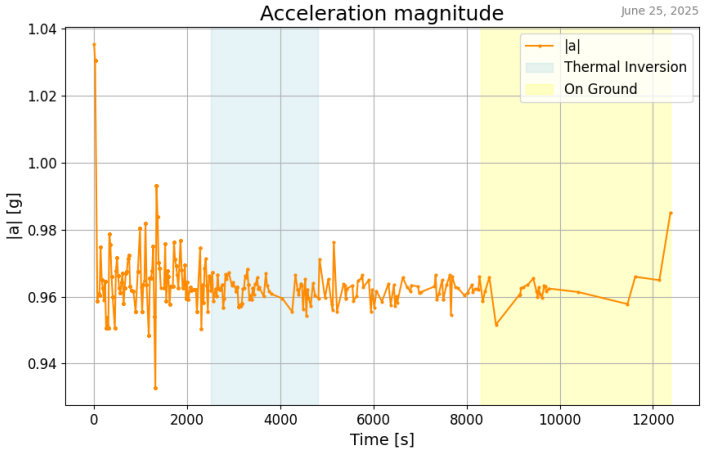

(b)

Figure 6.7: Acceleration data measured by the IMU: (a) Time evolution of the acceleration components in the radiosonde's body frame; (b) Acceleration magnitude over time, lower than the expected gravitational acceleration, likely due to an initial offset in the sensor calibration.

To perform a basic spectral analysis of the received raw data, it was first necessary to resample the time signals, since the packets were separated by highly irregular time intervals. Therefore, sampling at 10-second intervals was carried out by linear interpolation, which made it possible to apply the Fast Fourier Transform (FFT) and obtain spectra for temperature, relative humidity, and wind speed.

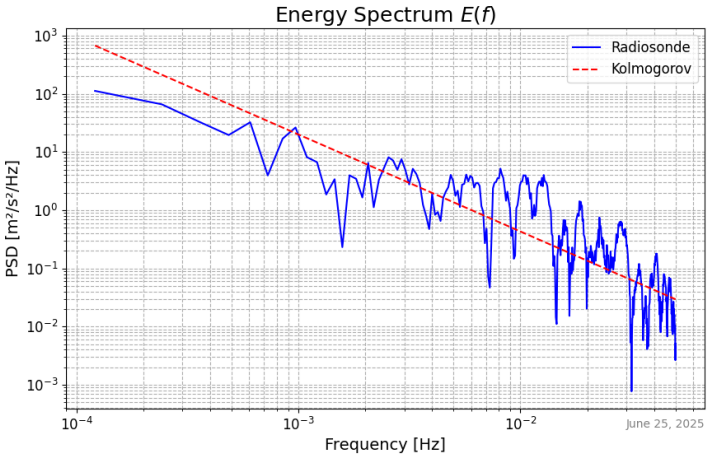

(a)

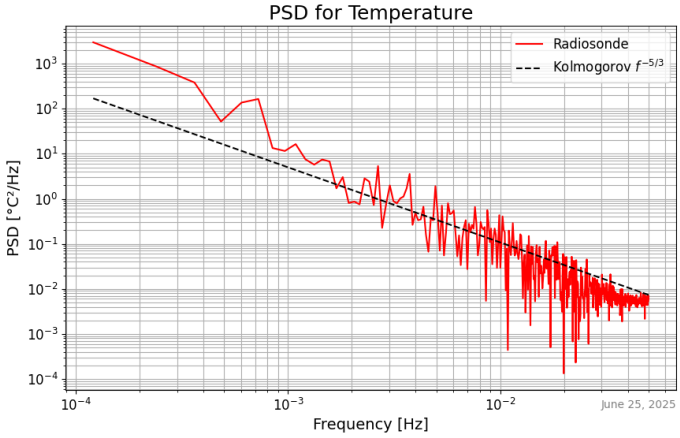

(b)

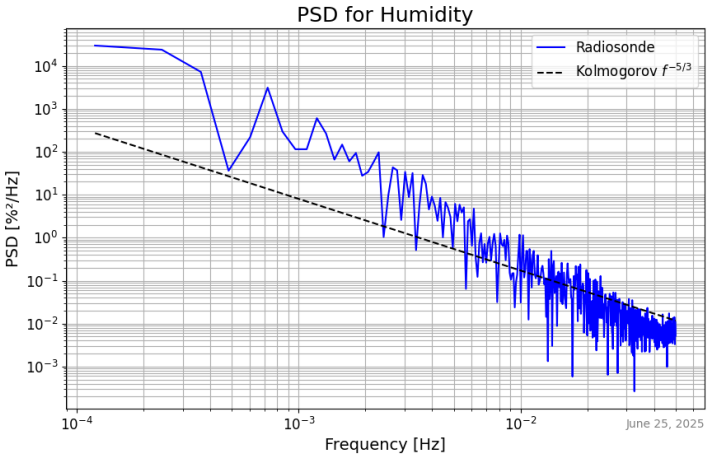

(c)

Figure 6.8: Spectral analysis of key environmental variables: (a) wind speed, (b) temperature, and (c) humidity. The data are plotted using log-log axes. A Kolmogorov trend line is included for reference. Since the original datasets featured irregular time intervals, they were resampled at uniform 10-second intervals before analysis.

Due to the artificial effects introduced by the interpolation process, these spectral

results should be interpreted as a qualitative, rather than quantitative, indication of the signal characteristics.

Data Transmission Statistics

As mentioned before, the main goal of this launch was to see if a LoRaWAN network could reliably receive and store data from our radiosonde. Overall, we found that receiving data worked well, even though we had some times when we lost data packets for short or long periods.

A total of 226 packets were successfully received by The Things Network (TTN) public network. Of these, 158 packets were collected during the flight (and on-ground) phase, while the remaining 68 packets were recorded during the pre-launch phase. The radiosonde was programmed to transmit packets every 23 seconds, utilizing a LoRaWAN SF8 configuration.

The Table 6.3 below reports the distribution of received and lost packets across consecutive reception intervals, considering the post-launch period from 2:24 PM to 6:12 PM. The reception gaps (Δt) between packets were rounded to integer multiples of the nominal transmission period.

Δt (s)	**Packets Received**	**Packets Lost**	**Received (%)**	**Lost (%)**
23	62	0	10.43%	0.00%
46	31	31	5.22%	5.22%
69	26	52	4.37%	8.75%
92	8	24	1.35%	4.04%
115	8	32	1.35%	5.38%
138	8	40	1.35%	6.73%
161	1	6	0.17%	1.01%
184	2	14	0.34%	2.36%
207	2	16	0.34%	2.69%
230	2	18	0.34%	3.03%
276	1	11	0.17%	1.85%
368	1	15	0.17%	2.52%
483	1	20	0.17%	3.36%
529	1	22	0.17%	3.70%
644	1	27	0.17%	4.54%
1058	1	45	0.17%	7.57%
1265	1	54	0.17%	9.09%
Total	**158**	**436**	**26.58%**	**73.42%**

Total Transmitted: 594 packets (100%)

Table 6.3: Distribution of received and lost packets across consecutive reception intervals, rounded to multiples of 23 seconds (the nominal transmission period of the radiosonde). The table lists, for each interval, the number of packets received and lost, along with their percentages relative to the total of 594 transmitted packets during the post-launch phase.

In particular, as shown in Table 6.3, there were two extended gaps, each lasting close to 20 minutes, during which no packets were received. It is important to note that this

occurred after the landing, hence it is presumed to be due to a combination of factors such as loss of line-of-sight to the gateways, signal obstruction by terrain or vegetation, and/or a not optimal antenna orientation.

Regarding communication between the sondes and the TTN gateways, a total of 19 stations were recorded receiving at least one packet during the launch. Figure 6.9 shows their geographic distribution; only 8 of them are displayed, because not all gateways provided location data. For reference, the local RAK7244 station at the Politecnico di Torino is also included, as it marks the launch site on the university rooftop. The southernmost gateway (visible in the map) received a few packets from approximately 83 km away, representing the maximum link distance achieved during the flight. A significant portion of the data was received by a single gateway (Figure 6.10), but there were also periods of excellent coverage in which up to six gateways simultaneously received the same transmission.

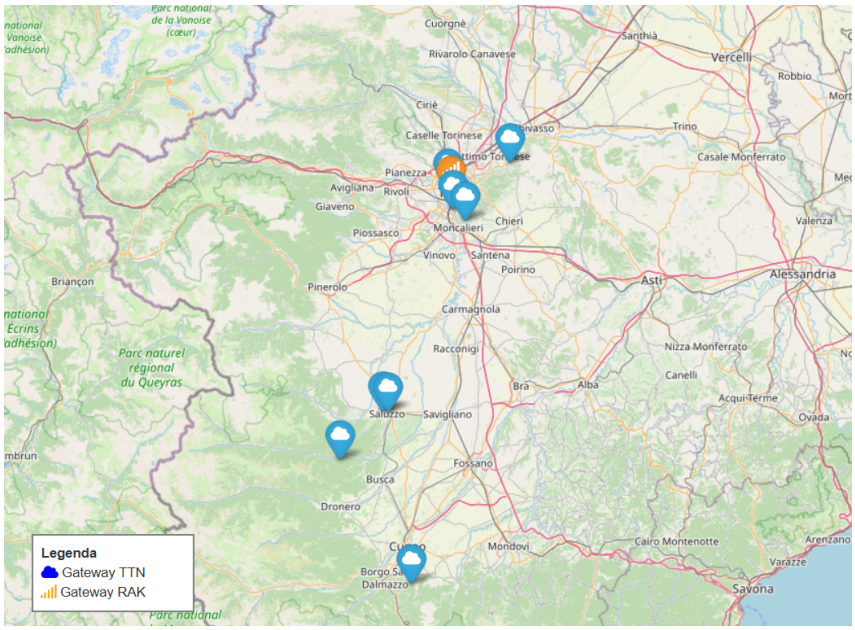

Figure 6.9: Distribution of the 8 TTN gateways which provided available location data, with the private RAK7244 station marking the launch site at the Politecnico di Torino. The southernmost gateway represents the maximum recorded distance of approximately 83 km.

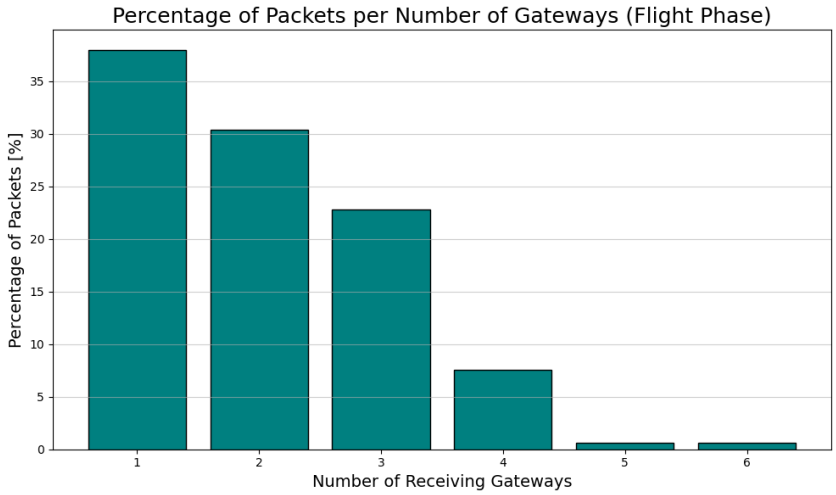

Figure 6.10: Percentage distribution of received packets versus the number of gateways that simultaneously received them. Most packets were collected by a single gateway, with up to 6 gateways occasionally receiving the same transmission.

Considering the entire duration of the flight and the post-landing phase, the TTN network yielded an average reception interval of 86.93 seconds, corresponding to 0.011 packets per second. When including the packets received by the private RAK7244 gateway, operating with the same transmission parameters, the average interval improved to 51.50 seconds. Restricting the analysis to the flight phase only, the mean interval further decreased to 35.22 seconds (0.028 packets per second), getting closer to our intended 23-second target.

Although these intervals are not yet ideal, it is expected that operating in an area with a higher density of LoRaWAN receiving stations would effectively mitigate the issue of data packet loss.

6.3 Cluster LoRaWAN Experiment

After validating in the previous experiment the reliability of LoRaWAN communication through the public TTN network, on July 22, 2025 it was possible to proceed with a full cluster launch of radiosondes. The experiment took place at the Centro di Agrozootecnia Tetto Frati in Carmagnola (TO), a research facility of the University of Turin dedicated to agricultural and zootechnical studies. The choice of this site was motivated by the presence of a meteorological and piezometric station operated by ARPA Piemonte, which provides surface meteorological and hydrological measurements (pressure, temperature, humidity, precipitation, wind and solar radiation) useful as reference [50].

Technical staff from ARPA Piemonte and ItalMeteo also took part in the launch. Their contribution was essential for monitoring winds and other environmental conditions during the preparations, as well as for the general organization and experimental activities.

A significant milestone was reached: for the first time in the history of the project it was possible to launch simultaneously **20 radiosondes**, doubling the maximum number of sondes launched so far (10). This achievement was made possible thanks to the availability of a public communication network (*The Things Network*, TTN), which allowed the management of a large number of devices in parallel.

Figure 6.11: View of the southern side of the Centro di Agrozootecnia Tetto Frati in Carmagnola (TO). Meteorological and piezometric instruments operated by ARPA Piemonte are visible in the background.

6.3.1 Experiment Setup

The experiment was set up with the following instruments:

- 20 Radioprobe V1: the consolidated version of the radioprobe.
- 20 Mylar Globe 19" balloons: manufactured by Grabo S.r.l. and filled with 99% helium. Each balloon had a capacity of 63 L and dimensions of 48×48×48 cm.
- Laptop: used for managing the experiment and collecting data.
- LoRaWAN portable gateway: a WisGate RAK7244 model.
- Four single-channel LoRa gateways: Dragino LG01v2 model.

The radioprobe used in this launch was based on the consolidated design already described in Section 6.1.1, and therefore included: a radio transmission unit, a GNSS receiver, an IMU (accelerometer, gyroscope, magnetometer), and a PHT sensor (pressure, humidity, temperature).

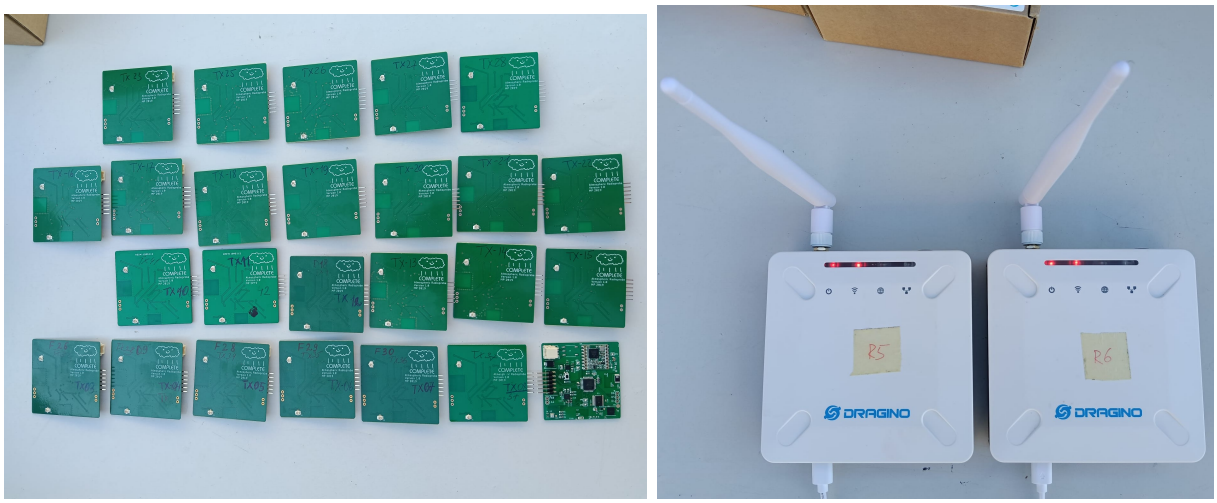

(a) (b)

Figure 6.12: (a) The 20 probes during the configuration phase, before being attached to the batteries and Mylar balloons; (b) Two single-channel Dragino LG01v2 gateways.

Communication of the sondes was configured to use the LoRaWAN protocol, relying both on the network of public TTN gateways and on a private RAK7244 station. In parallel, peer-to-peer (P2P) mode was also implemented through four Dragino LG01v2 receivers, with a planned autonomy of about one hour after launch. Two of the probes were selected to be tracked in real time via LoRa P2P: a vehicle was equipped with two Dragino LG01v2 receivers and used to follow their positions, improving their data reception witihin the one-hour communication window. The selected LoRaWAN communication parameters are reported below:

Parameter	**Value**
SF (Spreading Factor)	9
CR (Code Rate)	4/5
Bandwidth	125 kHz
Operating Frequency	868 MHz

Table 6.4: LoRaWAN transmission configuration parameters used during the 22/07/2025 launch.

In this launch SF9 was preferred over SF8 (used in the previous single-probe test), mainly to increase the reception range. Although this reduced the transmission rate to one packet every 42 seconds, the data frequency was still sufficient for the experiment and ensured a more reliable link.

As for the balloons, once again it was decided to employ Mylar models manufactured by Grabo S.r.l. instead of the Mater-Bi balloons, because the latter are still under development (both internally at Politecnico di Torino and by Grabo as non-spherical test productions) and are therefore not yet reliable enough for flight experiments of this type. Compared to the previous launch at Politecnico, spherical balloons with double the volume (63 L) were chosen, so that each probe could be carried by a single balloon while still reaching approximately the same floating altitudes.

6.3.2 Preparation, launch and reception

Preparations before Launch

Before performing the launch, several preparation steps were carried out, which required a few hours of activity. First, the 20 balloons were inflated (Figure 6.13), while in parallel the peer-to-peer (P2P) receivers and the LoRaWAN private gateway were configured.

Subsequently, each radioprobe was powered on and tested to ensure correct operation of all onboard components. We verified that the sondes could successfully connect both to our LoRaWAN gateways and to the Dragino receivers.

Figure 6.13: Nineteen-inch Grabo Mylar balloons inflated and temporarily secured to a support pole before being attached to the probes.

After these checks, we were able to proceed with the system assembly: the battery was connected to the probe, and the entire system was secured with a thread to the helium-filled Grabo Mylar balloons. After verifying one last time the correct data transmission, the sondes were ready for launch.

After the Launch: data reception

The launch of the 20 radiosondes took place at 12:20 CEST, after which we monitored whether the data packets were being correctly received both by the local P2P receivers and by the LoRaWAN gateways. We immediately observed that two sondes (TX01 and TX02) did not connect to the public TTN LoRaWAN gateways. Therefore, data were available only for the first hours, until they moved out of range of the private on-site LoRaWAN station.

(a)

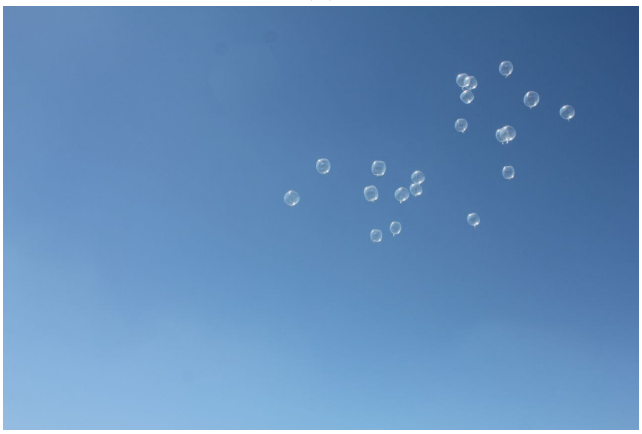

(b)

Figure 6.14: (a) Release of the 20-sonde cluster from the launch site; (b) the cluster approximately one minute after launch, with the balloons already dispersing under the prevailing wind.

Across all 20 sondes, the average data reception duration after launch was 7 hours and 55 minutes, even if we include the two that never connected to public stations and the two that were damaged shortly after launch, which landed prematurely little more than one hour later (this will be discussed later).

Excluding these four cases, all remaining sondes maintained all three communication links and operated for at least 7 h; two exceeded 15 h (as will be visible in the figures of the next chapter). The large differences in lifetime can be attributed to two main factors:

- the use of batteries with different nominal capacities (450, 500, and 550 mAh), which leads to endurance differences of several hours;
- the different flight trajectories followed by the sondes, which led to landings or splashdowns at different times and under different conditions, sometimes causing early damage and transmission interruption.

In total, 17249 packets were received, including:

- 11854 from the network of public TTN gateways,
- 1876 from the private LoRaWAN gateway,

- 3519 through P2P communication with the Dragino receivers.

This represents a substantial dataset. However, it must be stressed that these are raw packets which require subsequent processing steps, such as deduplication and the removal of corrupted or incomplete payloads, which significantly reduce the final number of usable data.

Despite the large amount of collected data, it is equally important to consider packet losses. Focusing on LoRaWAN transmissions only, and assuming a nominal transmission interval of 42 s (as set by SF9), the comparison between the expected number of packets over the sondes' flight durations and the packets actually received indicates an overall data loss of about 82%. This high loss rate can be mainly attributed to the limited and non-uniform coverage of LoRaWAN receiving stations along the flight trajectories.

Regarding communication with the TTN infrastructure (including our own gateway), the sondes were received by a total of 91 distinct gateways, with a peak of 26 gateways simultaneously detecting the same packet. The percentage distribution of packets with respect to the number of simultaneous gateways is reported in the following histogram (Figure 6.15).

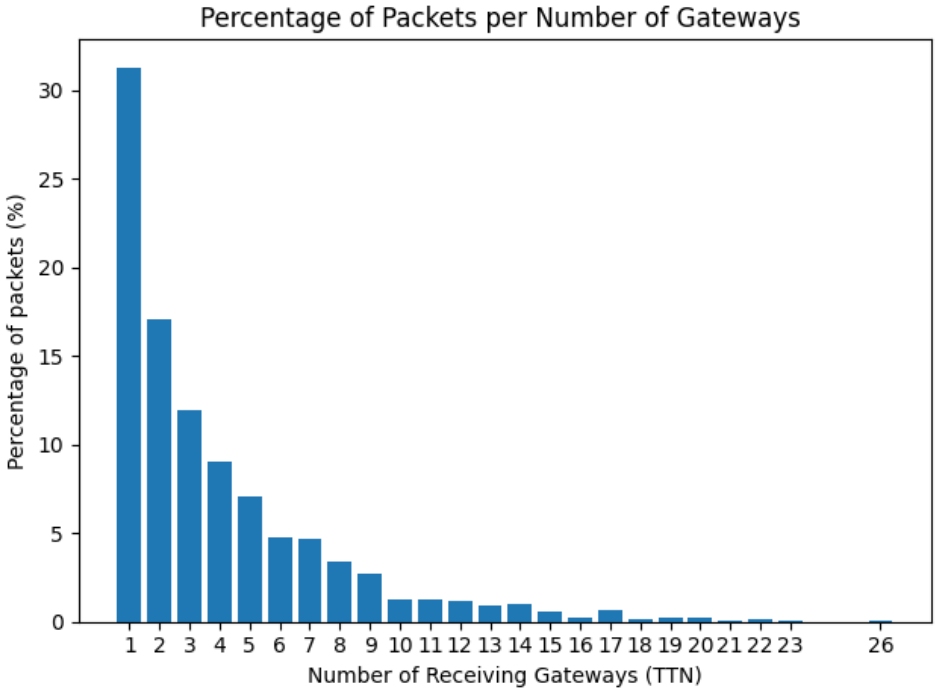

Figure 6.15: Percentage distribution of packets with respect to the number of TTN gateways that received them simultaneously. Most packets were collected by a single gateway, while up to 26 gateways occasionally received the same packet.

6.3.3 Raw Data Analysis

As shown in the figures below, the radiosondes followed different flight paths after the launch at 10:20. In the first part of the flight, most sondes moved to the northwest, then gradually turned east and later to the southeast, as visible in Figure 6.16. From this stage, two main behaviours could be observed. Most sondes turned back and finally landed some

kilometres northeast of the launch site, while others continued travelling farther across central Italy, with the last data packets transmitted from Tuscany (Figures 6.17 and 6.18).

The first two sondes in the legend (tx-01 and tx-02) were those that transmitted only through P2P and private LoraWAN gateway. For this reason, their trajectories stop earlier.

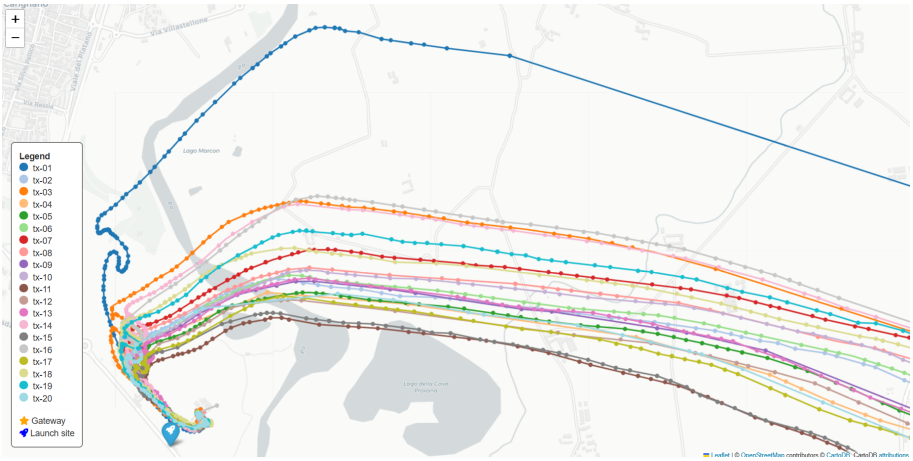

Figure 6.16: Zoomed view of the first flight hours near the launch site (Carmagnola, TO). The sondes initially moved northwest, then gradually turned east and southeast.

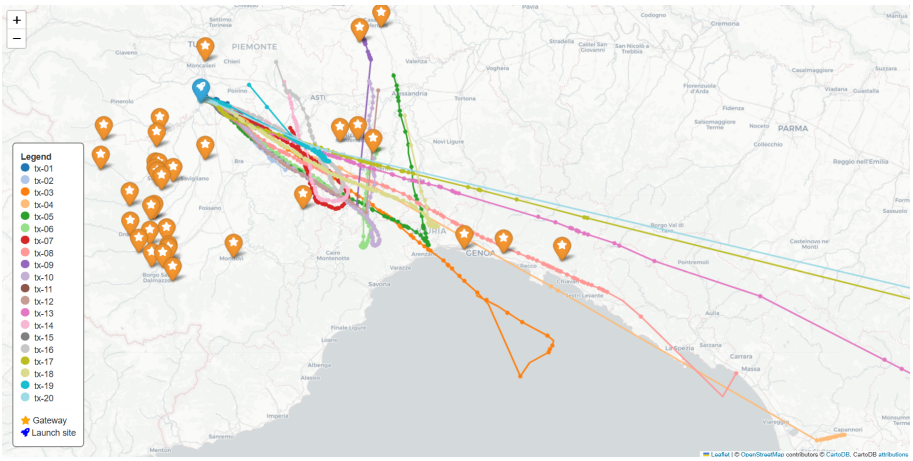

Figure 6.17: Extended view of the trajectories showing the two main behaviours: sondes turning back and landing north-east of the launch site, and sondes continuing towards central Italy. The sonde that landed in the Ligurian Sea (tx-03) is also visible. The dense distribution of TTN gateways in Piemonte is evident.

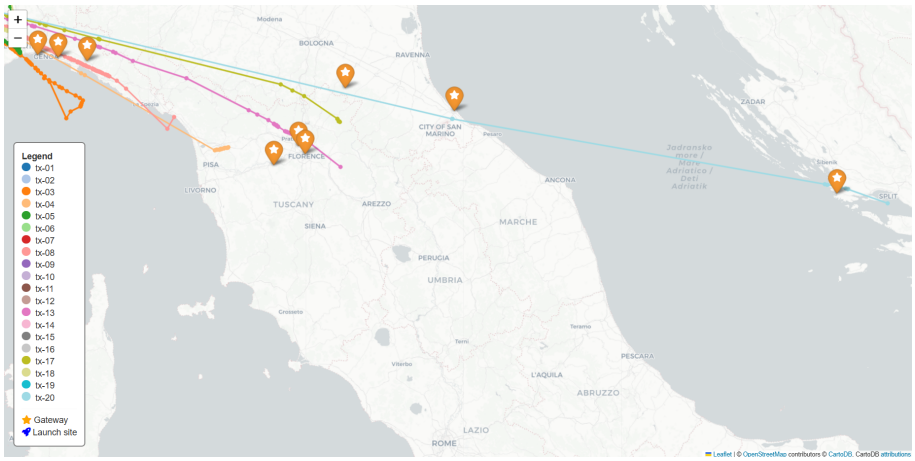

Figure 6.18: Wider view of central Italy and the Adriatic coast, showing sondes travelling further, including the one that reached Croatia (tx-20). The figure highlights the lower density of TTN gateways in central Italy compared to northern regions.

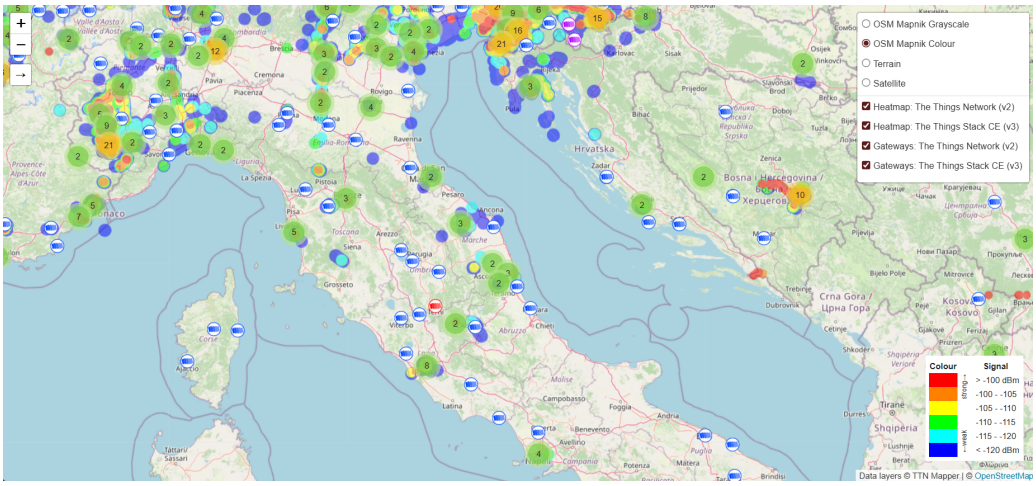

Figure 6.19: TTN coverage heatmap showing differences in the distribution of gateways across Italy.

In particular, two sondes undertook an unusual trajectory: TX-03 crossed the Ligurian Apennines flying over the Ligurian Sea; TX-20 continued towards Central Italy and, instead of concluding its flight there, went on towards the east, crossing the entire Adriatic Sea until reaching the coasts of Split (Croatia). The variety observed in the trajectories is a clear demonstration of how turbulent dispersion can influence the movement of atmospheric particles: even starting from the same point, they are transported by different turbulent structures, moving away significantly.

The trend of altitude over time, reported in Figures 6.20a and 6.20b, can give us further details on the trajectories. The 5 sondes that reached the highest altitudes, namely TX-04, TX-08, TX-13, TX-17, and TX-20, are those that continued in a southeast direction and maintained an almost constant altitude along the path. It can also be observed that each of these sondes transmitted the last data packet while still at altitude, which suggests that their data transmission ended because of battery depletion. Finally, it should be noted that TX-03 followed a similar pattern, but probably due to maritime air currents, ended with a sea landing.

Figure 6.20b shows a zoom of the altitudes in the first two hours of flight: most sondes stabilized at a floating equilibrium altitude, while TX-11 and TX-15 were damaged after just over one hour, leading to a sudden descent and loss of communication.

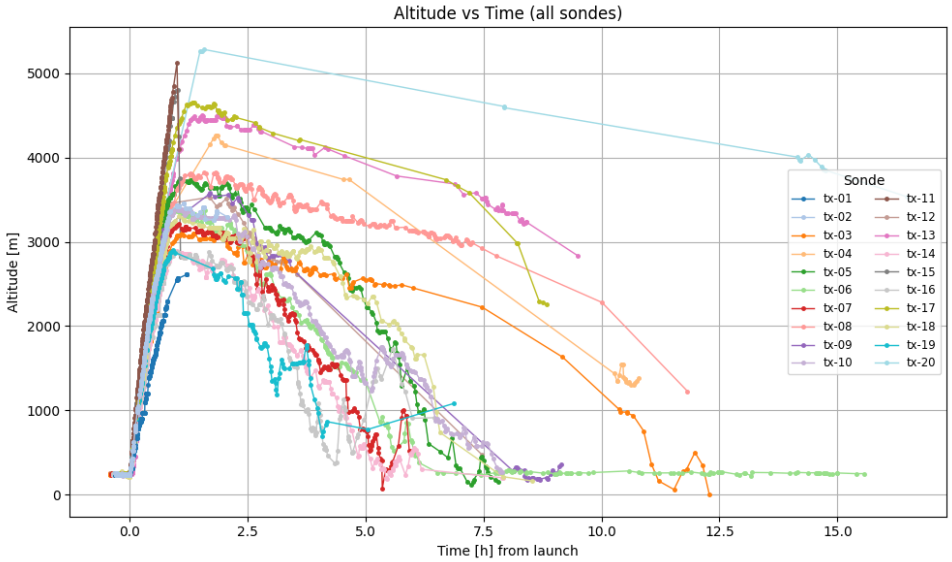

(a)

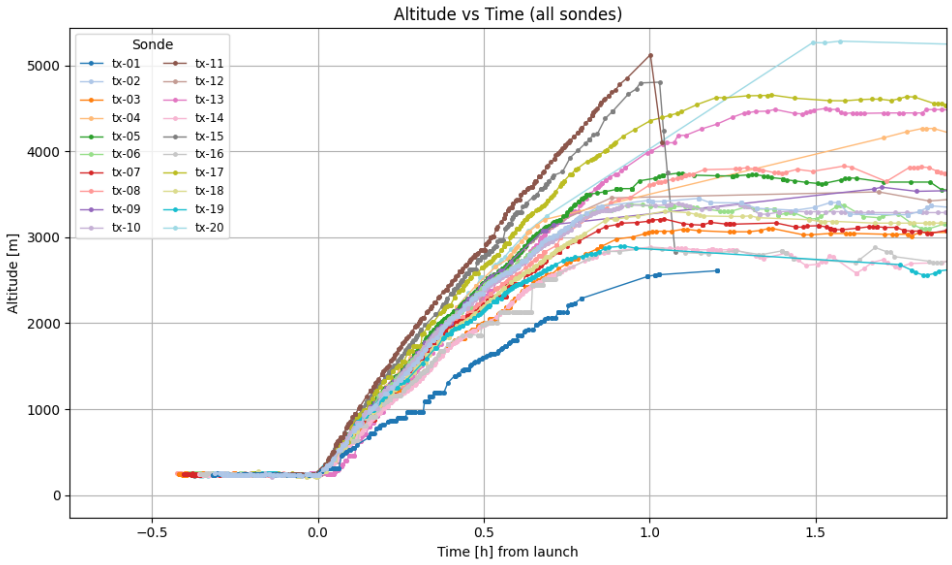

(b)

Figure 6.20: (a) Altitude profiles of all sondes during the 22 July 2025 cluster launch, showing the difference in transmission duration between sondes that reached higher equilibrium levels and those that remained lower. (b) Detail of the first two hours of flight, highlighting sondes stabilizing at floating altitude and the premature failures of tx-11 and tx-15.

Another particular case is the sonde TX-06, which, despite landing after only 7 hours, continued transmitting for much longer. It probably landed in an area with excellent TTN coverage without being damaged, and it was able to send a total of 511 data packets, corresponding to more than 16 hours of continuous transmission.

From both the trajectory maps and the altitude plots it is clear that data reception was

dense and continuous while the sondes remained over Piemonte, but became sparse once they moved southeast and farther away. This highlights the lack of TTN receiving stations in central Italy (Figures 6.17, 6.18 and 6.19), underlining one of the main limitations of this year's data transmission setup: the dependence on the geographical distribution of the public TTN gateways.

Figures 6.21a, 6.21b and 6.21c show the pressure, humidity, and temperature profiles during flight and after landing. Data points recorded before time zero should be regarded as invalid, since the sondes were being handled by the launch personnel.

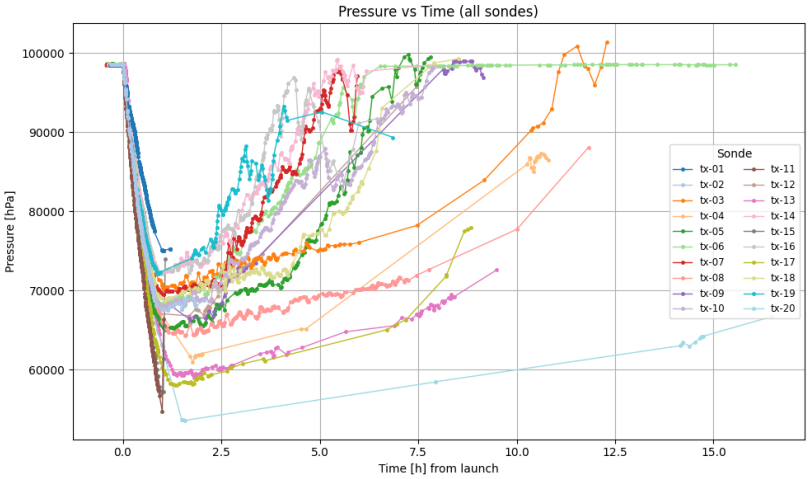

(a)

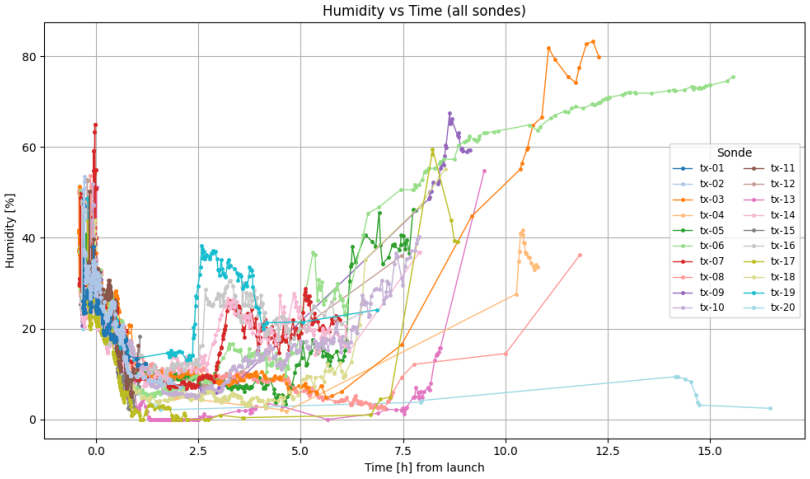

(b)

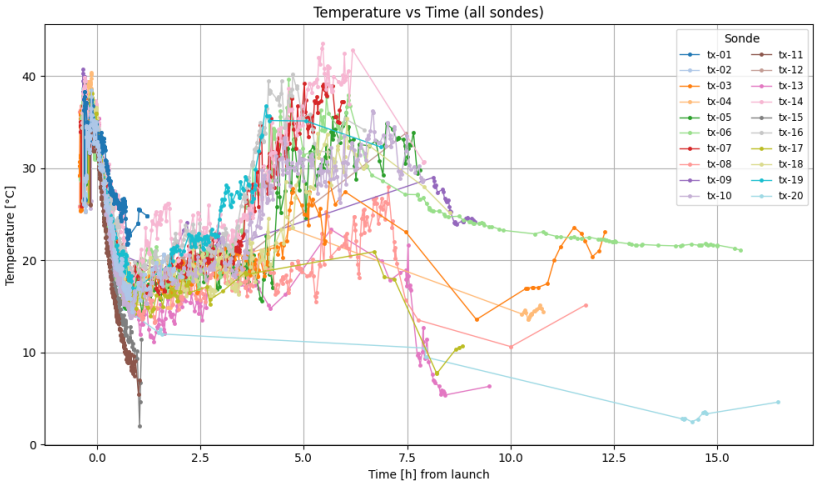

(c)

Figure 6.21: (a) Pressure profiles; (b) Humidity profiles; (c) Temperature profiles of all sondes during flight and after landing.

The pressure profiles follow the expected decrease with altitude and are consistent with the standard pressure gradient, confirming the reliability of the sensors.

The humidity and temperature profiles show oscillations with altitude, caused by transitions between air masses of different humidity and temperature, together with the

influence of turbulent structures that locally affect the sondes' paths. Relative humidity generally remained below 80%, confirming that the sondes did not enter cloud layers; the only exception is tx-03, which exceeded this threshold during the final stage of flight as it landed in the sea.

While the velocity profiles will be addressed in the next section, which is more specifically dedicated to turbulent characteristics, for now we focus on the behavior of the accelerations and of the magnetic field recorded by the inertial unit.

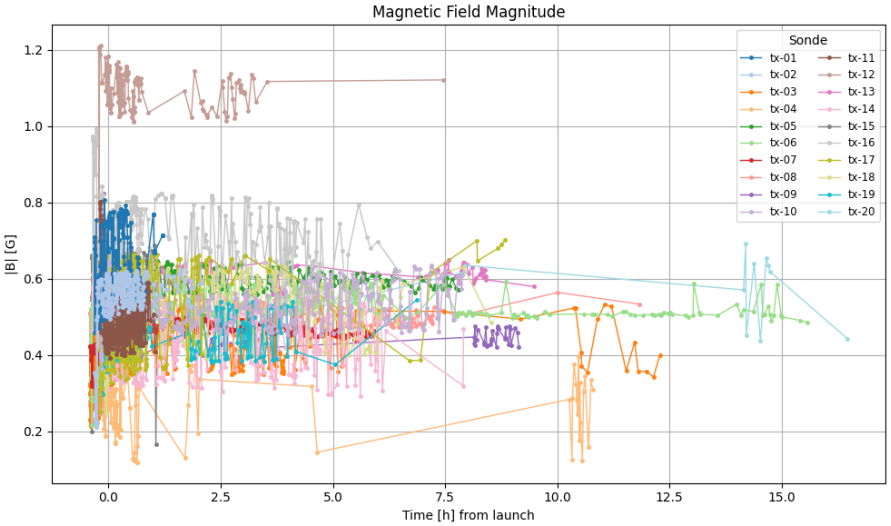

Figure 6.22: Magnetic field recorded by the sondes. Bias errors are evident from the offset of mean values outside the expected geomagnetic field range.

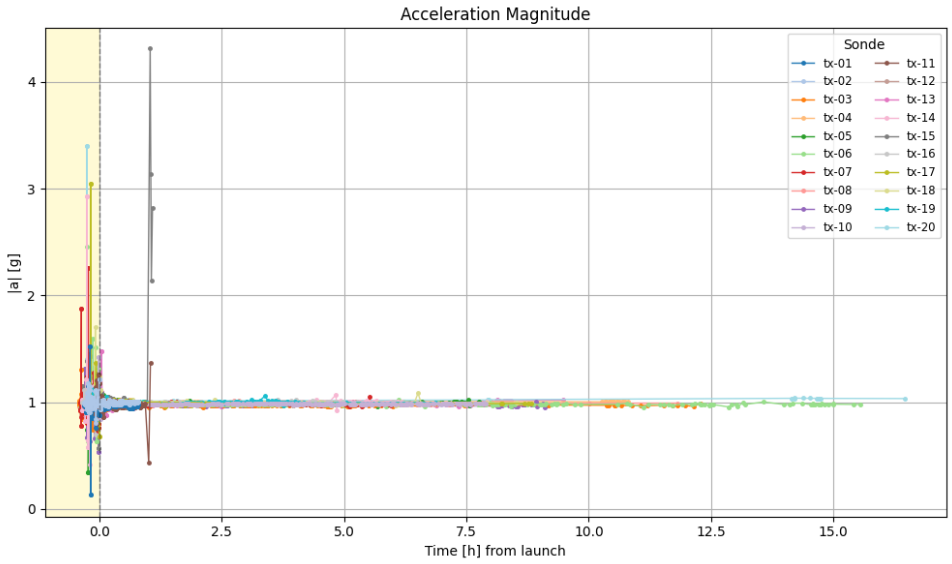

(a)

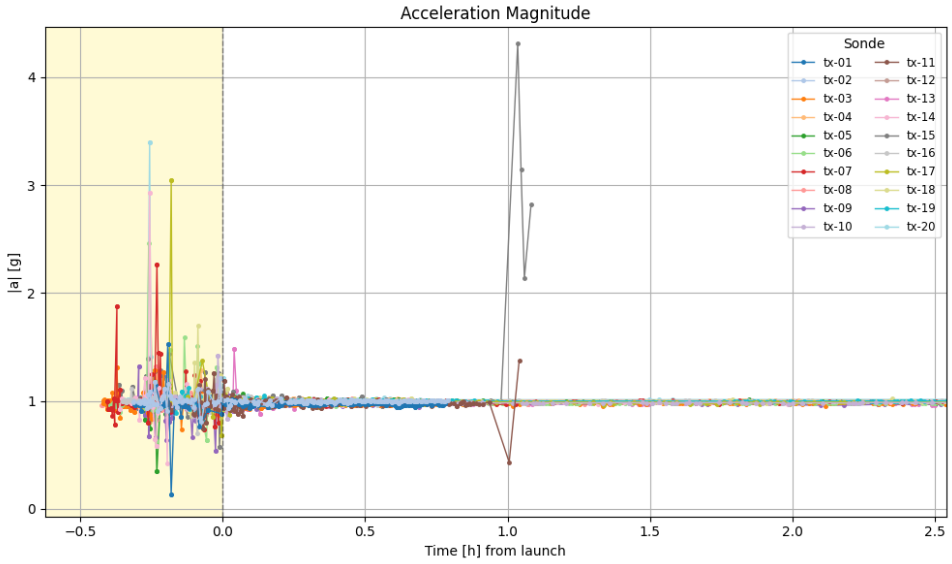

(b)

Figure 6.23: (a) Acceleration magnitude during the flights, with values close to 1 g reflecting gravity and strong peaks corresponding to sondes damaged in flight. (b) Zoom of the period before launch (yellow background), showing stronger oscillations due to handling by the launch team, and the smaller oscillations appearing just after release

Regarding the magnetic field, Figure 6.22 shows that the main problem is the missing correct calibration of the magnetometers. The sensors record fluctuations, but their mean values are often shifted outside the expected range of the Earth's field in this region ($\approx$ 0.45–0.5 G, from Northern Italy to Croatia). One probe is even more displaced, with mean values close to 1 G, which confirms that calibration errors are the main reason rather than real changes in the geomagnetic field.

Acceleration, on the other hand, looks reliable: as shown in Figures 6.23a and 6.23b, the acceleration magnitude stays close to 1 g for most of the flights, as expected from the gravity force. The zoom in Figure 6.23b shows stronger oscillations before the launch (yellow background), caused by handling of the sondes by the launch team. Just after

balloon release, smaller oscillations (generally <0.2 g) appear, most likely due to the mechanical response of the sonde–balloon system (pendulum motion and tether vibrations) rather than to atmospheric turbulence, since ARPA reported almost calm winds at low altitude that day. The only strong peaks happened about one hour after launch for sondes tx-11 and tx-15, which were probably damaged in flight; in particular, tx-11 reached more than 4 g, consistent with a sudden impact or structural failure.

6.3.4 Post-processing: Turbulent characteristics and diffusion

From the collected data, and remembering that the original purpose of radiosondes is to study the atmospheric turbolence, some post-processing was carried out to highlight turbulent characteristics of the flows encountered by the sondes.

Spectral analysis

The spectral analysis focused on the wind speed magnitude and on its three velocity components in the NED (North–East–Down) frame. Three sondes (tx-05, tx-10, tx-14) were selected as representative cases for both the total wind speed spectra (Figure 6.24) and the components spectra (Figure 6.25)

The original data were received at irregular times, so resampling was necessary. The signals were linearly interpolated at regular 42 s intervals, corresponding to the median packet spacing observed from the gateways. This sets the Nyquist frequency according to

$$f_N = \frac{1}{2\,\Delta t} = \frac{1}{2 \times 42\,\mathrm{s}} \approx 0.012\,\mathrm{Hz},$$

which limits the high-frequency end of the spectra. After resampling, the Fast Fourier Transform (FFT) was applied to obtain the spectra. The plots are shown in log–log scale, with the Kolmogorov $-5/3$ slope added for comparison.

The spectra of both the total wind speed and the three components show a general agreement with the $-5/3$ law, although the noisy nature of the dataset makes the identification of an inertial range less clear. At very low frequencies (10^{-3}–10^{-4} Hz), a flattening of the spectra would normally be expected, since this range belongs more to the energy-production scales than to the inertial subrange (see, e.g., Stull 1988 [51]). In our case, however, such flattening is not clearly visible, which may be related to the fact that the atmosphere is far from isotropic and homogeneous.

A lack of agreement is especially marked in the vertical component V_{up} (Figure 6.25f), whose spectrum deviates completely from the $-5/3$ slope. The curve shows a steeper decay at low frequencies and a flatter trend at higher ones, which can plausibly be explained by the strong vertical anisotropy induced by atmospheric stratification together with the influence of balloon buoyancy on the vertical motion.

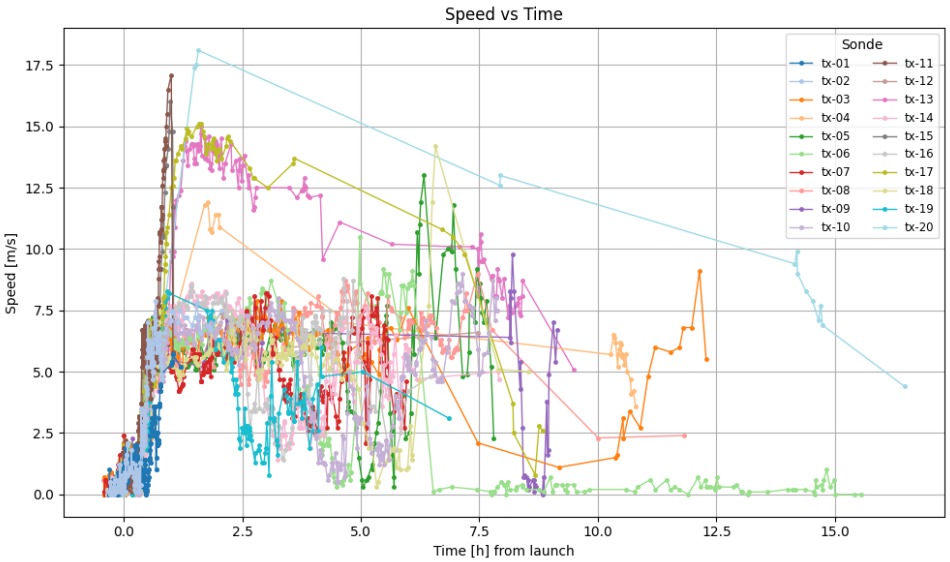

(a)

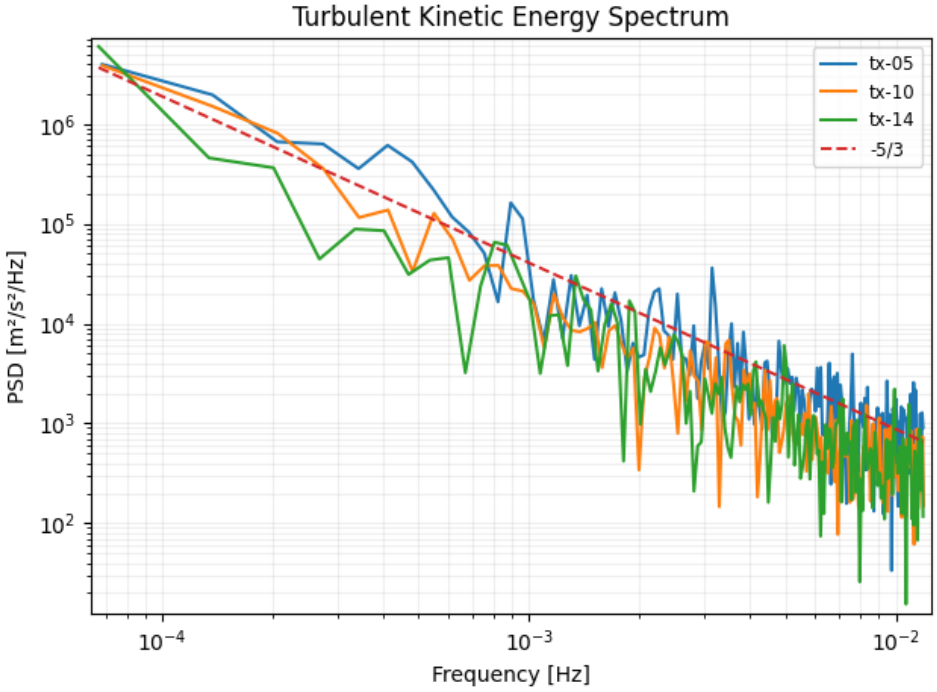

(b)

Figure 6.24: (a) Wind speed profiles of all sondes, where higher-altitude sondes reached larger velocities; (b) power spectral density of wind speed, representative of turbulent kinetic energy, for the three selected sondes (tx-05, tx-10, tx-14), in approximate agreement with the $-5/3$ Kolmogorov slope but without evident flattening at low frequencies.

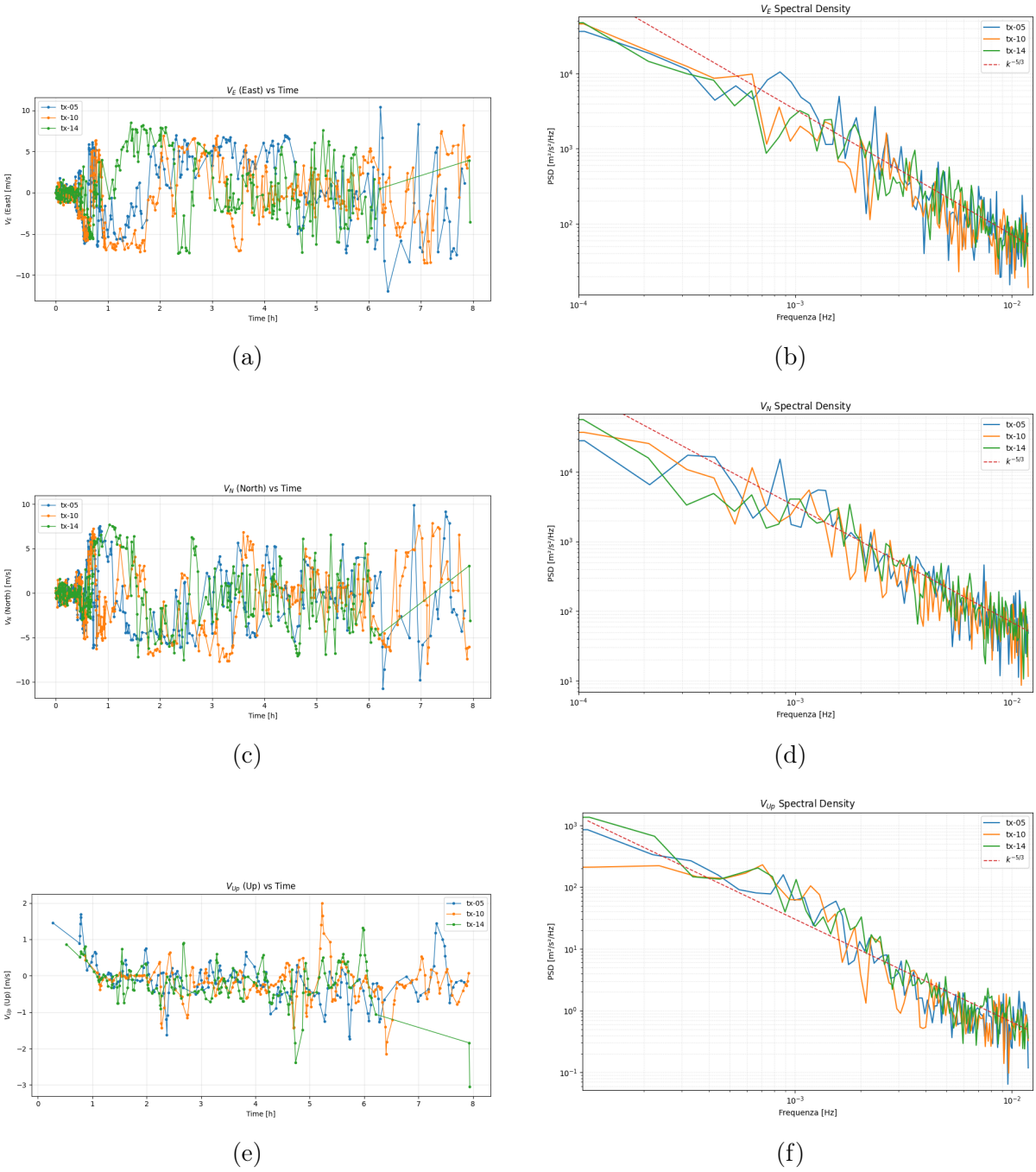

Figure 6.25: Velocity components in the NED frame and corresponding spectra for the three selected sondes: (a, c, e) time series of V_E, V_N, and V_{up}; (b, d, f) power spectral densities compared with the $-5/3$ Kolmogorov slope. The horizontal components (V_E, V_N) display approximate agreement, while the vertical component V_{up} deviates strongly, with a steeper decay at low frequencies and a flatter trend at higher ones.

The spectral analysis was also extended to temperature and humidity for the same three sondes (tx-05, tx-10, tx-14; Figure 6.26). Both variables display spectra that align reasonably well with the $-5/3$ law, similar to the wind speed results. As in the velocity case, no flattening is visible at very low frequencies (10^{-3}–10^{-4} Hz),

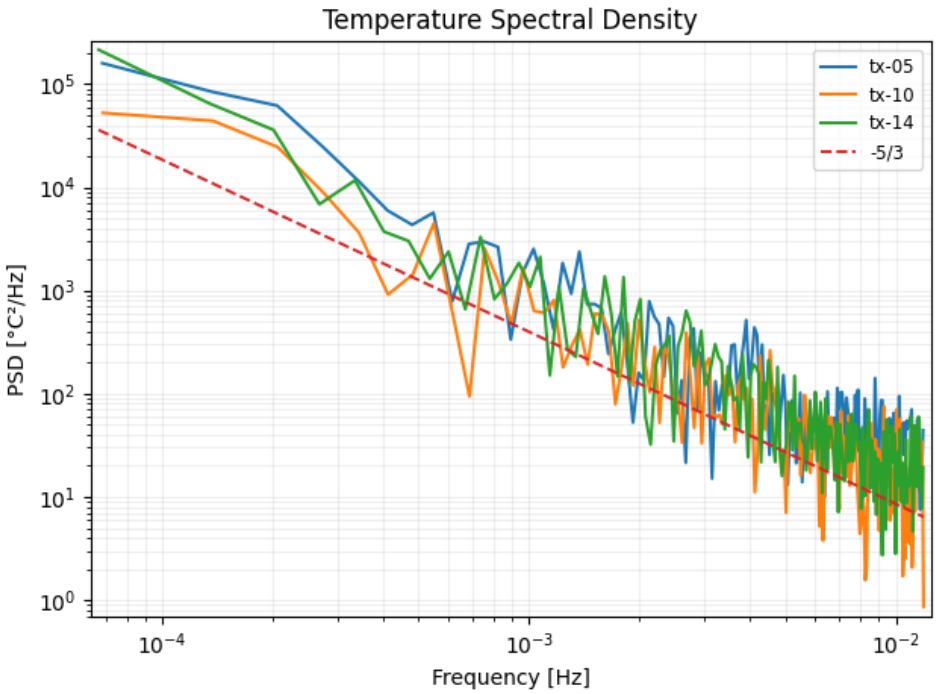

(a)

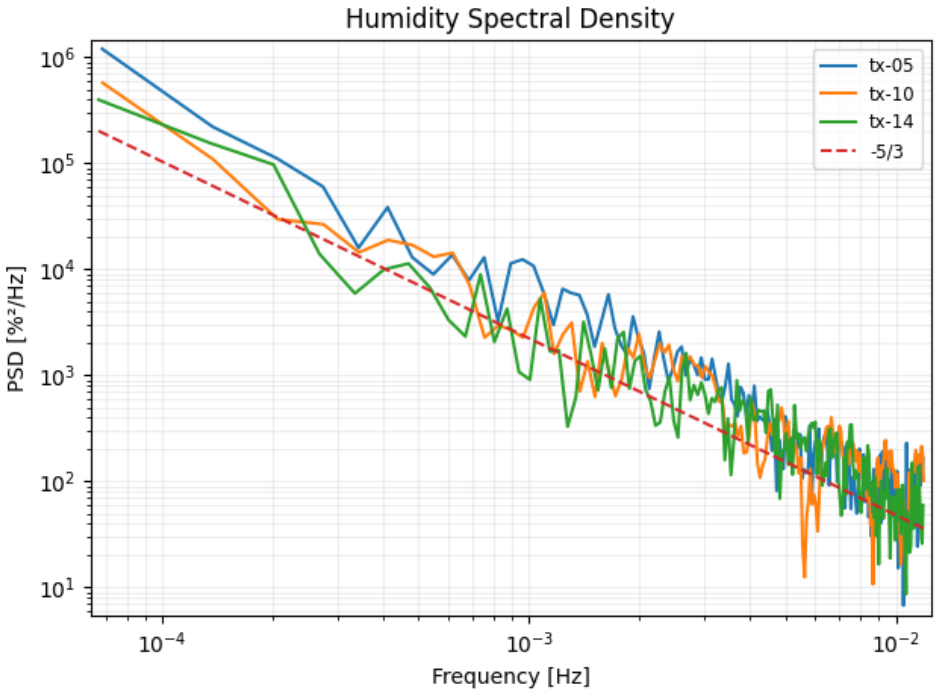

(b)

Figure 6.26: Power spectral densities of temperature and relative humidity for the three selected sondes (tx-05, tx-10, tx-14), showing approximate agreement with the $-5/3$ Kolmogorov slope.

Energy dissipation rate estimation

An important parameter in the study of turbulent flows, which can be estimated from kinetic energy spectra at least in a preliminary way, is the mean turbulent energy dissipation rate (ε). We briefly introduced this concept in Chapter 1.

According to the classical K41 theory, which relies on the assumptions of stationarity, homogeneity, and isotropy, the one-dimensional energy spectrum within the inertial subrange follows the Kolmogorov $-5/3$ scaling law:

$$F(k) = \alpha\, \varepsilon^{2/3}\, k^{-5/3}$$

where $F(k)$ is the one-dimensional spectrum as a function of the wavenumber k, ε the mean dissipation rate, and α the Kolmogorov constant (≈ 0.5 for the streamwise velocity component).

As described by Batchelor [52], this formulation can be transferred into the frequency domain using Taylor's frozen turbulence hypothesis, which assumes that fluctuations are advected by the mean wind speed U, so that $k = 2\pi f/U$. This leads to the following expression for the power spectral density $S(f)$:

$$S(f) = \alpha\, \varepsilon^{2/3} \left(\frac{U}{2\pi}\right) f^{-5/3}$$

where $S(f)$ is the power spectral density, f the frequency, and U the mean wind speed. From this relationship, the dissipation rate can be estimated as:

$$\varepsilon = \left(\frac{2\pi U}{\alpha}\right) \left(f^{5/3} S(f)\right)^{3/2}$$

Before discussing the results, it is important to acknowledge the limitations of applying these relations to our data. The assumptions of K41 theory (stationarity, homogeneity and isotropy) cannot be verified with the available measurements, and the atmospheric conditions during the flights are likely far from such constraints. In addition, the temporal resolution of the dataset restricts access to the highest frequencies, so that the inertial subrange is only partially resolved. Finally, the meaning of the averaged dissipation rate $\bar{\varepsilon}$ is weaker than in ideal homogeneous isotropic turbulence, since in our case ε varies considerably along the sondes' trajectories, both in terms of fluctuations and mean values.

Despite these limitations, the Kolmogorov framework is here adopted as a preliminary tool to estimate the order of magnitude of the dissipation rate. Future studies should aim at extending the resolvable frequency range and at accounting for anisotropy effects more explicitly.

An additional important remark is that the horizontal wind speed was chosen as the reference velocity, since the sondes predominantly follow the horizontal flow. In particular, the streamwise velocity was defined as:

$$U_h = \sqrt{V_E^2 + V_N^2},$$

which was adopted both for the spectral analysis and, from the spectra, for the estimation of the energy dissipation rate.

With these considerations, we can now look at the results for the three selected sondes, shown in Figures 6.27 and 6.28 below.

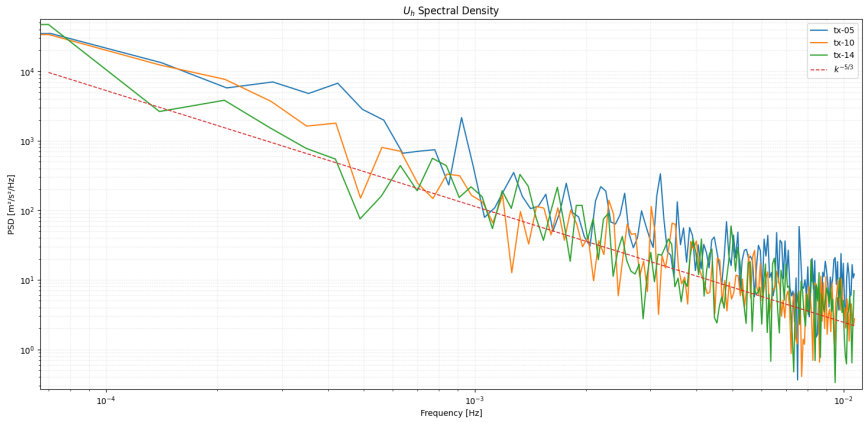

Figure 6.27: Horizontal wind speed spectra of the three selected sondes (tx-05, tx-10, tx-14), computed from the NED components V_N and V_E, and used for the estimation of the turbulent energy dissipation rate.

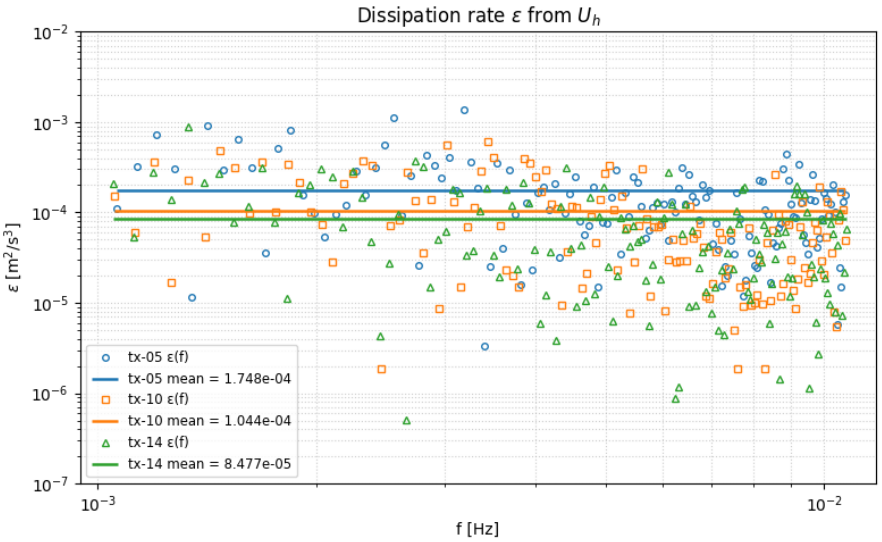

Figure 6.28: Energy dissipation rate estimates for the three selected sondes (tx-05, tx-10, tx-14). Continuous lines indicate mean values computed for frequencies $f > 10^{-3}$ Hz, while individual points represent estimates at each frequency. The average dissipation rates range from 8.5×10^{-5} to 1.75×10^{-4} m^2/s^3.

It can be seen that not the whole frequency range over which the spectrum was calculated (see Figure 6.27) is represented in Figure 6.28. This is because, in this analysis, only frequencies higher than 10^{-3} Hz were taken into account. This threshold was chosen because it better represents the inertial subrange described in the literature and avoids including very low frequencies, which are dominated by large-scale motions and are less useful for estimating dissipation.

In Figure 6.28, the dashed lines show the mean dissipation values calculated by integrating over the chosen frequency range, while the points represent the dissipation rate estimated at each single frequency. The average values obtained are between 8.5×10^{-5} and 1.75×10^{-4} m^2/s^3.

These estimates are consistent with typical values reported for the atmospheric boundary layer, usually between 10^{-6} and 10^{-2} m^2/s^3 (see, e.g., O'Connor et al. 2010 [53]).

Turbulent diffusion

Following the classical framework of Richardson (1926) for turbulent dispersion, the relative motion of a cluster of particles can be analyzed using the probability distribution of their separation distances. For this purpose, we adopt the Distance–Neighbor Graph function (Q), already introduced in Chapter 1.

The DNG describes the average number of neighboring particles found within successive distance intervals. Radiosondes, acting as "marked particles," are well suited for this analysis, as they rise to a given altitude and then drift passively with the flow. Each element $Q_{n,n+1}$ represents the average number of probes located between distances $n \cdot h$ and $(n+1) \cdot h$ from a reference probe, where h is the chosen neighborhood size. Formally:

$$Q_{n,n+1} = \frac{1}{N} \left(P^1_{n,n+1} + P^2_{n,n+1} + \cdots + P^N_{n,n+1} \right)$$

where N is the total number of sondes and $P^k_{n,n+1}$ the number of neighbors of the k-th sonde in the bin $[n \cdot h, (n+1) \cdot h]$. To compute P^k, we evaluate the separation distances between each sonde and all the others $(N-1)$, then build histograms over the distance bins.

Q is a probability distribution dependent on space and time; thus, choosing the bin size h and the time interval Δt between curves effectively means selecting which turbulent scales to consider. In this study, two cases were analyzed:

1. Small-scale analysis: only the first 15 minutes after launch are considered, with $\Delta t = 3$ min and $h = 30$ m.

2. Larger-scale analysis: the sondes' behavior is observed over the first hour of flight, just before the number of active sondes decreased due to in-flight failures, using $\Delta t = 15$ min and $h = 800$ m.

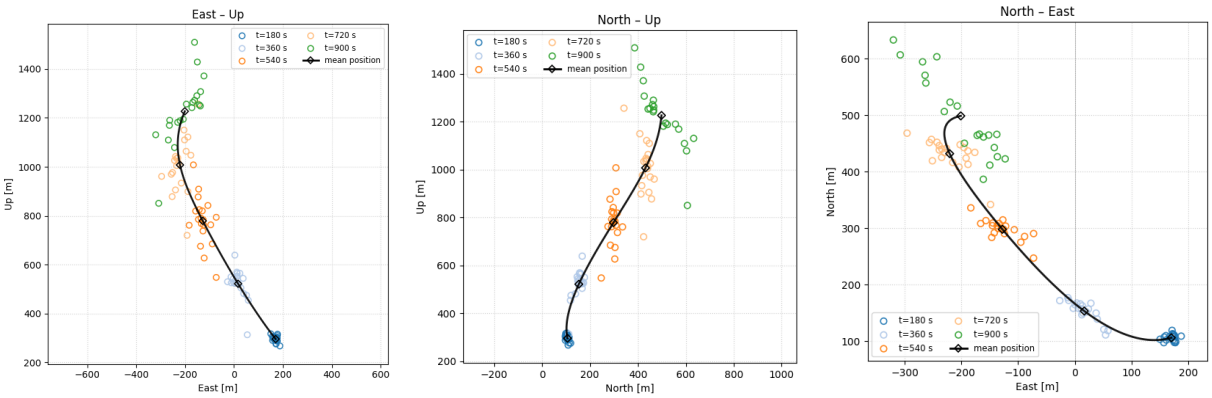

(a) (b) (c)

Figure 6.29: Small-scale cluster evolution (first 15 minutes) in the planes: (a) east–up, (b) north–up, (c) north–east. Each color corresponds to a distinct time; black markers show the mean cluster position.

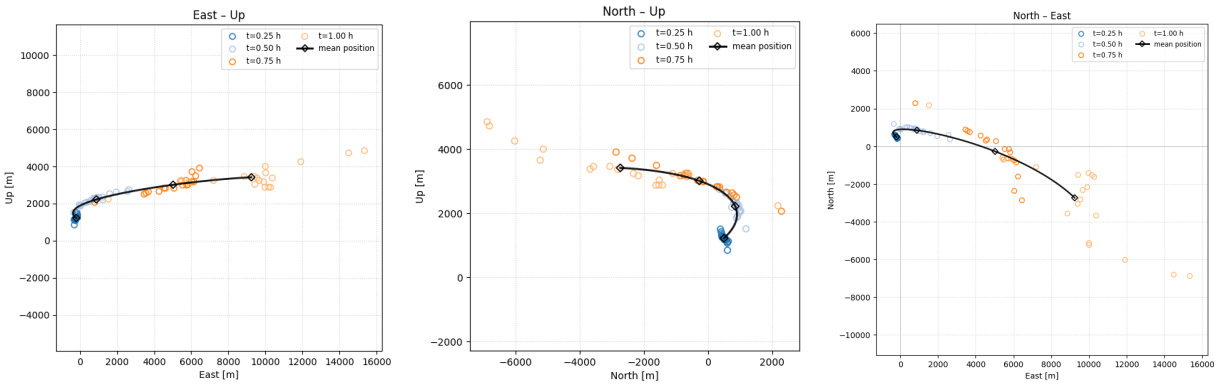

(a) (b) (c)

Figure 6.30: Larger-scale cluster evolution (first 60 minutes) in the planes: (a) east–up, (b) north–up, (c) north–east. Each color corresponds to a distinct time; black markers show the mean cluster position.

From these figures, it is clear that the mutual separation between sondes increases steadily with time. Notably, when extending the observation window from 15 minutes (Figure 6.29) to 60 minutes (Figure 6.30), the maximum horizontal distance from the launch site increases from about 0.7 km to 17.5 km, showing a much faster growth than the time scale itself. This illustrates that turbulent diffusion is inherently a large-scale process: the longer the time interval considered, the more the larger turbulent eddies contribute to amplifying the dispersion of the sondes.

Once the sondes' positions at different time instants were obtained, the analysis could proceed with the calculation of the Distance–Neighbor Graphs (DNG). Figures 6.31 and 6.32 present the results for the two time scales considered.

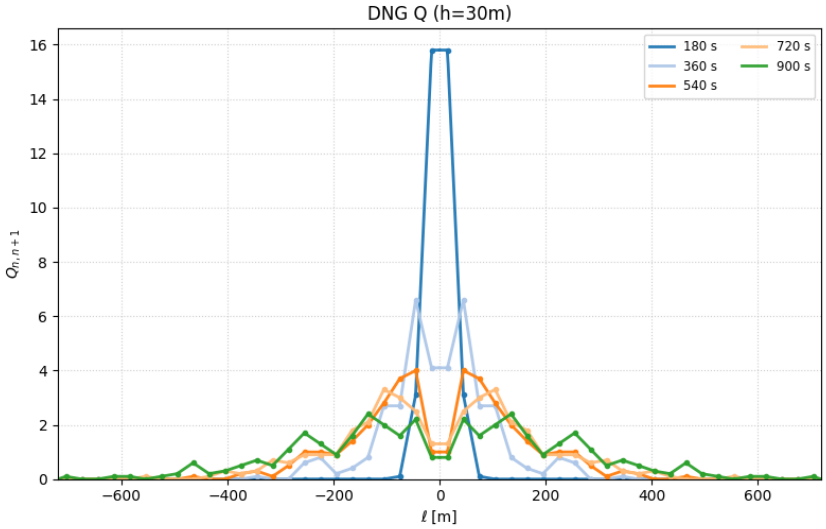

Figure 6.31: Distance–Neighbor Graph (DNG) for the small-scale case ($\Delta t = 5$ min, $h = 30$ m).

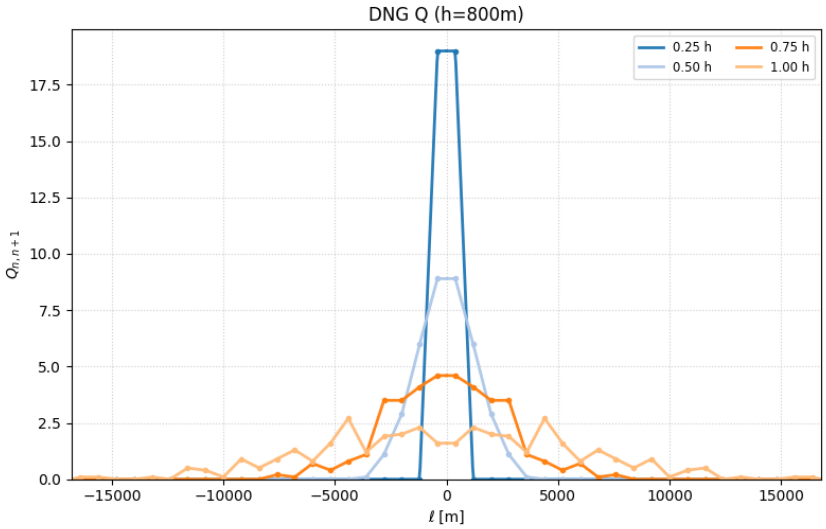

Figure 6.32: Distance–Neighbor Graph (DNG) for the larger-scale case ($\Delta t = 15$ min, $h = 800$ m).

The choice of the neighborhood size h is somewhat arbitrary and represents a compromise: it should be small enough to resolve the fine structure of the flow, but large enough to ensure that each interval contains a statistically significant number of probes. In this study, an interval of $h = 30$ m was adopted for the small-scale case (Figure 6.31), while a much larger interval of $h = 800$ m was selected for the large-scale case (Figure 6.32).

These figures, in both cases analyzed, represent well the characteristics of the turbulent dispersion of the radiosonde cluster: at the beginning of the flight, most sondes are concentrated within the first distance interval, but as time progresses, the peaks of the distributions move away from each other and the overall width of the DNG increases, a sign that the cluster is observing larger separation distances.

Conclusions

Rereading the chapters as a chronological sequence, it clearly emerges that the H2020-COMPLETE project, which has now become HOUSEFLIES, has been a continuously evolving process. Within this framework, the present thesis aims to document the contribution made to two of the most significant advances of the past year.

The first contribution concerns the design and realization of a double-wheel thermal sealer dedicated to the production of Mater-Bi balloons. Although, at first sight, they may appear as a secondary component, in reality these aerostatic balloons play a fundamental role for the radiosonde: to ensure the tracking of fluid-dynamic quantities along Lagrangian trajectories, it is essential to have a balloon that is lightweight, as spherical as possible and, given the disposable nature of the radiosonde system, also biodegradable. In other words, "how passively" the sensors follow the turbulent motion, simulating the behavior of a particle in the flow, largely depends on the properties of the balloon. From here derives the choice to intervene on the production process to make it more reliable and repeatable, and at the same time adaptable to different geometries in order to tend more and more to the ideal sphere. After an initial phase of conceptualization and design, with the sizing of the compression system, it was possible to build the prototype and start the first welding tests. Numerous laboratory tests on Mater-Bi samples made it possible to identify the optimal parameters (pressure, temperature, speed), which were subsequently applied in the construction of full-scale balloons. A first verification phase included helium retention tests, and the results on gas leakage were encouraging, while still indicating margins of improvement with the potential reduction of the number of welds. Another way pursued to test the quality of the welds was in the field, using a launch of two tethered sondes to observe the behavior of the balloons subjected to environmental turbulent phenomena while carrying sondes with a configuration very similar to that planned for cluster launches. In this case, the environment to which the balloons were exposed was certainly not the most favorable, with the presence of strong winds and rain for a certain part of the experiment. Despite such conditions and the violent tugging that the tether could generate to keep the balloon anchored to the ground, the balloons performed very well: the welds resisted and the sonde continued to transmit, suspended above the ground, until the end of the test. This is an encouraging result in view of future launches.

The second contribution concerns participation in the organization and execution of two launches, both free-floating but with different characteristics. The first experiment, conducted on 25/06/2025 from the roof of the Politecnico with a single sonde, aimed to validate a new method of data packet communication. Until then, in the HOUSEFLIES project transmission had always taken place in LoRa peer-to-peer mode on private single-channel receivers, but the need to manage larger clusters with greater autonomy and coverage led to the adoption of a LoRaWAN communication protocol on a public network (TTN). Despite the inevitable constraints related to the use of a standardized protocol

(for example the duty cycle), the experiment demonstrated clear advantages in terms of duration and coverage of reception. The positional and environmental data proved to be reliable and, confirming the quality of the measurements, spectral analyses showed consistency with Kolmogorov's law. This success opened the way to a second cluster experiment (22/07/2025), aimed at fully exploiting the potential of the public gateway network. Twenty sondes were employed simultaneously (doubling the historical maximum of the project) and the trajectories covered distances much greater with respect to the previous multi-sonde launches, exploiting completely the autonomy of the batteries. In fact, with the exception of a few isolated results, the sondes transmitted data for at least seven hours, up to a maximum of 16 hours. The spectral analysis again showed slopes consistent with Kolmogorov's theory and made it possible to estimate the mean energy dissipation rate, in line with typical atmospheric values reported in the literature. The large number of transmitting sondes also made it possible to study turbulent dispersion and, in particular, in agreement with Richardson, to observe the behavior of particles on different spatial and temporal scales through the Distance–Neighbor Graph (DNG). These two experiments, which effectively served as validation of the new transmission configuration, nevertheless highlighted some difficulties: the constraints of the duty cycle limit the sampling frequency and, consequently, the range of turbulent scales that can actually be resolved; moreover, the continuity of data reception is influenced by the geographical distribution of TTN gateways. Facing these two problems will be fundamental for the next experimental campaigns.

Overall, the work carried out during this thesis confirmed the feasibility of cluster launches through LoRaWAN communication for quantitative studies of atmospheric turbulence and, at the same time, made the production of Mater-Bi balloons more reliable and efficient. Two complementary results that push HOUSEFLIES towards increasingly numerous and accurate measurements, with expected benefits both in the characterization of turbulent diffusion processes and, more generally, in experimental observations supporting atmospheric modeling.

Bibliography

[1] Richardson, L. F. (2007). *Weather prediction by numerical process* (2nd ed.). Cambridge University Press.

[2] Kolmogorov, A. N. (1941). The local structure of turbulence in incompressible viscous fluids at very large Reynolds numbers. *Doklady Akademii Nauk SSSR*.

[3] Pope, S. B. (2000). *Turbulent flows*. Cambridge University Press.

[4] Kundu, P. K., & Cohen, I. M. (2007). *Fluid mechanics*. Academic Press.

[5] Frisch, U. (1995). *Turbulence: The legacy of A. N. Kolmogorov*. Cambridge University Press.

[6] Zhou, Y. (1993). Interacting scales and energy transfer in isotropic turbulence. *Physics of Fluids A*, 5, 2524–2531.

[7] Monin, A. S., & Yaglom, A. M. (1975). *Statistical fluid mechanics: Mechanics of turbulence* (Vol. 1). MIT Press.

[8] Sreenivasan, K. R., & Antonia, R. A. (1997). The phenomenology of small-scale turbulence. *Annual Review of Fluid Mechanics*, 29, 435–472.

[9] Richardson, L. F. (1925). Atmospheric diffusion shown on a distance-neighbour graph. Cambridge University.

[10] Gioia, G., Lacorata, G., Marques Filho, E. P., Mazzino, A., & Rizza, U. (2004). Richardson's law in large-eddy simulations of boundary-layer flows. *Boundary-Layer Meteorology*, 113, 187–199. https://doi.org/10.1023/B:BOUN.0000039373.45669.68

[11] Elliott, F. W., Jr., & Majda, A. J. (1996). Vorticity and turbulence dynamics. *Physics of Fluids*, 8, 1052–1060.

[12] Fung, J. C. H., & Vassilicos, J. C. (1998). Two-particle dispersion in turbulent-like flows. *Physical Review E*, 57, 1677–1690.

[13] Monin, A., & Yaglom, A. (1975). *Statistical fluid mechanics* (Vol. 2). MIT Press.

[14] Boffetta, G., & Sokolov, I. M. (2002). Relative dispersion in fully developed turbulence: The Richardson's law and intermittency corrections. *Physical Review Letters*, 88, 094501.

[15] Wallace, J. M., & Hobbs, P. V. (2006). *Atmospheric science: An introductory survey* (2nd ed.). Academic Press.

[16] Garratt, J. R. (1992). *The atmospheric boundary layer*. Cambridge University Press.

[17] INFLIBNET Centre. (n.d.). *Atmospheric boundary layer*. In *Environmental Science* (Chapter 8). Retrieved April 23, 2025, from `https://ebooks.inflibnet.ac.in/esp08/chapter/8-atmospheric-boundary-layer/`

[18] Honnert, R., Efstathiou, G. A., Beare, R. J., Ito, J., Lock, A., Neggers, R., Plant, R. S., Shin, H. H., Tomassini, L., & Zhou, B. (2020). The atmospheric boundary layer and the "gray zone" of turbulence: A critical review. *Journal of Geophysical Research: Atmospheres*, 125, e2020JD030317.

[19] Dimotakis, P. E. (2005). Turbulent mixing. *Annual Review of Fluid Mechanics*, 37, 329–356.

[20] Kaimal, J. C., & Finnigan, J. J. (1994). *Atmospheric boundary layer flows: Their structure and measurement*. Oxford University Press.

[21] Hamblyn, R. (2022). Luke Howard, namer of clouds. *Weather*, 77(11), 376–379.

[22] ISCCP. (2022). Cloud climatology: Net effect on energy and water balances. International Satellite Cloud Climatology Program (NASA). Retrieved from `https://isccp.giss.nasa.gov/role.html`

[23] Lamb, D., & Verlinde, J. (2011). *Physics and chemistry of clouds*. Cambridge University Press.

[24] Pruppacher, H., & Klett, J. (2010). *Microphysics of clouds and precipitation*. Springer.

[25] Warner, J. (1969). The microstructure of cumulus cloud. Part I. General features of the droplet spectrum. *Journal of the Atmospheric Sciences*, 26, 1049–1059.

[26] Jonas, P. R. (1996). Turbulence and cloud microphysics. *Atmospheric Research*, 40(2), 283–306.

[27] Bodenschatz, E., Malinowski, S., Shaw, R., & Stratmann, F. (2010). Can we understand clouds without turbulence? *Science*, 327(5968), 970–971.

[28] Grabowski, W. W., & Wang, L.-P. (2013). Growth of cloud droplets in a turbulent environment. *Annual Review of Fluid Mechanics*, 45, 293–324.

[29] Vaillancourt, P. A., Yau, M. K., Bartello, P., & Grabowski, W. W. (2002). Microscopic approach to cloud droplet growth by condensation. Part II: Turbulence, clustering, and condensational growth. *Journal of the Atmospheric Sciences*, 59(24), 3421–3435.

[30] Maxey, M. R., & Riley, J. J. (1983). Equation of motion for a small rigid sphere in a nonuniform flow. *Physics of Fluids*, 26, 883–889.

[31] Lehmann, K., Siebert, H., & Shaw, R. A. (2009). Homogeneous and inhomogeneous mixing in cumulus clouds: Dependence on local turbulence structure. *Journal of the Atmospheric Sciences*, 66(12), 3641–3659.

[32] Pinsky, M., & Khain, A. (1996). Theoretical analysis of the entrainment mixing process at cloud boundaries. Part II: Motion of cloud interface. *Journal of the Atmospheric Sciences*.

[33] Brenguier, J.-L., & Grabowski, W. W. (1993). Cumulus entrainment and cloud droplet spectra: A numerical model within a two-dimensional dynamical framework. *Journal of the Atmospheric Sciences*, 50(1), 120–136.

[34] Stevens, B., & Bony, S. (2013). What are climate models missing? *Science*, 340(6136), 1053–1054. https://doi.org/10.1126/science.1237554

[35] Fossà, L., Abdunabiev, S., Golshan, M., & Tordella, D. (2022). Microphysical timescales and local supersaturation balance at a warm cloud top boundary. *Physics of Fluids*, 34(6), 067103. https://doi.org/10.1063/5.0090664

[36] Hentgen, L., Ban, N., Kröner, N., Leutwyler, D., & Schär, C. (2019). Clouds in convection-resolving climate simulations over Europe. *Journal of Geophysical Research: Atmospheres*, 124(7), 3849–3870. https://doi.org/10.1029/2018JD030150

[37] CORDIS, European Commission. (2022). Cloud-microphysics-turbulence-telemetry: An interdisciplinary training network for enhancing the understanding and modeling of atmospheric clouds (COMPLETE Project H2020). Retrieved from `https://cordis.europa.eu/project/id/675675`

[38] NOAA, Air Resources Laboratory. (2022). Low altitude balloon measurement platforms. Retrieved from `https://www.arl.noaa.gov/wp_arl/wp-content/uploads/Review/Posters/Balloon.pdf`

[39] Abdunabiev, S., Musacchio, C., Merlone, A., Paredes, M., Pasero, E., & Tordella, D. (2024). Validation and traceability of miniaturized multi-parameter cluster radiosondes used for atmospheric observations. *Measurement*, 224, 113879. https://doi.org/10.1016/j.measurement.2023.113879

[40] Paredes Quintanilla, M. E., Abdunabiev, S., Allegretti, M., Merlone, A., Musacchio, C., Pasero, E. G. A., Tordella, D., & Canavero, F. (2021). Innovative mini ultralight radioprobes to track Lagrangian turbulence fluctuations within warm clouds: Electronic design. *Sensors*, 21(4). https://doi.org/10.3390/s21041234

[41] Bosch Sensortec. (2022). *BME280 — Combined humidity and pressure sensor* (Rev. 1.23). Retrieved from `https://www.bosch-sensortec.com/media/boschsensortec/downloads/datasheets/bst-bme280-ds002.pdf`

[42] u-blox. (2021). *ZOE-M8B — Ultra-small, super low-power u-blox M8 GNSS SiP module* (Data sheet, UBX-17035164). Retrieved from `https://www.u-blox.com/sites/default/files/ZOE-M8B_DataSheet_UBX-17035164.pdf`

[43] STMicroelectronics. (2015). *LSM9DS1 — 9-axis inertial module: 3-axis magnetometer, 3-axis accelerometer and 3-axis gyroscope* (Rev. 3). Retrieved from `https://www.st.com/resource/en/datasheet/lsm9ds1.pdf`

[44] OpenCV. (2023). *Open Source Computer Vision, Tracking API.* Retrieved from `https://docs.opencv.org/3.4/d9/df8/group__tracking.html`

[45] Basso, T. C., Perotto, G., Musacchio, C., Merlone, A., Athanassiou, A., & Tordella, D. (2020). Evaluation of Mater-Bi and polylactic acid as materials for biodegradable innovative mini-radiosondes to track small scale fluctuations within clouds. *Materials Chemistry and Physics*, 253, 123411. https://doi.org/10.1016/j.matchemphys.2020.123411

[46] Stoehr, N., Baudrit, B., Haberstroh, E., Nase, M., Heidemeyer, P., & Bastian, M. (2014). Ultrasonic welding of plasticized PLA films. *Journal of Applied Polymer Science*, 132(13). https://doi.org/10.1002/app.41351

[47] Vazquez-Martinez, J. M., Piñero, D., Salguero, J., & Batista, M. (2020). Evaluation of the joining response of biodegradable polylactic acid (PLA) from fused deposition modeling by infrared laser irradiation. *Polymers (Basel)*, 12(11), 2479. https://doi.org/10.3390/polym12112479

[48] Palaniyappan, S., Sivakumar, N., Selvarajan, R., Mohan, D. G., & Rahaman, M. (2024). Ultrasonic welding of cork wood/PLA composites: Effect of welding factors on lap shear strength performance. *Journal of Adhesion Science and Technology*. https://doi.org/10.1080/01694243.2024.2353779

[49] Spotts, M. F., Shoup, T. E., & Hornberger, L. E. (2004). *Design of machine elements* (8th ed.). Pearson Education.

[50] Centro di Agrozootecnia Tetto Frati, Università degli Studi di Torino. (n.d.). Retrieved from `https://www.disafa.unito.it/do/home.pl/View?doc=/ricerca/centri_sperimentali/centro_di_agrozootecnia_tetto_frati.html`

[51] Stull, R. B. (1988). *An introduction to boundary layer meteorology*. Springer.

[52] Batchelor, G. K. (1953). *The theory of homogeneous turbulence*. Cambridge University Press.

[53] O'Connor, E. J., Illingworth, A. J., Brooks, I. M., Westbrook, C. D., Hogan, R. J., Davies, F., & Brooks, B. J. (2010). A method for estimating the turbulent kinetic energy dissipation rate from a vertically pointing Doppler lidar, and independent evaluation from balloon-borne in situ measurements. *Journal of Atmospheric and Oceanic Technology*, 27(10), 1652–1664. https://doi.org/10.1175/2010JTECHA1455.1